CREATING A SOURCE FOR COLD, MAGNETICALLY-TRAPPED BROMINE ATOMS

Jessica Lam

Merton College

University of Oxford



A thesis submitted for the degree of Doctor of Philosophy

Michaelmas Term 2015

CREATING A SOURCE FOR COLD, MAGNETICALLY-TRAPPED BROMINE ATOMS

Jessica Lam, Merton College

A thesis submitted in partial fulfilment of the requirements
for the degree of Doctor of Philosophy of the University of Oxford

Michaelmas Term, 2015

Abstract

This thesis demonstrates the feasibility of producing the first cold source of halogen atoms, using Br atoms as the focus. Br atoms are produced by photodissociation of Br_2, and detected by (2+1) REMPI and time-of-flight measurements. Ground- and excited-state Br fragments are formed with a recoil velocity directed along the molecular beam axis. The excess energy from the dissociation laser provides the backscattered Br fragments with sufficient recoil velocity to match and cancel out the average velocity of the molecular beam. The Br fragments which undergo sufficient velocity cancellation remain in the laser detection volume for up to 5 ms.

A magnetic trap, composed of two permanent bar magnets with their North poles facing each other, is placed around the detection volume and with an axis perpendicular to the molecular beam and laser axes. The centres of the trap and of the laser interaction volume are overlapped. The magnetic field is linear near the centre of the trap and forms a 3-dimensional well with a depth of 0.22 T, equivalent to a trap depth of $U_0/k_B = 255$ mK, with the upper and lower standard error $[215, 325]$ mK, for ground-state Br. With this configuration, Br atoms have been detected up to delays of 99 ms, to the next laser pulse, suggesting the possibility of accumulating density over successive molecular beam cycles.

The decay of Br atoms from the trap is measured, and a Monte Carlo Markov Chain method is implemented to extract the intensity of the Br signal, which decreases to be on the order of the background noise at delays close to 99 ms. Monte-Carlo simulations demonstrate that the trap loss mechanisms are primarily due to collisions with the molecular beam and background gas, inhibiting the ability to accumulate trap density. These simulations also show that Majorana transitions to higher quantum states are minimal and can be ignored. Experimental measurements confirm that near the peak of the molecular beam, when the strongest signal of Br is observed at long delays, around 60% of initially trapped Br atoms are lost due to molecular beam collisions, and (34 $\pm$3)% due to collisions with the background gas.

To minimise molecular beam collisions, a chopper construct is designed to reduce the beam pulse width and is placed between the molecular beam valve and detection volume. The chopper runs from 3,000 rpm to 80,000 rpm, during which the duration of the molecular beam at the detection volume is shortened from 130 μs (measured at the full width at half maximum) to between 80 μs and 13 μs, respectively. However, the chopper significantly reduces the initial Br_2 density in the trapping region, and the influence of the chopper construct in reducing molecular beam collisions requires further experimental work.

Further work is also necessary to improve the operational components, such as reducing the base pressure in the detection chamber to lower background gas collisions, or using a heavier carrier gas to increase density of initially trapped Br atoms. These improvements can lead us closer toward building density of cold Br atoms in the trap over successive molecular beam cycles, with which a source of cold, dense halogen atoms can be realised.

Acknowledgements

I am very thankful for all the people who have supported me throughout my journey in completing this DPhil thesis.

I would like to thank Dr. Chris Rennick for helping me design and implement the experimental and theoretical work over the majority of my DPhil tenure.

I also want to thank Chris and Dr. Brianna Heazlewood for being very available during my thesis writing stage and for providing extensive last minute and highly constructive edits on my thesis drafts.

I want to thank my supervisor, Professor Tim Softley, in mentoring me on my pursuits in extending my DPhil work to conduct new experiments, from undergoing reactions with ozone, to transferring the cold Br atoms into a linear Paul trap. Even though many of these ideas didn't turn out to be feasible, his availability and encouragements significantly helped me improve my confidence, my appreciation for scientific due-diligence, and my creativity. I also want to thank Tim for continually coaching me on effectively communicating my work via writing and PowerPoint presentations. I am a much more confident and better communicator because of this.

I also want to thank my former and current labmates for being there for me. Dr. Will Doherty gave me a smooth transition into his DPhil project. Mike Kohlhoff was there for many last minute stints, from staying late in the office to keep me company while I had to run last minute experiments late into the night, to doing the logistics for submission of this thesis for me. My labmate, wonderful friend, and former housemate, Dr. Katrin Dulitz, would often bounce off many ideas with me, mentor me on conducting good scientific research, and help me navigate the physical chemistry community. And once, when my ceiling fell down into my room, as is typical of Merton college houses in Manor place, within short notice, I had a place on her floor for the night.

I would like to thank the PTCL Electronics Workshop team, in particular, Philip Hurst, for cleverly building and fine-tuning the electronic controller to the motor that runs the chopper construct mentioned. I would also like to thank the PTCL Mechanical Engineering Workshop team, in particular, Charlie Jones, for building the chopper wheel, and Dennis Chikwanha, for constructing the majority of the chopper construct. The contents of chapter 5 would not exist without their support.

I am very grateful for Phil and Barbs O'Malley for continuously being there for me throughout the sleep-deprived and time-constrained turmoil associated with my thesis writing. Love you two!

Finally, I am forever grateful for the unconditional love and support my mom, dad, and brother, Dennis, continuously provide for me. I love you three very much!

Table of Contents

Abstract i

Acknowledgments ii

List of Figures **vi**

1 Introduction **1**

1.1 Chemical dynamics at cold temperatures 1

1.2 Confinement of cold atoms and molecules 6

1.3 Significance and applications of cold halogen atoms 8

1.4 Making and confining cold halogen atoms 11

1.5 Outline of this thesis 13

2 Laboratory Preparation of Cold Br atoms **14**

2.1 Apparatus design 14

2.2 Detection of trapped Br atoms 19

2.3 Formation of photostopped Br atoms 20

2.4 Magnetic trapping of photostopped Br atoms 22

2.5 Analysis of Br signal 24

2.6 Results 27

2.7 Conclusion 29

3 Controlling Trap Loss of Br Atoms **31**

3.1 Monte Carlo simulations 32
3.1.1 Overview of methodology of simulation 32
3.1.2 Movement of simulated Br atoms 33
3.1.3 Elastic collisional dynamics of Br and Ar atoms 35
3.2 Incorporating characteristics of the differential cross sections (DCSs) for Br–Ar elastic collisions into the simulation 36
3.2.1 Calculating the DCS for Br–Ar 36
3.2.2 Using DCSs to determine post-collisional velocities of trapped Br atoms 42
3.3 Using characteristics of the dissociation laser to determine density and trap depth 44
3.4 Results of simulation 48
3.5 A brief exploration of substituting Kr for Ar as the carrier gas atom . . 51
3.6 Accumulating Br atoms over successive molecular beam cycles 53
3.7 Exploring Majorana losses 55
3.8 Conclusion 58

4 Experimental Characterisation of Collisional Trap Loss 59
4.1 Background gas collisions 59
4.2 Molecular beam collisions 63
4.3 Future work 66

5 Development of a Molecular Beam Chopper 69
5.1 Significance of developing a new method to shorten the duration of cold molecular beams 69
5.2 Constraints for the design of the chopper construct 72
5.2.1 Analytical model of pulse width reduction by the chopper . . . 73
5.2.2 Physical constraints 74

5.3 Final design of the chopper construct 75
5.4 Implementing the chopper construct into the source chamber 77
5.5 Testing with NO as the seed molecule 80
5.5.1 Controlling the temperature of the molecular beam 80
5.5.2 Controlling the duration of the molecular beam 85
5.6 Testing with Br_2 as the seed molecule 88
5.7 Controlling trap loss of Br atoms by minimising collisions with the molecular beam 91
5.7.1 Decay of Br atoms with a chopped molecular beam 91
5.7.2 Collisional loss of trapped Br atoms with a chopped molecular beam 94
5.7.3 Accumulation of trapped Br atoms with a chopper 97
5.8 Summary and suggestions for future improvements 99

6 Conclusions and Future Outlook 102
6.1 Summary 102
6.2 Improving the number density and temperature of cold Br atoms . . . 104
6.3 Other atoms and molecules suitable for the Photostop method 107
6.3.1 Preparing photostopped halogen atoms 108
6.3.2 Preparing photostopped non-halogen species 110
6.3.3 Trapping photostopped atoms and molecules 111

1 Monte Carlo Markov chain using Maximum Likelihood Estimation 112

2 Collision cross section for trapped atoms 116

References 119

List of Figures

2.1 Recorded ion image of Br^+ cations, compared with simulations. 17

2.2 Magnetic field along each axis between two opposing permanent magnets. 18

2.3 Schematic of experimental chamber. 19

2.4 Zeeman energies for the two ^2P spin-orbit states of the excited ($J = 1/2$) and ground ($J = 3/2$) fragments in a magnetic field, relative to field-free conditions. 23

2.5 Recorded oscilloscope traces from 1- and 2-colour experiments fit by a Monte Carlo Markov chain-optimised flight time model. 27

2.6 Integrated signal as a function of delay between dissociation and ionization. 28

3.1 Position of simulated Br atoms 100 μs after they are initially formed. . 34

3.2 Potential energy surfaces of the Br–Ar $X_{1/2}$ and $I_{3/2}$ molecular states. . 37

3.3 Diagram of the Br–Ar scattering system. 38

3.4 $Br(^2P_{3/2})$–$Ar(^1S_0)$ DCS for collisions with the molecular beam and thermal background gas. 39

3.5 Distribution of the integrated elastic cross sections for the $Br(^2P_{3/2})$–$Ar(^1S_0)$ scattering. 41

3.6 Normalised cumulative distribution function at a range of scattering angles for Br–Ar collisions with the molecular beam and thermal background. 43

3.7 Density plot of the velocity distribution of photodissociated Br atoms in the lab-frame. 47

3.8 Velocity distribution of Br atoms in the lab-frame, just after undergoing trap loss collisions with the molecular beam and background gas I. . . . 49

3.9 Velocity distribution of Br atoms in the lab-frame, just after undergoing trap loss collisions with the molecular beam and background gas II. . . 50

3.10 Differential cross section for Br with Kr in the molecular beam and thermal background, weighted across the two PESs $X_{1/2}$ and $I_{3/2}$. . . . 52

3.11 Loading curves with Br prepared from a beam of Br_2 seeded in Ar and in Kr. 54

3.12 A map of the locations near the centre of the trap, at which simulated Br atoms will undergo a Majorana transition after 5 s. 57

4.1 Trapped Br atom signal as a function of delay between the dissociation and REMPI lasers for a range of chamber background pressures. 60

4.2 Pseudo-first order trap loss rate coefficient as a function of background Ar density. 61

4.3 Instantaneous molecular beam density, determined from Br fragment ionisation yield. 64

4.4 Scaled fraction of trapped atoms remaining after the molecular beam pulse, determined by extrapolation of trap loss curves. 65

5.1 Range of beam widths achieved with the detection region located right after the molecular beam passes through the chopper slit. 75

5.2 The calculated time between each slit passing through the axis of the molecular beam, as a function of motor speed. 77
5.3 Molecular beam and ion detection section of the experimental set-up with a chopper construct. 78
5.4 Photograph of the chopper set-up in the source chamber. 79
5.5 Diagram of the timing set-up in the chopper controller and delay generator. 80
5.6 Intensities of the rotational absorption lines of NO at a gas pressure of 1×10^{-5} mbar, using a Boltzmann plot method. 82
5.7 Rotational temperatures of NO as a function of gas pressure. 83
5.8 The NO (1+1) REMPI spectrum recorded experimentally and simulated with PGOPHER. 83
5.9 Comparison of the NO signal measured on the multi-channel plates with a chopper running at a revolution speed of 3,000 rpm, with and without a plastic shield. 85
5.10 A normalised profile of the molecular beam with the chopper running at 70,000 rpm. 86
5.11 Plot of beam widths of NO and Br as a function of chopper speed. . . . 87
5.12 Molecular beam profile of 8-10% Br_2 seeded in 3 bar Ar without the presence of a chopper and with a chopper running at 60,000 rpm. . . . 88
5.13 Comparison of the molecular beam profile with a chopper running at 60,000 rpm and at 3,000 rpm. 90
5.14 Signal of Br^+ over multiple molecular beam cycles, with a chopper running at 4,000 rpm and at 6,000 rpm. 90
5.15 Fraction of initially trapped Br atoms remaining after collisions with the molecular beam, determined by extrapolation of a trap loss curve. . 92

5.16 Fraction of initially trapped Br atoms remaining after collisions with the molecular beam. 95

5.17 Loading curves with Br prepared from a beam of Br_2 seeded in Ar and in Kr. 98

1.1 Log-likelihood of the parameters used to fit to the 1-colour background as a function of Monte Carlo Markov chain iteration. 115

Chapter 1

Introduction

1.1 Chemical dynamics at cold temperatures

The production of cold ($\leq$ 1 K) and ultracold ($\leq$ 1 mK) atoms and molecules provides an opportunity to examine chemical processes with unprecedented control. In cold environments, chemical dynamics are dominated by quantum mechanics, providing a doorway for manipulation and interrogation of chemical reactions [1–3].

In standard classical transition state theory, reactants require sufficient energies to overcome a potential energy barrier to form products, and thus the rate of reaction decreases with decreasing temperature [4, 5]. However, "barrierless" reactions, which do not feature an activation energy barrier along the reaction coordinate, often exhibit very different behaviour; as the temperature decreases, the rate of reaction may remain finite, or even increase [3].

The interaction energy that describes these reactions is in the form of an effective potential. The effective potential is proportional to the collision energy and the square of the classical impact parameter, b (equal to the shortest distance between two reactants unaffected by the potential). b is related to the collisional orbital angular momentum state, $l = \mu v_{rel} b$, where μ and v_{rel} are the reduced mass and relative veloc-

ity of the reactants, respectively. The total integrated cross section, σ, made up of a thermal distribution of reaction channels, each associated with a particular l state. At low temperatures, the measured rate constant of the chemical reaction, proportional to σ, can be associated with only a few quantum states.

As the collision energy is lowered, the distribution of accessible scattering channels are concentrated around the lowest l states (and for molecules, the number of rotational and vibrational quantum states are reduced). At sufficiently low temperatures, the rate of reaction is almost solely dependent on the lowest $l = 0$, or "s-wave", state. In this scattering channel, v_{rel} approaches zero, and the centrifugal barrier contribution to the effective potential (proportional to $l(l + 1)$) vanishes, and the reaction is truly barrierless.

For example, Cvitaš *et al.* observed that below 1-3 mK, elastic and inelastic collisions of Li_2 and Li are dominated almost exclusively by the scattering channel associated with $l = 0$ with a vanishing centrifugal barrier. In this regime, the values of σ were found to increase with decreasing temperature, and the total rate coefficients for the inelastic collisions (with Li_2 in the ground and first excited vibrational states) approach a constant value on a log-log scale [6].

State-specific reactants can be prepared with a narrow distribution of collisional energies. As the relative velocities of the colliding reactants are reduced, it is possible to increase the breadth of experimental capabilities. These capabilities include the ability to undertake high precision spectroscopic measurements of the reactants and in some cases the products [7, 8], to refine measurements of fundamental constants [9], and to exert control over the reaction process using perturbations from external fields [10].

Observing cold chemical processes requires the particles to be formed at cold temperatures in artificial environments, as the lowest temperature that can be observed in nature is ∼3 K (in interstellar space) [11, 12]. The first step toward forming cold matter was in 1908, when Heike Kamerlingh Onnes reduced the temperature of gaseous

helium (He) to 4 K, creating liquid He for the first time [13]. This work led him to discover superconductivity only three years later; when Onnes immersed samples of mercury (Hg) and gold (Au) in liquid He and reduced the temperature to 3 K, he found the resistivity of Hg and Au to be "practically zero". In the same experiment, the liquid He used to cool the resistors underwent a superfluid transition at 2.2 K, but this was not realised until much later [14].

Numerous other methods have been developed to produce cold and ultracold species. One of the simplest methods that has been developed to form internally cold species is to pass a high pressure gas through a small hole into a vacuum [15–17]. If the diameter of the hole is larger than the mean free path of the gas in the reservoir, a supersonic jet forms as the gas expands out of the nozzle. Multiple collisions occur in and downstream of the orifice, equilibrating the internal energy of the particles in the jet, thus narrowing the distribution of internal energies. During these collisions, much of the internal energy is converted into kinetic energy, leading to an increase in the velocity component (typically several hundred meters per second) along the jet axis in the laboratory frame. The distribution of the centre-of-mass (COM) velocity of the atoms within the supersonic jet is small, and hence the temperature in the moving frame of the molecular beam is low, which has been exploited in the study of reactions in, for example, merged beams. Here, collision energies can be near-zero in the moving frame of reference, despite the high velocity of the reactants in the lab-frame. When one beam is merged onto a second supersonic beam, the relative velocity between the reactants in the two beams can approach zero, enabling cold chemical reactions to take place in a merged beam [18, 19] or crossed beam [20] geometry. The process of cooling via supersonic expansion has been developed in several ways, such as using a high-pressure seeded expansion [21], pre-cooling from a buffer gas source [22–24], or by passing the gas through a cryo-cooled valve [25,26] or a room-temperature nozzle spinning in a counter-rotating configuration [27–29]. The use of a conical nozzle, in which

the opening angle of the nozzle is reduced, manipulates the supersonic expansion, primarily by increasing spatial confinement of the beam, thereby increasing collisions further down the jet and enhancing the translational cooling and peak density of the atoms close to the jet axis. For a molecule, the lowest internal temperatures that can be reached depend on its rotational constant and can also be limited by cluster formation due to condensation in the jet [30].

The development of laser cooling has created significant advances in reducing the momentum of atoms, atomic ions, and a small number of molecules [31–35]. For a laser propagating counter to the direction of the motion of the particle to be cooled, the wavelength of the laser is red-detuned from the transition wavelength in order for absorption to occur to compensate for the Doppler shift associated with the relative motion between the laser and atom. The particle absorbs a photon and subsequently relaxes back to the ground state, emitting a photon in a random direction. During the absorption, the momentum of the particle in the laser direction is reduced by $\Delta \mathrm{p} = h/\lambda$, where h is the Planck constant and λ is the wavelength of the laser. However, narrow band laser systems that can access the closed cycle of absorption and emission in laser cooled species are limited to those with wavelengths in the IR, visible or near-UV regions. Furthermore, only species with appropriate energy levels can be successfully laser cooled. Ideally, this involves a single ground state and excited state. Where there are numerous energy levels that can be populated when the excited species relaxes, additional lasers are required to return population to the main cooling cycle. This is why very few molecules have been successfully laser cooled, as the addition of rotational and vibrational energy levels makes the number of lasers required impractical to implement. Thus, laser cooling is primarily limited to alkali metal atoms or other metallic elements that possess closed absorption and fluorescence cycles at convenient wavelengths [36–40].

Typically the use of an “optical molasses”, in which six counter-propagating lasers

are directed onto the atom, can reduce the velocity of the atom regardless of its direction of motion. This technique was first demonstrated by Chu *et al.*, who cooled an atomic beam of sodium (Na) atoms down to a translational temperature of 240 μK, corresponding to a root mean square (rms) velocity of 0.6 m/s [31].

Another method that has been developed to generate cold samples is buffer-gas cooling. Here, a thermal flux of ions, atoms or molecules is introduced into a cryogenic buffer-gas cell at temperatures typically around 2-20 K [41]. Multiple collisions between the atoms and the cooled buffer gas (typically He) enable translational and rotational thermalisation of the species of interest to the temperature of the He. The species of interest typically exits the cell through a small orifice, in the form of a slow moving beam seeded in the buffer gas [41, 42]. Unlike laser cooling, this technique is a versatile method for cooling a wide range of species [43].

External fields can be employed to manipulate the translational motion of atoms and molecules, due to the interaction of the electric dipole and magnetic moments of neutral atoms and molecules with external electric and magnetic fields. In the presence of an electric or magnetic field, the Stark or Zeeman energy levels of neutrals with a dipole or magnetic moment, respectively, become non-degenerate. Particles in low-field seeking states moving toward regions of increasing electric or magnetic fields may exhibit an increase in potential energy, and thus a decrease in kinetic energy [44, 45]. In a Stark decelerator, particles in low-field seeking states move through a pair of high voltage electrodes, resulting in an increase in their Stark potential energy as they approach the electrode pair. When the high voltages are rapidly switched off, a small amount of kinetic energy is removed from these particles as their Stark potential energy rapidly decreases to zero. This process is repeated numerous times along the length of the decelerator, thus enabling particles in selected low-field seeking states to be decelerated [46, 47]. Non-polar species–atoms or molecules–with a significant polarisability can be slowed via an optical decelerator, in which a molecular beam

of neutrals intersect two counter-propagating laser beams. The interference from the laser beams forms a periodic potential well, or an "optical lattice", which traps a fraction of the neutrals near the potential minima and decreases the velocities of the trapped neutrals [48]. Similarly to using a Stark decelerator, neutrals with a magnetic moment can be cooled by passing a molecular beam through a Zeeman decelerator. A time-varying series of high-current electric coils in a Zeeman decelerator switches on and off as a molecular beam of neutrals passes through the decelerator, forming a positive longitudinal gradient. The longitudinal gradient produces a force which decelerates a fraction of the neutrals [49, 50].

In electrostatic velocity filtering, a thermal beam of neutral polar species passes through a bent electrostatic guide. At the bend, the fast-moving neutrals continue moving along the original axis of propagation and are lost from the guide, whereas the slowest-moving neutrals are confined to the electric field minimum and guided around the bend, thus resulting in a translationally cold beam of neutrals at the end of the guide [51]. It should be noted that electrostatic guides select for slow-moving species but do not significantly affect the internal energy distribution of the species. While only low-velocity species in low-field seeking states are guided around the bend, there is no direct cooling and so the guided beam typically exhibits a very similar internal energy distribution as in the initial thermal beam.

1.2 Confinement of cold atoms and molecules

Confinement of cold species is crucial to enable reactants to remain in a detection volume for a length of time sufficient for interrogation. Traps are also frequently combined with the cooling methods described in the previous section, allowing the study of reactions with control over the collision energy and properties of both reactants. Ions, which have a charge, can be easily manipulated by external fields, such as by

static magnetic and electric fields in a Penning trap [52], or by time-varying RF electric fields in a linear Paul trap [53]. For example, in a linear Paul trap, time-varying RF voltages are applied to four cylindrical electrodes to generate an effective harmonic electric potential, confining the ions in two dimensions. Static DC voltages are applied to the ends of the electrodes, confining the ions in the third dimension. The ions are thus trapped, limited by the Coulomb repulsion force and thermal motion of the ions. The laser cooling of trapped ions can reduce the temperature of the species to form ensembles of ions at milliKelvin temperatures, in the form of a Coulomb crystal [54–56].

Unlike ions, neutral atoms do not have a net charge and thus require alternative methods, such as magneto-optical traps (MOTs) for confinement. The formation of cold, trapped, neutral atoms has also seen the development of Bose-Einstein condensates (BECs) [57, 58]. At ultra-cold temperatures, the de Broglie wavelength of the particles ($\lambda_{dB} = h/p$ where h is the Planck constant and p is the momentum of the particle and proportional to the square root of the temperature of the particle) becomes large. When it is on the order of the distance between the particles, the majority of particles occupy the same quantum state, and the internal states of the particles become indistinguishable from one another, thus forming a BEC. To prepare a BEC, the particles are first laser-cooled [59, 60], the most common method whereby the particles are Doppler cooled to reduce their kinetic energy inside a MOT generated by magnetic coils in an anti-Helmholtz configuration [61]. Next, the depth of the trap is gradually reduced to promote evaporative cooling [62], until the particles are at nanoKelvin temperatures and at densities of 10^{14}–10^{15} cm^{-3}.

Molecules are typically harder to trap than atoms, because the complexity of their internal energy states provide additional degrees of freedom, which make it difficult for them to be experimentally manipulated [63]. Despite this challenge, standard techniques in preparing and trapping cold atoms have been extended to molecules, such as producing cold diatomic molecules in a MOT, primarily by including additional

re-pump lasers to minimise unwanted population of rotational and vibrational states [64]. Cold molecules can also be formed and trapped via magnetoassociation [65] or photoassociation [66, 67], in which a magnetic field or laser excitation, respectively, modifies the energy of two colliding atoms to become resonant with a bound molecular state. The molecules are then cold enough to be trapped in a shallow optical dipole trap formed by standing waves from superimposed laser beams.

Permanent magnets provide an alternative route to MOTs for trapping cold atoms and molecules. Permanent magnets typically provide magnetic fields tens of times stronger than magnetic traps using electromagnetic coils [61], such as MOTs, which generate weak trapping fields on the order of hundreds of Gauss. The larger field strength, and thus larger trap depth, allows the trapping of atoms and molecules with small magnetic moments. Such permanent-field traps require a method to remove atomic kinetic energy. In some cases, the dissipative force can be provided by laser cooling [68], or the trap could be loaded from a buffer-gas cooled atomic [69] or molecular [70–73] gas cell or Zeeman- or Stark-decelerated molecular beam [74, 75]. In the work described in this thesis, a method is developed whereby the cold atoms are generated by photodissociation *inside* the trap, allowing, in principle, reloading and accumulation of density.

1.3 Significance and applications of cold halogen atoms

The production of cold, trapped free radicals is of particular interest due to their significant role in nature, from the breakdown of ozone (O_3) [76, 77] to altering biological functions [78–80]. Their open shell configuration enables them to be highly reactive. Radicals can be manipulated by magnetic fields and, in the case of polar

species, electric fields. Halogen atoms are highly reactive and highly electronegative free radicals. Reactive collisions between a halogen atom, such as F [81, 82], Cl [83], and Br [84], with H_2 are some of the simplest reactions, yet which serve as prototypes for more complex chemical reactions, such as in exothermic exchange reactions [82], in atmospheric radical chain reactions [85], and in combustion chemistry [86–88].

The reactions of several atmospherically and astrochemically important radicals (such as OH, CN, NO, N, O) have been examined using, for example, the Cinétique de Réaction en Ecoulement Supersonique Uniforme (CRESU) experiment [89]. Sims *et al.* performed CRESU experiments to study the reactions of OH + HBr [90]. While the rate constant was found to have little variation over the range 200 K to 400 K, it was observed to increase monotonically as the temperature was lowered from 200 K to 23 K. To date, no CRESU experiments have been performed to examine the temperature dependence of halogen radical reactions.

The low barrier to reaction with halogen radicals renders them suitable for the study of low-temperature kinetics [3, 91, 92]. For example, below 10 K, the cross sections for the reaction between F and $H_2(\nu = 0,\ J = 0)$ to form HF ($\nu' = 0,\ 1,\ 2$) and H increases with decreasing collisional energy [93, 94]. Substituting H_2 for D_2 results in a slower reaction, with a rate constant 100 times smaller, due to the heavier mass of D_2 [92].

Low temperature kinetics provide insight into the long-range interaction between reactants. For example, theoretical work suggests that at collision energies below 10 meV, the long-range part of the interaction potential of Cl + HD ($\nu = 1$), described by the formation of a van der Waals complex, exhibits resonances in the rate of predissociation into HCl + D [95]. Experimental investigation of such a system would be highly valuable to better understand how such reactions occur at a fundamental level.

This thesis focuses on Br, as its parent molecular Br_2 has a broad region of continuous absorption and a dissociation energy accessible in the visible regime [96].

The preparation of Br from photodissociation of Br_2 is also well studied and understood [96–98]. However, there are at present very few methods for preparing cold Br atoms for reaction studies. Theories on how halogen species such as Br interact with H_2 and D_2 in cold environments are yet to be tested experimentally [95]. Such information is crucial for accurate modelling of the chemistry of halogen species occurring in the stratosphere [99].

The Br radical is an important player in atmospheric chemistry. In the stratosphere, Br is 50-60 times more effective in depleting O_3 than Cl [100–102]. Reactions of Br with organic compounds, such as oxidation reactions with hydrocarbons and ethers [103–107], have been found to exhibit very different rates of competing reactions (including oxidation, halogenation, and hydrogen abstraction) than that of other electrophilic reagents, such as O_3, $O(^3P)$, NO_3, OH, and Cl [103]. Given the wide range of temperatures in the atmosphere, an understanding of the temperature-dependence of the reaction rate is important for atmospheric modelling. Thus, low-temperature methods are potentially valuable.

The fine structure of Br also plays a role in chemical reactions and energy transfer, particularly in combustion and atmospheric reactions. The spin-orbit splitting between the ground $^2P_{3/2}$ and spin-orbit excited $^2P_{1/2}$ states of Br is 3685 cm^{-1}, which is close to the fundamental frequency of the ν_1 OH stretching mode of methanol (3682 cm^{-1}) [108, 109]. There are also near-resonances with vibrational modes in H_2O (3657 cm^{-1}) [110] and CF_2H_2 (3015 cm^{-1}) [111], and thus, it would be interesting to investigate the resonance-enhancement of energy transfer between the spin-orbit energy of Br and the vibrational energy of the collision partner.

Cold halogen atoms could, in principle, also be combined with laser-cooled alkali metal atoms through methods such as photoassociation or magnetoassociation to form highly polar cold diatomic molecules. For example, at low temperatures, potassium bromide (KBr), which possesses a very strong dipole of 10.5 D [112], may be an at-

tractive molecule for the development of quantum information processing.

1.4 Making and confining cold halogen atoms

The lowest energy–allowed single–photon transition of elements such as halogens lies in the vacuum ultraviolet (for example, requiring photon wavelengths of 95.48, 134.73 and 157.64 nm for F, Cl, and Br, respectively), a spectral region for which sufficiently powerful continuous–wave laser systems are not widely available [113, 114]. Thus, laser cooling methods would be extremely challenging to apply to halogen atoms and therefore have not been demonstrated to date. An alternative approach may be to use a Zeeman decelerator to reduce the velocity of a supersonic beam seeded with halogen atoms. However, the magnetic moment to mass ratio is very unfavourable for Zeeman deceleration of Cl and Br [115], and thus, an exceedingly complex decelerator with hundreds of stages would have to be constructed.

Recently, a new method to produce cold atoms and molecules using near-threshold photolysis has been developed [116]. In 2007, Matthews *et al.* proposed that O(^{3}P) atoms could be prepared at cold temperatures by dissociating a beam of NO_2 molecules, producing NO($J'' = 3/2$) and O($^3P_2$) fragments [117]. The laser energy can be tuned to produce O($^3P_2$) fragments with an available energy of 175 cm^{-1}, which corresponds to a speed of 413 m/s. The anisotropy parameter β, which describes the angular distribution of the fragments upon photolysis (described in section 2.3) [118], has a value of 1.5, indicating a parallel transition. Thus, by tuning the laser polarisation to be parallel to the molecular beam, the O($^3P_2$) fragments can scatter forward and backward along the molecular beam axis. The O atoms with the lowest lab-frame velocities will remain in the detection volume for the longest of time, in contrast to the fastest atoms, which will leave the detection volume first. Further explanation of this technique is described in section 2.3.

Subsequently, Zhao *et al.* demonstrated that photodissociating a molecular beam of NO_2 at 344 nm can produce slow NO($X^2\Pi, \nu = 1, J = 8.5$) fragments with the full-width half-maximum (FWHM) of the longitudinal velocity distribution estimated to be in the range 35 m/s to 45 m/s (from a molecular beam moving at 565 m/s) [119]. These molecules remained in the detection region for up to 300 ns, suggesting that fragments with velocities closer to zero were also formed. However, the use of a laser with a fixed wavelength prevented them from tuning the recoil COM velocity of the fragments to exactly cancel the lab-frame velocity of the molecular beam.

This technique was further optimised by Trottier *et al.*, who used a tunable dissociation laser and termed this method, 'Photostop' [120]. The work resulted in the production of a cold source of NO($X^2\Pi_{3/2}, \nu = 0, J = 1.5 - 9.5$) molecules by photodissociating the parent NO_2 molecules and waiting 10 μs for those with the highest kinetic energies to leave the detection volume. The FWHM of the longitudinal velocity distribution of the NO molecules remaining in the detection volume was 23 m/s, corresponding to a translational temperature of 1.6 K. A density of 10^9 cm^{-3} was reported, which is a promising step towards generating a source of cold, confined radicals for the observation of cold chemical reactions.

Recently, cold halogen atoms were formed for the first time using the Photostop method. A molecular beam of Br_2 moving at 385 m/s was dissociated in the wavelength region 480-490 nm to produce Br fragments in the ground $^2P_{3/2}$ and excited $^2P_{1/2}$ spin-orbit states. Upon photodissociation, a density of 10^8 cm^{-3} was achieved for Br atoms at temperatures less than 1 K. Br atoms were still detectable up to 100 μs post-formation, at which point the values for the FWHM of the velocity distributions parallel and perpendicular to the molecular beam propagation direction were measured to be 17 m/s and 59 m/s, corresponding to temperatures of 520 mK and 6 K, respectively [116].

However, a disadvantage of creating cold halogen atoms via the Photostop method

is that the atoms have a finite velocity distribution, and therefore most of the atoms leave the trap volume after 100 μs. Thus, the ability to observe chemical reactions is prohibited due to the very narrow timescales during which a reaction will have to occur. Even if reactions can occur within this time scale, a sufficient density of atoms will have to be reached for the probability of a reaction to be high enough to be observable. Consequently, a method to trap and accumulate atoms is desirable, and this forms the subject of the work described in this thesis.

1.5 Outline of this thesis

In this thesis, the production of cold, magnetically-trapped bromine atoms at translational temperatures $\leq$ 300 mK is demonstrated for the first time. Chapter 2 describes the preparation of cold Br atoms via the Photostop method and their confinement in a magnetic field. Chapter 3 discusses theoretical modelling of trap loss due to elastic collisions with the carrier and background gas and quantum-state transitions to untrappable states. Chapter 4 shows experimental results that support the theoretical calculations in Chapter 3. A method to minimise the main cause of trap loss using a mechanical chopper construct is then discussed in Chapter 5. And finally, Chapter 6 suggests examples of ways to improve the trapping of Br and other halogen species and free radicals, with a view to generate a dense source of reactants for the study of cold, controlled reactions.

Chapter 2

Laboratory Preparation of Cold Br atoms

Br atoms are highly reactive. To produce Br atoms in a controlled fashion, the diatomic Br_2 molecule is photodissociated using tunable lasers. Widely available and inexpensive permanent magnets can be used to confine the Br atoms, thus providing a versatile and cost-effective route for creating a cold Br atom source. This chapter describes the apparatus developed for the formation, trapping, and detection of cold Br atoms. The content in this chapter is drawn from Lam *et al.* [121] and Rennick *et al.* [122], as published in the journals *Physical Review A* and *Physical Review Letters*, respectively.

2.1 Apparatus design

A pulsed supersonic molecular beam of 8% Br_2 by volume is formed by saturating Ar carrier gas with the vapour pressure from liquid Br_2 at room temperature. The mixture expands through a 0.5 mm diameter pulsed General Valve Series 9 valve system at a backing pressure of 3 bar and operating at 10 Hz. The beam subsequently passes through a 1 mm skimmer, into the second, differentially pumped, chamber (described

later in section 2.2 in figure 2.3).

Because it is very difficult to measure the pressure of the beam coming directly out of a pulsed valve, the gas pressure is defined to be that measured by a pressure gauge located about 3.5 cm from the beam axis. The reproducibility of the gas pressure from the nozzle is controlled by a proportional-integral-derivative (PID) controller, optimized to ensure the pressure oscillates steadily around a defined value within a 20% error. The PID controller signals an input-output (IO) controller in the range 0 V to 5 V to a valve control box, which sends this voltage pulse to a solenoid in the valve. The solenoid retracts an armature holding the Teflon poppet sealing the nozzle. At a voltage of 0 V, the nozzle is fully sealed, and of 5 V, fully open. This capacity is defined by the following two factors on the valve controller: a course controller sets the baseline pressure at which the spring is always pulled back, and a span controller controls the extent to which the spring can compress.

Br_2 absorbs strongly above its dissociation limit in a broad continuum spanning 320 nm to 600 nm [97]. A 460 nm Nd:YAG pumped pulsed dye-laser (5 ns pulse length, Coumarin 460) is used to excite Br_2 molecules for an energy state above their dissociation energy, leading to prompt dissociation. As described in more details in section 2.3, two channels are available - one producing two ground state $Br(^2P_{3/2})$ atoms and the other producing one ground state $Br(^2P_{3/2})$ atom and one excited state $Br^*(^2P_{1/2})$ atom. The latter channel dominates at this dissociation wavelength.

The velocity distribution can be determined by ionising the atoms and employing either ion imaging or time-of-flight (TOF) analysis [123]. Ground state $Br(^2P_{3/2})$ atoms are ionised via $(2+1)$ resonance enhanced multi-photon ionisation (REMPI) at 226.2021 nm ($5p\ ^2D_{3/2} \leftarrow 4p\ ^2P_{3/2}$) by a frequency-doubled dye laser (Coumarin 503) [124], extracted into a 50 cm long TOF tube and detected by a multichannel plate (MCP). The current from the MCP is amplified using a phosphor screen and a photomultiplier detector, and the output recorded on an oscilloscope. The dissociation

and REMPI lasers are fired simultaneously, to ensure that the Br atoms are detected at the instant that they are produced in the probe laser volume. Similar conditions are used to record the TOF signal and ion images, with the exception of the electric potentials on the extractor plate (shown in figure 2.3), which is tuned from 0.6 V to 1.4 V, and on the phosphor screen, which is tuned from 100 V to 3000 V, respectively.

Figure 2.1 shows an ion image of the two product branches of photodissociated Br_2 (right), obtained under velocity mapping conditions, compared with simulations showing views projected perpendicular (left, top) and parallel (left, bottom) to the ion image. The experimental ion image is skewed, due to the Lorentz force exerted on the charged Br^+ cations in the presence of the high magnetic field. The high magnetic field is generated by the trapping magnets (see figure 2.2), located in the stack of electrodes, which guide the Br^+ cations toward the MCP detector. Despite appearing skewed, the ion image behaves qualitatively as expected. The Br atoms formed via the excited channel (blue) fill a spherical volume with the distribution of Br fragments concentrated at opposite ends along the molecular beam axis (approximately $\beta = 2$) in the direction perpendicular to the page. In contrast, the Br atoms formed via the ground state channel (red) fill a larger spherical volume, concentrated around a ring perpendicular to the molecular beam axis (approximately β = -1) [124]. In the ground state channel, the size of the sphere is larger, due to the smaller dissociation energy needed to dissociate Br_2. Thus, a larger amount of excess photon energy is available, shown by the larger recoil velocities of the resulting Br atoms (red).

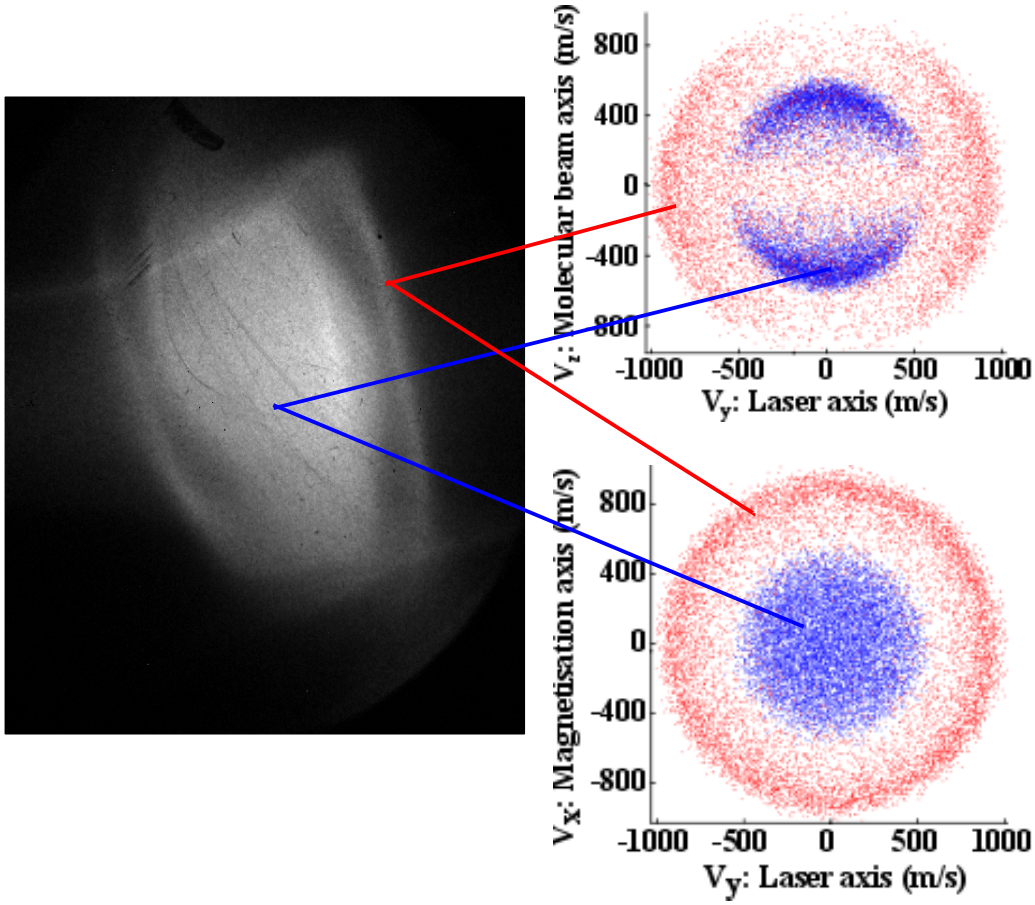

Figure 2.1: Recorded ion image of Br^+ cations produced by (2+1) REMPI (left), compared with simulations from the perspectives of a side view (right, top) and a bird's eye view (right, bottom) of the experimental set-up. (The recorded ion image is also a bird's eye view perspective.) The Br atoms produced by the excited state channel (blue dots in simulations) give the signal at the centre of the ion image (shown by the blue lines), and similarly, the Br atoms produced by the ground state channel (red dots in simulations) cause the outer rings in the ion image (shown by the red lines). The background signal without the presence of Br^+ is negligible, and thus this VMI image is equal to that of a background-subtracted image.

Br atoms are formed at the centre of a magnetic trap (see figure 2.3). The counter-propagating photodissociation and REMPI lasers pass along the x-axis, intersecting the molecular beam along the z-axis. The magnetic trap, created by a pair of opposing neodymium iron boride (NdFeB) permanent bar magnets (Arnold Magnetic Technologies), is used to confine low-velocity paramagnetic species in the Photostop experiment. The $2 \times 4 \times 10$ mm magnets are magnetised along the longest (y) axis

with a remnance of 1.4 T and are clamped with the 2×4 mm north pole faces opposing each other and separated by 2 mm. The Br atoms are thus confined in three dimensions by the magnetic minimum. The sintered NdFeB magnets have a remarkably high resistance to demagnetization; the field due to one magnet is 0.1 T at the face of the opposing magnet, resulting in negligible demagnetisation. The components of the field are calculated analytically [125], as described in section 3.1.2. The magnetic field near the centre of the trap can be approximated by adding the field components of each individual magnet, as plotted in figure 2.2.

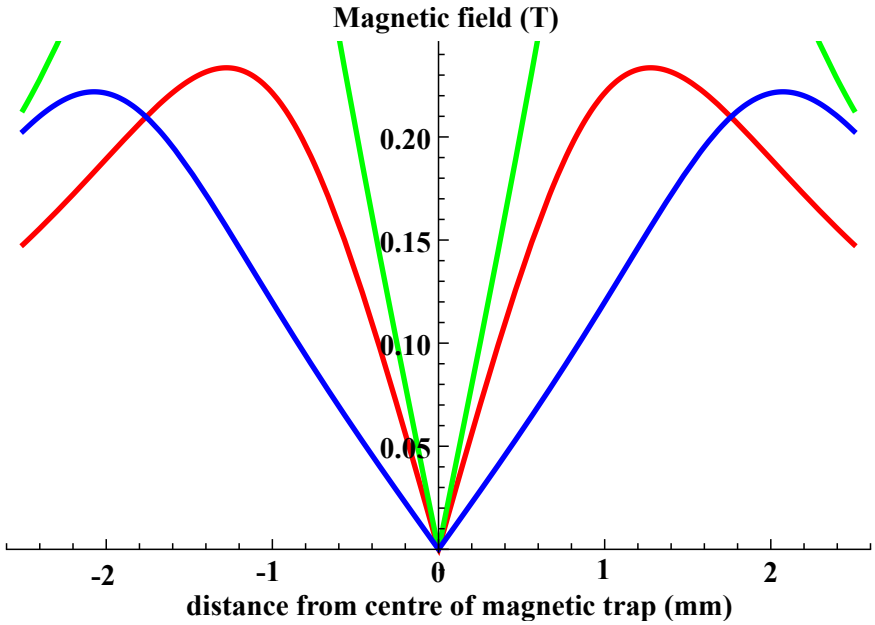

Figure 2.2: Magnetic field along each axis between two opposing permanent magnets. Green: x-axis, parallel to the laser propagation axis; red: y-axis, parallel to the magnetisation axis; blue: z-axis, parallel to the laser molecular beam axis. The figure is drawn from Rennick *et al.* [122].

The trap depth corresponds to the potential energy of an atom at the lowest saddle point in the trapping potential, seen in figure 2.2 to correspond to a field strength of (0.24 ± 0.02) T, determined from the manufacturer's nominal magnetisation and dimensional tolerance. There is a field minimum at the midpoint of the gap between the magnets, rising to a saddle point at 1 mm and 2 mm from the centre along the x-

and z-axes, respectively.

2.2 Detection of trapped Br atoms

Figure 2.3 shows a close-up of the experimental chamber with the magnetic trap.

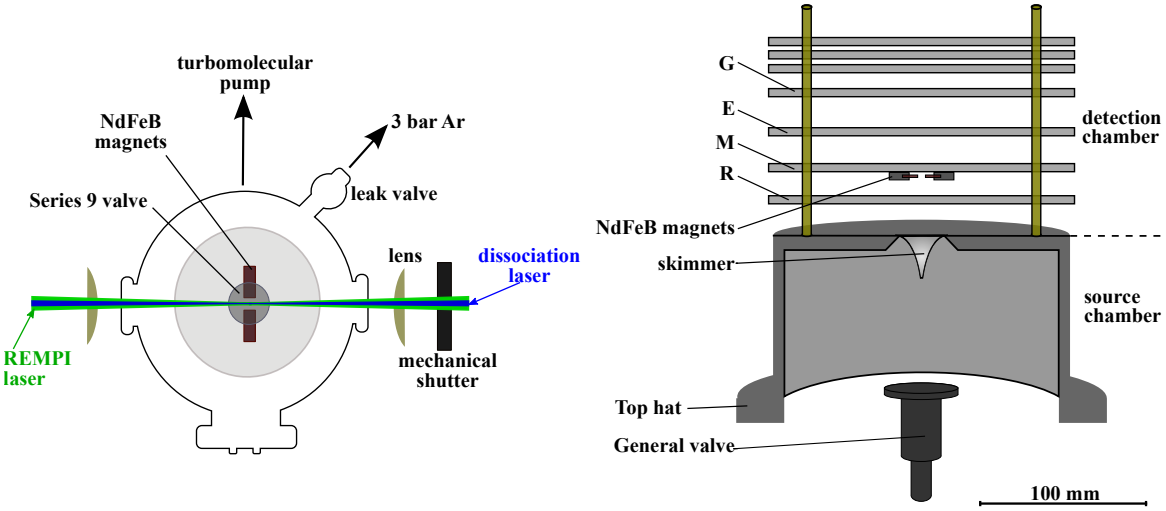

Figure 2.3: Schematic of experimental chamber, bird's eye view (left) and street view (right). The REMPI (green) and dissociation (blue) lasers intersect the molecular beam (not shown, perpendicular to the page at the centre of the Series 9 valve) between the two bar magnets (burgundy rods). The Al magnet-mount plate (M) is positioned between the repeller (R) and extractor (E) of a Wiley-McLaren electrode stack and a grounded flight tube that extends from the grounded plate (G). The source chamber is pumped by a diffusion pump located underneath the figure on the left (not shown). The figure is partly reproduced from Lam *et al.* [126]. The diagram is not to scale.

The detection laser is tuned to resonantly ionise only Br atoms formed in the ground $^2P_{3/2}$ state, so the Br* atoms in the excited $^2P_{1/2}$ state do not contribute to the measured signal. Trapped Br* atoms are metastable with respect to radiative decay and collisional quenching [127]. The radiative lifetime of Br* is 1.12 s, and no effects are observed from re-population of the ground state on the 99 ms time scale of these experiments. Br^+ cations produced by REMPI are extracted into the flight tube by the repeller (R) and extractor (E) plates. The NdFeB magnets are mounted on plate M, and the two laser beams pass between the magnets parallel to plate M

in counter-propagating directions. The magnets are electrically biased at a voltage of 1.7 V to minimize perturbation to the local electric field and to maintain extraction efficiency.

2.3 Formation of photostopped Br atoms

Two combinations of products are energetically available at wavelengths shorter than 510 nm: a pair of ground state $Br(^2P_{3/2})$ atoms, or one ground $Br(^2P_{3/2})$ atom and one spin-orbit excited $Br^*(^2P_{1/2})$ atom [124]. The excited Br_2 then dissociates via two channels [96, 124]:

$$Br_2 + h\nu \rightarrow Br(^2P_{3/2}) + Br^*(^2P_{1/2}), \tag{2.1}$$

$$Br_2 + h\nu \rightarrow Br(^2P_{3/2}) + Br(^2P_{3/2}), \tag{2.2}$$

where h is the Planck constant and ν is the frequency of the dissociation laser. Reaction 2.1 occurs through a parallel ($\Delta\Omega = 0$) transition from the $X^1\Sigma_g^+(0_g^+)$ ground state to an excited state of $B^3\Pi_u(0_u^+)$ symmetry, whereas reaction 2.2 occurs through a perpendicular ($\Delta\Omega = \pm 1$) transition from the ground state to an excited state of $^1\Pi_u(1_u)$ symmetry.

The Br fragments recoil preferentially along the laser polarisation axis with a near-limiting value of the anisotropy parameter, β, which characterizes the photofragment angular distribution in terms of the second Legendre polynomial [118],

$$I(\Theta) = \sigma/(4\pi)\left[1 + \beta P_2(\cos\Theta)\right]. \tag{2.3}$$

Thus, the distribution of laboratory-frame velocities and directions of the recoiling Br atoms can be controlled via the wavelength and polarisation of the photodissociation

laser.

The terminal velocity of the Ar in the beam is calculated to be 556 m/s, and photodissociation at 460 nm produces both $Br(^2P_{3/2})$ and spin-orbit excited $Br^*(^2P_{1/2})$. If the polarisation of the laser pulse is parallel to the molecular beam, one of the Br atoms moves backwards relative to the beam direction; and if the dissociation laser energy is selected such that the recoil velocity matches the molecular beam, cancellation between the centre of mass and recoil velocities results in one Br atom remaining stationary in the laboratory frame of reference. The Br atoms formed via channel 2.1 has a recoil angular distribution centred along the molecular beam axis. The percentage of Br atoms formed in this channel is 60% [124], with equal populations of ground state $Br(^2P_{3/2})$ and spin-orbit excited $Br^*(^2P_{1/2})$ atoms. An equal distribution of m_J sub-levels is assumed.

The centre of mass frame recoil velocity of the Br fragments, $v_{COM,\,Br}$, is [123]:

$$v_{COM,\,Br} = \sqrt{2E_{kin}^{avg}\frac{m_{Br^*}}{m_{Br}m_{Br_2}}}, \tag{2.4}$$

where E_{kin}^{avg} is the average kinetic energy of the Br fragments, m_{Br^*} is the mass of the excited state Br fragment, m_{Br} is the mass of the ground state Br fragment, and m_{Br_2} is the mass of the Br_2 parent molecule. The recoil kinetic energy arises from the excess photon energy above the dissociation limit; accounting for the internal energies of the molecular precursor and atomic fragments, E_{kin}^{avg} is given by:

$$E_{kin}^{avg} = h\nu + E_{int}^{Br_2} - (D_0^{Br_2} + E_{int}^{Br} + E_{int}^{Br^*}), \tag{2.5}$$

where ν is the frequency of the laser, $E_{int}^{Br_2}$ and $D_0^{Br_2}$ are the internal and dissociation energies of Br_2, respectively, and E_{int}^{Br} and $E_{int}^{Br^*}$ are the internal energies of ground and excited Br and Br^* atoms, respectively. The mean velocity of the subset of backward

recoiling atoms can be arbitrarily close to zero, but in practice, a distribution of finite speeds remains owing to the velocity distribution of the molecular beam and the product angular distribution of fragmentation.

The sample of Br_2 is not isotopically pure, and the different parent isotopologues have varying dissociation energies [128]. For example, the dissociation energies in channel 2.1 range from (D_0 = 19580 cm^{-1}) for the $^{79}Br^{79}Br$ parent molecule, to (D_0 = 19582 cm^{-1}) for the $^{81}Br^{81}Br$ parent molecule. Taking the energy of the dissociation laser to be 21,739 cm^{-1} (at 460 nm), the average recoil velocities of the Br fragments will range from 517 m/s to 564 m/s, respectively. The velocities for the $^{81}Br^{79}Br$ parent molecule will lie in between these two extremes. As the spread of photofragment velocities is less than the velocity spread of the parent molecules, and as the experimental parameters are optimised to maximise the signal of slow Br atoms, variations in the atomic mass of Br are ignored in the experiment, and an average mass (representing the natural isotopic abundances) is used in the simulations.

2.4 Magnetic trapping of photostopped Br atoms

Photodissociation of Br_2 produces an anisotropic velocity distribution containing speeds in the lab frame ranging from 0 m/s to 1110 m/s. No additional cooling mechanism operates after photodissociation, and the Br fragments with low enough speeds remain in the detection volume. However, the cloud of slow atoms will continue to expand and decrease in density, and thus a method is needed to trap the slowest atoms in a well defined spatial region.

In the presence of a weak magnetic field, the ground and spin-orbit excited states of the Br atom split into six Zeeman energy levels, labelled by the angular momentum, J, and its projection on the axis defined by the field, m_J. Figure 2.4 shows the Zeeman splitting of the ground $^2P_{3/2}$ and excited $^2P_{1/2}$ spin-orbit components as a function

of magnetic field. The Zeeman energy is given approximately by $\Delta E = g_J m_J \mu_B |B|$, where m_J can take the values of $+3/2, +1/2, -1/2, -3/2$ for the $^2P_{3/2}$ state (blue lines) and $+1/2, -1/2$ for the $^2P_{1/2}$ state (black dashed lines). The spin-orbit excited state ($J = 1/2$) possesses a Landé g-factor ($g_J = 2/3$), equal to half the magnitude of that of the ground state ($g_J = 4/3$), resulting in a much shallower trap depth.

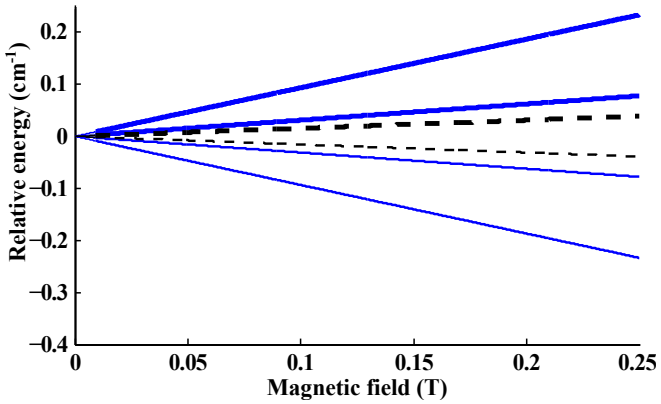

Figure 2.4: Zeeman energies for the two ^2P spin-orbit states of the excited ($J = 1/2$) (black) and ground ($J = 3/2$) (blue) fragments in a magnetic field, relative to field-free conditions. The bold lines are the low-field seeking ($m_J = +3/2, +1/2$) states that can be trapped.

The states that increase in energy with increasing magnetic field ($m_J = +3/2,\ +1/2$) are termed low-field seeking states (bold lines in figure 2.4). Only the Br atoms in these low-field seeking states can be trapped. As the m_J sub-levels of the ground state show a larger increase in energy for a given field, a greater number of Br atoms in the ground state than in the excited state will be trapped.

Only the spin-orbit ground state ($J = 3/2$) level is explored in this thesis. At the magnetic minimum in the trap, the Zeeman potential energy shift for the excited state Br* atom ($m_J = 1/2$) is 0.0315 cm^{-1}, and for the ground state Br atom is 0.205 cm^{-1}, for the ($m_J = 3/2$) state, and 0.0684 cm^{-1}, for the ($m_J = 1/2$) state.

For the trappable states ($m_J = +3/2,\ +1/2$), the nuclear hyperfine coupling is calculated to be too small to be detected. In a weak magnetic field, the allowed transitions between hyperfine states are those with $\Delta F = \pm 1$, $\Delta m_F = 0$. Differences

in energies in the hyperfine transitions in the ($5p\ ^2D_{3/2} \leftarrow 4p\ ^2P_{3/2}$) (2+1) REMPI transition requires a probe wavelength resolution ranging from 0.04 cm^{-1} to 0.08 cm^{-1}, which lies within the linewidth of the REMPI laser (0.1 cm^{-1}).

The ability to create cold atoms right at the trap centre enables further reloading of atoms without the need to "open" the trap. As the Br atoms move away from the centre of the trap, the magnetic field increases. This field gradient produces a force that accelerates the Br atoms back toward the trap centre:

$$\mathbf{a} = -\frac{\mu_B \cdot m_J \cdot g}{m_{\mathrm{Br}}} \cdot \frac{d}{d\mathbf{r}}\mathbf{B}, \tag{2.6}$$

where $\mathbf{a}$ is the acceleration of the Br atom, μ_B is the Bohr magneton, m_J is the angular momentum projection quantum number, g is the Landé g factor, $\mathrm{m_{Br}}$ is the mass of the Br atom, $\mathbf{r}$ is the radial distance from the centre of the trap, and $\mathbf{B}$ is the magnetic field vector.

As Br atoms in low field-seeking states move toward regions of higher magnetic field strength, they gain potential energy at the cost of kinetic energy, thereby slowing down, and are thus unable to escape the trap. The lowest barrier of our trap, in the direction parallel to the molecular beam axis, is 0.22 T. This corresponds to an ability to trap Br atoms with a maximum speed of 7.9 m/s for a spin-orbit ground state Br atom formed at the centre of the trap in the ($m_J = 3/2$) sub-state, of 4.5 m/s for a spin-orbit ground state Br atom in the ($m_J = 1/2$) sub-state, and of 3.2 m/s for a spin-orbit excited state Br^* atom in the ($m_J = 1/2$) sub-state.

2.5 Analysis of Br signal

Ionisation of the Br_2 parent molecules does not contribute to the recorded signal, as the wavelength used in the REMPI detection is far from the Br_2 resonance at 263 nm [129]. However, the REMPI laser is sufficiently energetic to dissociate residual Br_2 and to

then ionise the resulting fragments. Even at the longest laser delays probed, the recorded TOF signal contains significant contributions from this 1-colour background, in addition to the 2-colour signal from photostopped Br atoms. The velocities of the Br^+ cations in the 1-colour background are much greater than those in the 2-colour signal [130], and thus the 1-colour background is not resolved in the recorded ion image for this experimental set-up. While some of this contribution can be eliminated based on the ion flight time (as Br atoms from background Br_2 have a much higher initial velocity than the near-zero speed of trapped atoms) the angular anisotropy of the background photofragment signal still produces atoms with a zero velocity component in the TOF direction. This contribution to the detected signal is eliminated by recording two alternating batches of TOF traces: a 10-shot average of the 2-colour TOF trace, followed by a 10-shot average 1-colour signal (recorded using only the REMPI laser). This 1-colour signal is recorded using a mechanical shutter to block the photodissociation laser. Following this background subtraction, delaying the REMPI laser with respect to the gas pulse and dissociation laser pulse maps the decay of trapped Br atoms [123].

Figure 2.5 shows the averaged 1-colour signal recorded with the dissociation laser blocked, and the 2-colour signal that includes a contribution from trapped Br. The integrated trapped atom density is extracted from the measured signal by fitting the 1-colour background and 2-colour signals to a TOF model that represents the velocity-dependent arrival time distribution. The model parameters are optimised by a Markov Chain Monte Carlo (MCMC) method using a maximum likelihood estimator [131–133], described in more detail in Appendix 1.

The low count numbers mean that the statistics of signal intensity follow a Poisson distribution, so regular χ^2-distribution fitting is not statistically valid and fails to extract small signals from the large 1-colour background. Subtracting one Poisson distribution from another does not result in another Poisson distribution but rather in

a Skellam distribution, producing an apparently negative signal. For sufficiently large signals, the measurement uncertainty is closely approximated by a normal distribution. As the difference between two normal distributions is also a normal distribution, subtracting the background from the signal is sufficient. Here, an additive approach is taken, as the sum of two Poisson distributions is a Poisson distribution.

The 1-colour background TOF signal, $\mu_{\mathrm{bg}}(t)$, is represented by the sum of two Gaussian functions, representing the flight time of the two velocity components formed on dissociation and ionisation.

$$\mu_{\mathrm{bg}}(t) = \omega + \sum_{\mathrm{b}=1}^{2} \alpha_{\mathrm{b}} \exp\left\{\frac{-(t-\beta_{\mathrm{b}})^2}{2\gamma_{\mathrm{b}}^2}\right\}, \tag{2.7}$$

where ω is a background offset that accounts for electrical pick-up from the laser flash-lamps and t is the flight time. The parameters α_{b}, β_{b}, and γ_{b} are the maximum intensity, flight time, and standard deviation (respectively) for each of the two Gaussian functions. These six parameters are optimised to fit the data.

The 2-colour signal is represented by the background fit function in equation 2.7, plus a single additional Gaussian function that represents the flight time for ions produced from trapped Br atoms.

$$\mu_{\mathrm{sig}}(t) = \mu_{\mathrm{bg}}(t) + \alpha_{\mathrm{s}} \exp\left\{\frac{-(t-\beta_{\mathrm{s}})^2}{2\gamma_{\mathrm{s}}^2}\right\}, \tag{2.8}$$

where the three additional parameters α_{s}, β_{s}, and γ_{s} represent the maximum intensity, TOF, and standard deviation (respectively) of the trapped Br signal. Here, the six background parameters are kept fixed, with only the set of additional parameters adjusted in the fit. This additive approach accounts for the underlying statistics, and it prevents the noise enhancement that occurs from simply subtracting the background from the signal traces and then fitting a single Gaussian to the resulting difference. Fig-

ure 2.5 plots average 1- and 2-colour TOF traces overlaid with the MCMC-optimised flight time model.

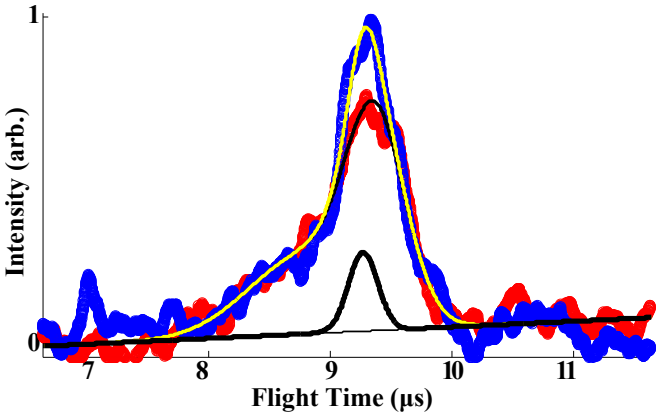

Figure 2.5: Recorded oscilloscope traces from 1- and 2-colour experiments fit by a MCMC-optimised flight time model. The 1-colour background is shown in red, and the 2-colour signal is shown in blue. The MCMC fits for the background and signal are shown by the yellow and thin black curves, respectively. The thick black curve illustrates the component resulting from trapped Br atoms. The figure is drawn from Lam *et al.* [121].

The signal intensity, proportional to [Br], is defined as the product of the maximum intensity and standard deviation of the component representing trapped Br atoms ($\alpha_s \times \gamma_s$). The corresponding 95% confidence intervals for these two parameters are summed and weighted to calculate the total error in the signal intensity, $[\mathrm{Br}]_{\mathbf{err}}$.

2.6 Results

Integrating the peak in the extracted 2-colour signal gives an estimate of the number of Br atoms remaining in the probe volume after a given time delay. Figure 2.6 plots this integrated signal (red) as a function of delay between the dissociation and REMPI laser pulses. Each data point represents an average of signal intensities, $[\mathrm{Br}]_{\mathrm{avg}}$. The error bars indicate the standard deviation for related experiments, defined as $0.434 \times [\mathrm{Br}]_{\mathbf{err,\ avg}}/[\mathrm{Br}]_{\mathrm{avg}}$ [134], and are much larger than the errors of each individual signal intensity, $[\mathrm{Br}]_{\mathbf{err}}$.

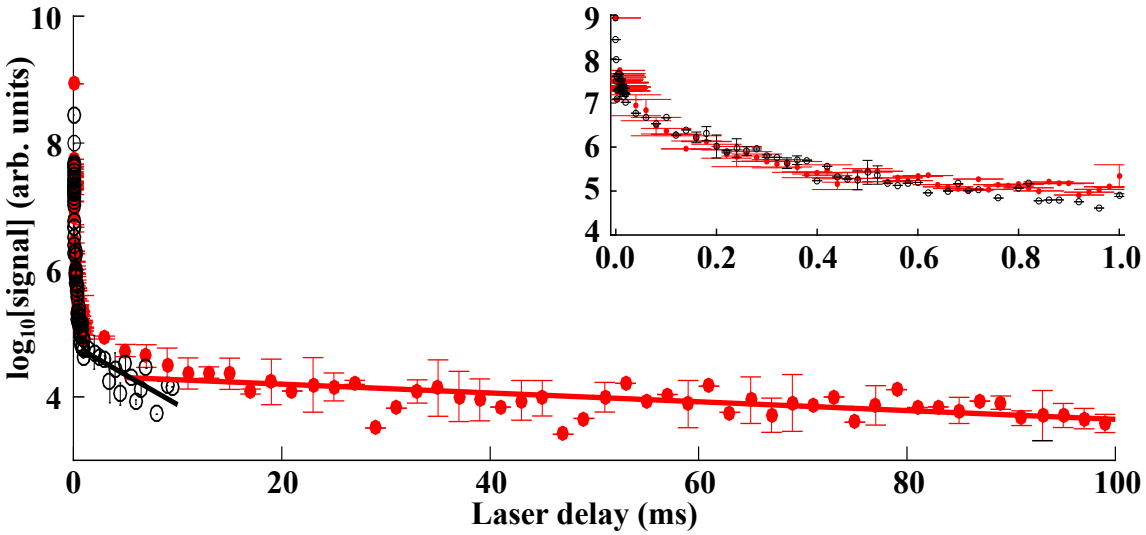

Figure 2.6: Integrated signal as a function of delay between dissociation and ionization; error bars are a standard deviation of repeated experiments. The decay of Br is shown in the presence of a magnetic trap (red) and in the absence of one (black). The inset shows a close-up of the decay at early laser delay times. The solid lines represent a linear least-squares fit performed between 5 ms and 99 ms in the presence of a magnetic trap (or 10 ms in the absence of one). Data in the figure is taken from Rennick *et al.* [122].

Replacing the magnets with Al pieces removes the magnetic field from the interaction region while maintaining the local electric field and physical dimensions of the trap region. The relative density of Br atoms with Al pieces as a function of delay time is plotted as black stars in figure 2.6. Each set of decay traces is built from five smaller sets, taken at smaller ranges of laser delays. At earlier laser delay times, the power in both the dissociation and REMPI lasers are reduced to 2 mJ/pulse to avoid saturation of the MCPs. The set of decay traces with the Al pieces is normalised to that with the magnets.

The notable difference between the two signals is that no atoms are detected beyond 5 ms with no magnetic field present; there is no statistically significant additional signal when the dissociation laser is fired without the magnetic trap. This measurement demonstrates that the magnetic trap is responsible for the long tail in the signal and thus the trapping of Br atoms up to 99 ms.

The integrated signal shows a rapid loss of atoms over the first few hundred microseconds (shown in the inset to figure 2.6), primarily representing the unhindered ballistic expansion of the fastest atoms produced on photodissociation passing through the detection volume. Integrating the distribution of photofragments formed with velocities below the trap depth of 255 mK (calculated in section 4.1), with a maximum velocity of 7.9 m/s, results in 0.4% of the photodissociation yield being trappable, which is consistent with the initial decrease in signal seen in figure 2.6. As the cloud of photodissociation products expands, successively slower atoms leave the probe volume and are irreversibly lost as their kinetic energy exceeds the trap depth. The inhomogeneous magnetic field will trap faster atoms until their trajectory takes them through the saddle point along the z-axis. After 1 ms, the remaining atoms are those with sufficiently slow initial velocities to be trapped in the magnetic field.

During this time, the trapped Br atoms undergo collisions with the molecular beam and background gas, and this decay becomes noticeable after ballistic expansion occurs. As discussed in more detail later, collisions of the trapped atoms with the tail of the molecular beam contribute to the early-time trap losses at laser delays below 5 ms, beyond which collisions with residual gas in the vacuum chamber become distinguishable. The chamber pressure rises to 4×10^{-7} mbar during the experiment, reaching a balance between the gas added via the molecular beam and the pumping speed of the turbo-molecular pump. This background presents an average density of 9.7×10^{9} Ar atoms/cm^3 with a room-temperature Maxwell-Boltzmann velocity distribution.

2.7 Conclusion

Photodissociation of Br_2 produces backscattered Br atomic fragments. The Br atoms in the spin-orbit ground $^2P_{3/2}$ state which scatter parallel to the molecular beam have a

net lab-frame velocity distribution centred on 0 m/s. A fraction of these photostopped Br atoms with a maximum velocity of 7.9 m/s are confined within a magnetic field and observed to a laser delay of 99 ms, up to the next laser pulse. The significance of the observation of signal out to 99 ms with a laser repetition rate of 10 Hz is the potential to build Br density from successive laser pulses.

The accumulation of Br density is limited by the trap loss of Br atoms. Potential causes of trap loss, in particular those due to elastic collisions with the Ar carrier gas, are characterised theoretically in chapter 3 and experimentally in chapter 4. As discussed in section 2.6, elastic collisions with the molecular beam at short laser delays contribute to a significant decrease in Br signal. A new method to decrease this loss using a mechanical chopper construct is discussed in chapter 5. The ability to control the loss of trapped Br atoms and increase density over time is a step towards the creation of a source of cold halogen atoms.

Chapter 3

Controlling Trap Loss of Br Atoms

This chapter discusses and quantifies the three major causes for loss of photostopped trapped Br atoms. The content in this chapter is drawn from Lam *et al.* [121] and Rennick *et al.* [122], as published in the journals *Physical Review A* and *Physical Review Letters*, respectively.

The production of cold Br atoms by photodissociation of Br_2, and confinement of the ground-state atoms in a permanent-magnet trap, can allow the possibility of reloading and accumulation of trapped atom density over successive dissociation laser pulses. However, various losses limit the ultimate density of cold Br atoms that can be maintained in the current experimental set-up.

Three mechanisms for loss of trapped atoms are investigated. These mechanisms are described below in the following order: elastic collisions with the molecular beam, elastic collisions with residual gas in the detection chamber, and Majorana transitions to high-field seeking states. This chapter focuses on theoretical simulations which describe these trap losses, while the experimental work to analyse and minimise these collisions is described in chapters 4 and 5, respectively.

3.1 Monte Carlo simulations

The elastic scattering dynamics of Br atoms with the carrier gas in the molecular beam and effusive background gas is modelled by a Monte Carlo trajectory simulation program. The shell of the simulation is described in the first two subsections, and the specific tools to model the scattering behaviour of the Br atoms are described subsequently.

3.1.1 Overview of methodology of simulation

The simulation models Br atoms over a series of 0.01 μs time steps, converged to ensure that the Br atoms remain indefinitely trapped in the absence of collisions. At each time step, each Br atom first undergoes a ballistic movement, described in section 3.1.2. Next, each Br atom has a probability of undergoing an elastic collision with a carrier-gas atom in the molecular beam, as well as a carrier-gas atom in the thermal background at a pressure of 4×10^{-7} mbar, both described in sections 3.1.3 and 3.2.2. If the position of the Br atom is located beyond the boundaries of a $2 \times 2 \times 4$ mm rectangular prism-shaped region between the two bar magnets, the Br atom is determined to be lost. Because the velocity and position of each Br atom is calculated only once at the beginning of each time step, a collisional trap loss is determined in the next time step.

In this simulation, inelastic collisions between the trapped Br atoms and the Ar in the molecular beam and carrier gas are ignored. In the absence of an external magnetic field, the large spin-orbit splitting of the Br doublet renders such spin-orbit inelastic collisions unlikely to occur [135]. However, near the centre of the magnetic trap, the splittings among the 6 different m_J energy levels, shown in figure 2.4, are close enough for an inelastic Br–Ar collision to be possible. In such a case, a Br atom may transition to either a high-field seeking state (unbolded lines in figure 2.4) or

a low-field seeking m_J state experiencing a lower trap depth (described in Sections 3.2.2 and 4.1). Further work is needed to model inelastic Br–Ar collisions under these conditions.

Elastic and inelastic collisions between pairs of trapped Br atoms are not explored in this thesis. The multitude of possible transitions among the m_J sub-states of the two ^{2}P spin-orbit states of these open-shell atoms during a collision is non-trivial, and there is little literature that maps the potential energy surfaces (PESs) with accurate inclusion of spin-orbit coupling to enable determination of the collision dynamics between two Br atoms. Nonetheless, the density of Br atoms is sufficiently low that the probability of a bimolecular collision between two Br atoms is very small compared to collision with an Ar atom. As the rates of decay of trapped atoms shown in figures 2.6, 4.2, and 4.4 indicate, our experimental measurements are well described by elastic collisions between Br and Ar in the molecular beam and thermal background gas species. This implies that any contribution from Br-Br collisions is very small compared to other factors.

3.1.2 Movement of simulated Br atoms

The distribution of positions and velocities of the Br atoms is chosen to mimic the experimental conditions outlined in Chapter 2. A supersonic molecular beam of 8% Br_2 in an Ar carrier-gas is generated from a pulsed Series 9 valve with a 3 bar backing pressure. The Br_2 is photodissociated 10 cm down the molecular beam path by a 460 nm laser. As described in Chapter 2, the trapped Br fragments are all assumed to be in the spin-orbit ground $^2P_{3/2}$ state. The trapped Br atoms in the excited $^2P_{1/2}$ state are neglected; because their Zeeman potential energies are three times lower than those in the ground state, fewer of them will have sufficiently low translational energies to remain trapped. Furthermore, these excited state Br atoms are not observed

experimentally as the REMPI laser is tuned to ionise only Br($^2P_{3/2}$).

The trapped Br atoms are simulated by numerically integrating the equations of motion, including the effect of the trapping field. At each half-time step, the positions and velocities of each Br atom are calculated from a Verlet integration specific to Newton's equations of motion, using the acceleration, **a**, due to the trapping field, described in equation 2.6 in Chapter 2 [136]. The field around a single bar magnet is determined analytically, and the field within the two-magnet trap, **B**, is determined from the contribution from each magnet assuming minimal demagnetisation [125]. The gradient vector of the magnetic field strength, $\nabla\mathbf{B}$ (where $\nabla = \frac{\mathrm{d}}{\mathrm{dx}}\hat{i} + \frac{\mathrm{d}}{\mathrm{dy}}\hat{j} + \frac{\mathrm{d}}{\mathrm{dz}}\hat{k}$), is calculated using the additive properties of a Laplace equation of the field lines between the two bar magnets, using the same coordinate positions of the Br atoms [125]. Figure 3.1 shows the position of Br atoms in the trap volume 100 μs after they are initially formed.

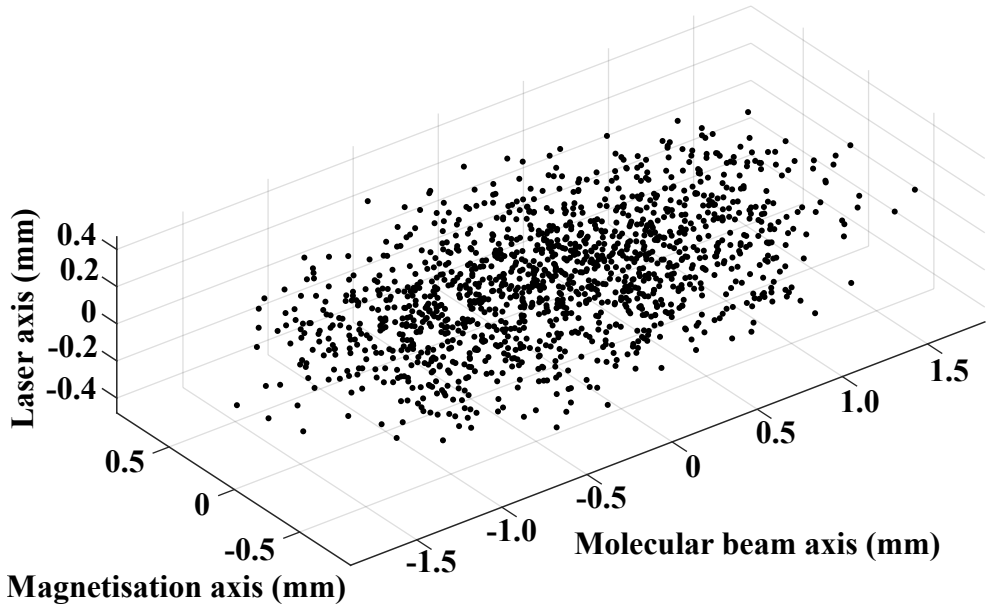

Figure 3.1: Position of simulated Br atoms 100 μs after they are initially formed.

The distribution of Br atoms shown in figure 3.1 has been compared with that

at 50 μs after the Br atoms are initially formed. The two distributions appear very similar, indicating that, in the absence of collisions or other external forces, a group of low-energy Br atoms typically remain in the trap volume. In the experiment, the permanent magnets may not be perfectly aligned. In this case, the magnetic field lines may not be fully symmetric along each axis, therefore decreasing the overall trap depth.

3.1.3 Elastic collisional dynamics of Br and Ar atoms

At each time step, each Br atom is assigned a random number taken from a uniform distribution between 0 and 1. A collision is deemed to occur with a carrier-gas atom, Ar in this case, if this number is less than the probability of a collision, P,

$$P = \rho_{\mathrm{Ar}} \cdot \sigma_{\mathrm{Br–Ar}} \cdot v_{\mathrm{rel}} \cdot \delta t, \tag{3.1}$$

where ρ_{Ar} is the density of the carrier-gas atoms in the trapping region, $\sigma_{\mathrm{Br–Ar}}$ is the integrated elastic cross section, which is dependent on the angular distribution of the collision products and which takes into account the trap depth (described in section 3.2), v_{rel} is the relative velocity between the Ar and Br atoms, and δt is the simulation time step of 0.1 μs. The Ar velocity is chosen from a Gaussian distribution centred at a lab-frame velocity of 560 m/s, with a spread of velocities of 46 m/s at a translational temperature of 10 K. As the molecular beam is formed about 11 cm from the magnetic trap, geometric constraints mean that an Ar atom will only pass through the two bar magnets if it has a perpendicular velocity vector with a magnitude less than 10 m/s; thus, the velocity spread of 46 m/s serves as an upper limit to the energy transfer for collisions between Br and Ar in the molecular beam in the simulation.

The velocities of Ar in the background gas are chosen from a room temperature Maxwell-Boltzmann distribution at 300 K, and in the molecular beam, from a Gaus-

sian distribution of velocities centred on the terminal velocity of the molecular beam with a temperature spread of 10 K. In the room-temperature background gas, at base pressure in the detection chamber, ρ_{Ar} is estimated to be 1.3×10^{10} cm^{-3}. The total number of Ar atoms in the beam is the area under the tail of the molecular beam, integrated from the time of dissociation, and is treated as equivalent to a molecular beam in the shape of a rectangular pulse with a height equal to the peak density of the molecular beam and a duration of 70 μs. In section 4.2, the peak density of the molecular beam, ρ_{Ar}, is measured to be 3.0×10^{13} cm^{-3}.

3.2 Incorporating characteristics of the differential cross sections (DCSs) for Br–Ar elastic collisions into the simulation

The use of the integrated elastic cross section, $\sigma_{\mathrm{Br–Ar}}$, in the theory outlined in section 3.1.3 must take into account the angular distribution of the collision products and its effect on the trapping probability. In this section, the DCS is calculated and used to compute $\sigma_{\mathrm{Br–Ar}}$.

3.2.1 Calculating the DCS for Br–Ar

To calculate the DCS, a quantum scattering approach is used, which propagates a log-derivative wavefunction along the radial Br–Ar potential energy surface. Matching the log-derivative matrix to the asymptotic solutions at a large interatomic separation yields the scattering matrix, from which the DCS is extracted [135,137]. The scattering wavefunction in a central potential is represented by a partial wave expansion in a basis of Legendre polynomials, $P_l(x)$.

The DCS for a collision of energy, E, is then given by [121]:

$$d\sigma/d\Omega(\theta; E) = \frac{1}{4\mu^2 E^2} \sum_l |(2l+1) S_l(E) P_l(\cos\theta)|^2 , \tag{3.2}$$

where $S_l(E)$ is the energy-dependent scattering matrix element, derived in Appendix 2, and μ is the reduced mass of the collision system.

The Br–Ar interaction potential has been determined from crossed molecular beam collision experiments in an energy range comparable to collisions of thermal Ar with trapped Br [135].

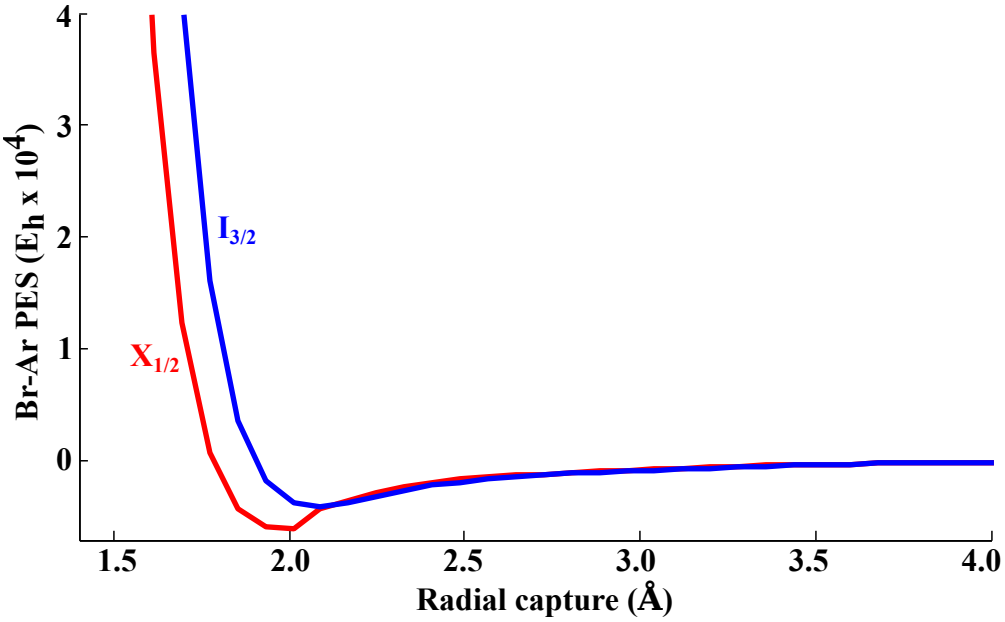

Figure 3.2: Potential energy surfaces of the Br–Ar $X_{1/2}$ (red) and $I_{3/2}$ (blue) molecular states [135]. For reference, the collision energy between a stationary Br atom and an Ar atom moving at the terminal velocity in the molecular beam (560 m/s in the lab frame) is 1.8×10^{-4} E_h, and an Ar atom moving at the median velocity in the background gas (350 m/s in the lab frame), is 7.0×10^{-5} E_h.

The Br–Ar complex can interact on two PESs, shown in figure 3.2, corresponding to a higher-energy molecular state ($I_{3/2}$, blue) and a lower-energy molecular state ($X_{1/2}$, red). The strong spin-orbit coupling means that the electron orbital angular momenta remain coupled throughout the collision, and the coupling between the adiabatic states

of the Br–Ar molecular system is weak. The collision can thus be modelled purely elastically on each of the adiabatic potential energy curves. The centro-symmetric potential is weakly attractive, with a well-depth of about 100 K, and strong short-range repulsion.

At each collision energy, the DCS is computed along each PES, and a summation along all scattering angles results in a total integrated cross section (ICS), where a scattering angle, θ, is defined as the angle between the initial and final axes of propagation of a pair of Br and Ar atoms colliding in the scattering frame, shown in figure 3.3.

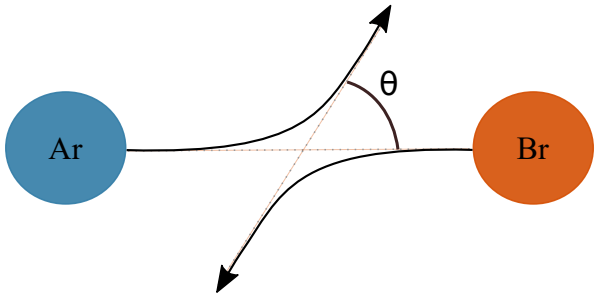

Figure 3.3: Diagram of the Br–Ar scattering system. The scattering angle, θ, is defined in equation 3.4.

The DCS is then weighted by the collision energy distribution function $f(v_{\mathrm{Ar}})$, taken as the Maxwell-Boltzmann speed distribution of Ar [121]:

$$\langle d\sigma/d\Omega f(v_{\mathrm{Ar}})\rangle = \left(\frac{m_{\mathrm{Ar}}}{2\pi k_{\mathrm{B}}T}\right)^{3/2} \times \int_0^{\infty} d\sigma/d\Omega 4\pi v_{\mathrm{Ar}}^2 \exp\left\{-\frac{m_{\mathrm{Ar}}v_{\mathrm{Ar}}^2}{2\mathrm{k_B T}}\right\} dv_{\mathrm{Ar}}, \qquad (3.3)$$

where v_{Ar} is the velocity of the Ar atom in the laboratory frame, m_{Ar} is the mass of the Ar atom, $\mathrm{k_B}$ is the Boltzmann constant, and T is average temperature.

Because the Br–Ar scatters along two PESs converging to the $X_{1/2}$ and $I_{3/2}$ molecular states, as shown in figure 3.2, the total DCS for a $\mathrm{Br}(^2\mathrm{P}_{3/2})$–$\mathrm{Ar}(^1\mathrm{S}_0)$ collision is a weighted average of the individual DCSs derived from each of these PESs, $\mathrm{DCS_{Br–Ar}}$

$= 0.487 \times \mathrm{DCS}_{X_{1/2}} + 0.513 \times \mathrm{DCS}_{I_{3/2}}$ [135, 137].

Figure 3.4 shows a portion of two DCSs, weighted along the two PESs for the $\mathrm{Br}(^2\mathrm{P}_{3/2})$–$\mathrm{Ar}(^1\mathrm{S}_0)$ scattering frame, at an average collision energy in the molecular beam (blue) and median collision energy in the thermal background gas (red).

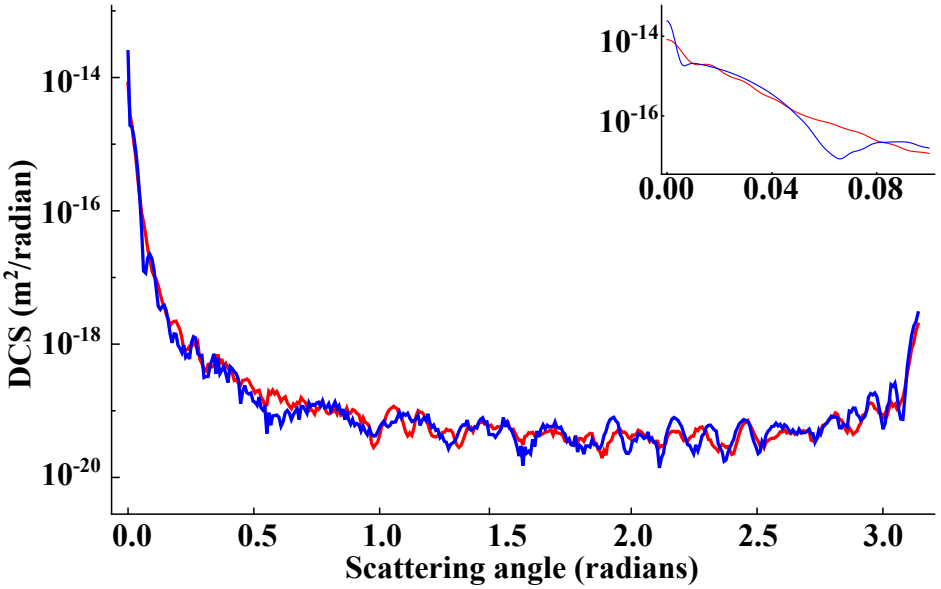

Figure 3.4: $\mathrm{Br}(^2\mathrm{P}_{3/2})$–$\mathrm{Ar}(^1\mathrm{S}_0)$ DCS for collisions with the molecular beam (blue) and thermal background gas (red). The inset is a close-up view of the DCS at scattering angles below 0.1 radians.

In both cases, the DCS peaks lie at low scattering angles. The inset graph in figure 3.4 shows that at the extreme end of total forward-scattering (0 radians), the magnitudes of both DCSs are larger by a factor of 10^3, compared with that at a scattering angle of 0.1 radians. A forward-scattering characteristic implies that there is little energy transfer between the Ar and Br atoms, and thus little change in momentum, during a collision, compared with a backward-scattering motion, in which the two atoms nearly swap momenta and thus recoil in opposite directions [138]. The energy transfer between the Ar and Br atoms, shown in equation 3.4, is related to the

scattering angle, θ, by [139]

$$\Delta \mathrm{E} \cong \frac{\mu}{m_{\mathrm{Br}}} \left| v_{\mathrm{rel}} \right|^2 (1 - \cos\theta), \tag{3.4}$$

where ΔE is the change in energy and μ is the reduced mass of the Br–Ar system. A small scattering angle means a small value of ΔE, and thus a low transfer of energy from the Ar to the Br atom. As the Br–Ar DCSs are strongly forward-peaked, the majority of collisions will result in low scattering angles, and therefore small values of ΔE. For a single collision to eject an atom from the trap, it must increase the kinetic energy of the trapped atom to overcome the trapping potential, U_{trap}. This defines a minimum scattering angle, θ_{min},

$$\theta_{\mathrm{min}} = \arccos\left\{1 - \frac{m_{\mathrm{Br}} U_{\mathrm{trap}}}{\mu^2 \left| v_{\mathrm{rel}} \right|^2}\right\}. \tag{3.5}$$

The ICS for trap loss is given by the integral of the DCS, using the minimum collision angle as a lower bound [122]:

$$\sigma(\theta_{\mathrm{min}}, v_{\mathrm{r}}) = \int_{\theta_{\mathrm{min}}(v_{\mathrm{r}})}^{\pi} (d\sigma/d\Omega) d\Omega. \tag{3.6}$$

Figure 3.5 shows the values for the ICSs of the Br–Ar scattering across a range of relative velocities.

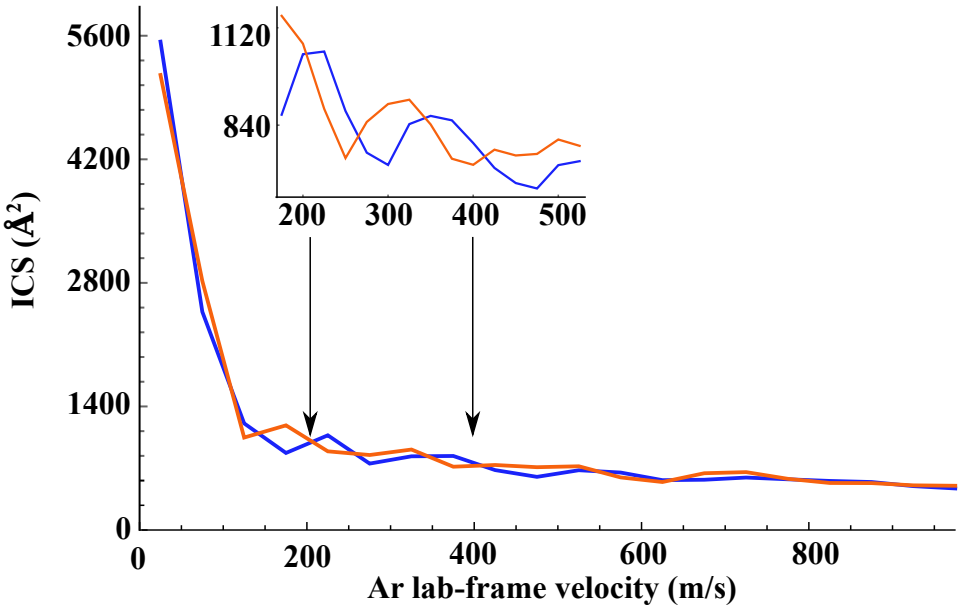

Figure 3.5: Distribution of the ICSs for the Br($^2P_{3/2}$)–Ar($^1S_0$) scattering across a range of collision energies described by the velocity of the Ar in the lab frame (x-axis). This range makes up the Maxwell-Boltzmann velocity distribution for thermal Ar in the background gas. The inset shows the range of Ar velocities within the molecular beam with a 10 K velocity spread.

The ICSs for the Br($^2P_{3/2}$)–Ar($^1S_0$) scattering are shown across a range of collision energies. To calculate the final ICS for the Br–Ar scattering for background gas collisions, the individual DCSs which make up each of these ICSs are weighted across a Maxwell-Boltzmann distribution of velocities shown on the x-axis of figure 3.5. With the molecular beam, the DCSs are weighted across a Gaussian centred on the peak velocity of the molecular beam with a 10 m/s velocity spread, shown on the x-axis in the figure inset. The ICSs are calculated using equation 3.6 over spherical coordinates.

It is interesting to note that the values of the ICSs increase significantly at velocities below 150 m/s. There is very little experimental data on the ICSs taken for the Br–Ar scattering system, and that available for the Br–Ar scattering system exists at collision energies of or above 2.9 kcal/mol, equivalent to velocities of 780 m/s [135, 137]. To calculate the cross sections shown in figure 3.5, the parameters for the propagation of the log-derivative wavefunction (described in Appendix 2) were initialised to values

that enabled the ICSs to match those reported in literature, and then varied to ensure convergence of the parameters over the sum of all scattering matrix elements at each collision energy. A possible explanation of the divergence of the calculated ICSs in figure 3.5 may be that, as the PES used for the Br–Ar scattering system is fitted to measurements at much higher collision energies [135], this fit may be out of the range of validity for low collisional energies. Nonetheless, the ICSs in this range contribute only a small proportion, and thus very little contribution, to the total ICS weighted over a Maxwell Boltzmann distribution of Ar lab-frame velocities. Thus, for the purpose of this thesis, the distribution of ICSs in figure 3.5 can be used as an appropriate estimate of the true ICS.

3.2.2 Using DCSs to determine post-collisional velocities of trapped Br atoms

To determine the value of ΔE at each simulated collision, a cumulative distribution function (CDF) is generated from the DCS. The CDF represents the likelihood that a collision will result in at or below a particular value scattering angle, which can be translated to a particular value of ΔE using equation 3.4.

Figure 3.6 shows the CDF generated by the DCS in the collisions between trapped Br and Ar in the molecular beam (blue) and thermal background (red).

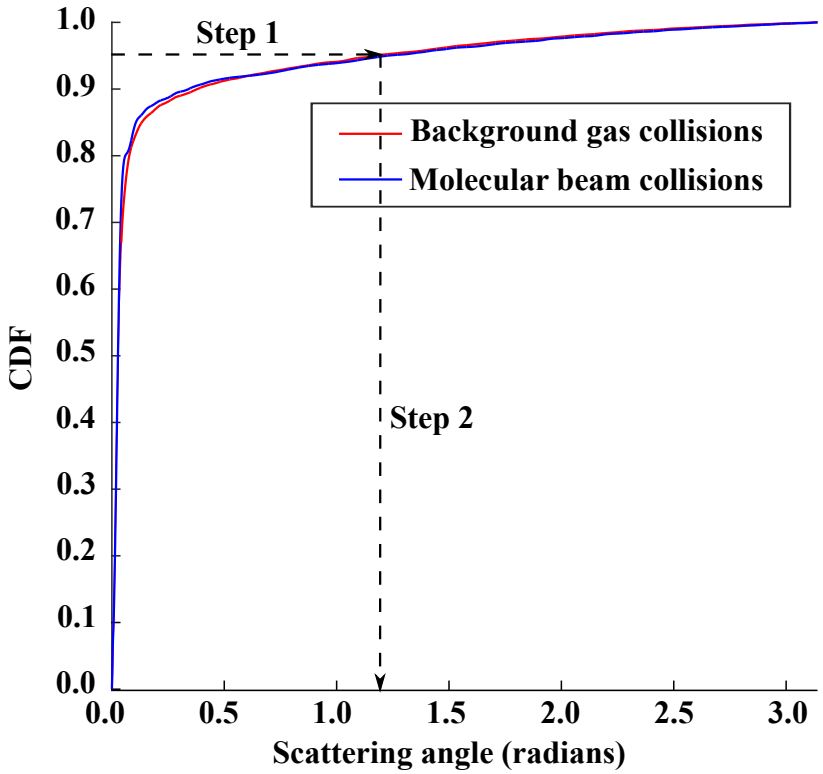

Figure 3.6: Normalised CDF at a range of scattering angles for Br–Ar collisions with the molecular beam (blue) and thermal background gas (red). The CDFs are derived from the DCS figure 3.4. In each Monte-Carlo time step, a uniform random number between 0 and 1 is chosen and corresponds to a point on CDF (Step 1), which in turn corresponds the scattering angle used for the simulation (Step 2), as illustrated by the dashed arrows. Larger scattering angles have a value close to 1.

The asymptotic value of each CDF is equal to 1. In each Monte-Carlo time step, for each Br–Ar collision, a random number is chosen from a uniform distribution between 0 and 1, which matches a unique value on the CDF (Step 1). This value determines the scattering angle of the corresponding Br–Ar system (Step 2) and therefore determines the final momentum vector of the Br atom. Thus, the CDF effectively enables random scattering angles, which follow the same distribution as the DCS, to be chosen for the simulation.

In the molecular beam, using equation 3.4, the minimum scattering angle required for a trapped atom to gain enough energy in a single collision to overcome the magnetic trapping potential ($\theta_{\text{min, Ar, molecular beam}}$) is equal to 1.4°, or 0.024 radians, which

corresponds to 57% of all collisions occurring with Ar in the molecular beam. In the thermal background, this minimum scattering angle ($\theta_{\text{min, Ar, thermal background}}$) is equal to 2.8°, or 0.048 radians, which corresponds to 29% of all collisions with Ar in the thermal background. Scattering angles below θ_{min} will transfer insufficient energy to the Br atoms to facilitate their escape from the trap, so at least one more collision would be required for them to leave the trap volume.

3.3 Using characteristics of the dissociation laser to determine density and trap depth

In order to perform realistic simulations of collisional loss, it is important to have a good estimate for the number and density of the initially trapped Br atoms. The total number of Br atoms trapped is calculated as follows [140]. The minimum beam diameter at the focal point of the laser is

$$w_0 = (2\lambda f)/\pi d_0, \tag{3.7}$$

where λ is the photolysis laser wavelength (460 nm), f is the focal length of the lens directing the laser beam into the chamber and equal to 300 mm, and d_0 is the initial diameter of the beam at the position of the focusing lens and measured to be 3 mm. The diameter of the laser beam as a function of position from the centre of the trap is

$$w(z_l) = w_0\sqrt{1 + \left(\frac{z_1\lambda}{\pi w_0^2}\right)^2}\,. \tag{3.8}$$

Using equations 3.7 and 3.8, the upper limit to the intensity of the laser beam, $i_{\text{laser}}(r, z_1)$, is calculated by assuming a Gaussian distribution of photons centred along

the axis of the laser beam,

$$i_{\text{laser}}(r, z_l) = i_0 \left(\frac{w_0}{w(z_l)} \right)^2 \exp\left\{ -2r^2/w(z_l)^2 \right\}, \tag{3.9}$$

where r is the radius from the trap centre in the plane perpendicular to the molecular beam axis, z_l is the distance along the laser beam axis from the centre of the trap and perpendicular to r, and i_0 is the peak photon intensity and equal to $(2/\pi w_0^2)\mathrm{P}_0$ (where P_0 is the total power in the beam).

The intensity of a supersonic gas expansion (particles per steradian per second) is given by [16]

$$I_0 = 1/8 f(\gamma) n_0 u_0 r^2, \tag{3.10}$$

where n_0 is the source number density, u_0 is the source peak velocity, and r is the radius of the nozzle. $f(\gamma)$ is a function of the heat capacity ratio, γ [16]:

$$f(\gamma) = \sqrt{\frac{\gamma}{\gamma+1}} \left(\frac{2}{\gamma+1} \right)^{\frac{1}{\gamma-1}}. \tag{3.11}$$

In the case of the mixture used here, gas properties are given by the mass-weighted mean of the components. The number density at the laser interaction region is then given by $n = I_0/u_\infty d^2$, where u_∞ is the terminal velocity of the molecular beam, and d is the distance from the nozzle to the interaction region. This simple gas dynamic model predicts a peak Ar beam density, $D_{\max}$, of $3.9 \times 10^{13}\,\mathrm{cm}^{-3}$ [130]. Using $D_{\max}$ and equations 3.9 and 3.8, the density of molecules in the laser interaction volume at a particular distance from the centre of the trap, $D(r, z_l)$, is a function of the density of the molecular beam and the shape of the laser,

$$D(r, z_l) = i_{\text{laser}}(r, z_l) D_{\max} \exp\left\{ -r^2/2d_{\text{flight}}^2 \right\}, \tag{3.12}$$

where d_{flight} is the distance from the nozzle to the centre of the trap.

The fraction of trappable velocities V_{F}, given in equation 3.13 at a given trap coordinate, is a function of a Gaussian distribution of velocities in the molecular beam, $F_{\text{MB}}(v(\Theta))$, where $v(\Theta)$ is the velocity of trappable speeds, and the photofragment angular distribution, $I(\Theta)$, in equation 2.3, integrated over all trappable velocities ($v(\Theta)$) and over all angles from the molecular beam axis (Θ),

$$V_{\text{F}} = \int_{-\Theta_{\text{max}}}^{\Theta_{\text{max}}} \int_{-v_{\text{max}}(\Theta)}^{v_{\text{max}}(\Theta)} F_{\text{MB}}(v(\Theta)) I(\Theta) dv(\Theta) d\Theta, \tag{3.13}$$

where Θ is equal to $v_{\perp}/v_0$ where $v_{\perp}$ is the velocity perpendicular to the peak velocity of Ar in the lab-frame, v_0. Considering only the Br atoms in the spin-orbit ground $^2\text{P}_{3/2}$ state, the maximum trappable velocity in the centre of mass frame, and thus the maximum value of $v_{\perp}$, is 7.9 m/s. At each value of $v_{\perp}$ and corresponding Θ, the velocity parallel to the direction at which a photodissociated Br fragment recoils, v_{r}, is equal to $v_0/\sin(\Theta)$. Thus, the range of velocities, $[-v_{\text{max}}(\Theta), v_{max}(\Theta)]$, over which $V_{\text{F}}(v, \Theta)$ is integrated in equation 3.13, is calculated to be $[-(v_{\text{r}} - v_0), (v_{\text{r}} - v_0)]$. The subset of Br atoms with trappable velocities can be visualised in the density plot in figure 3.7.

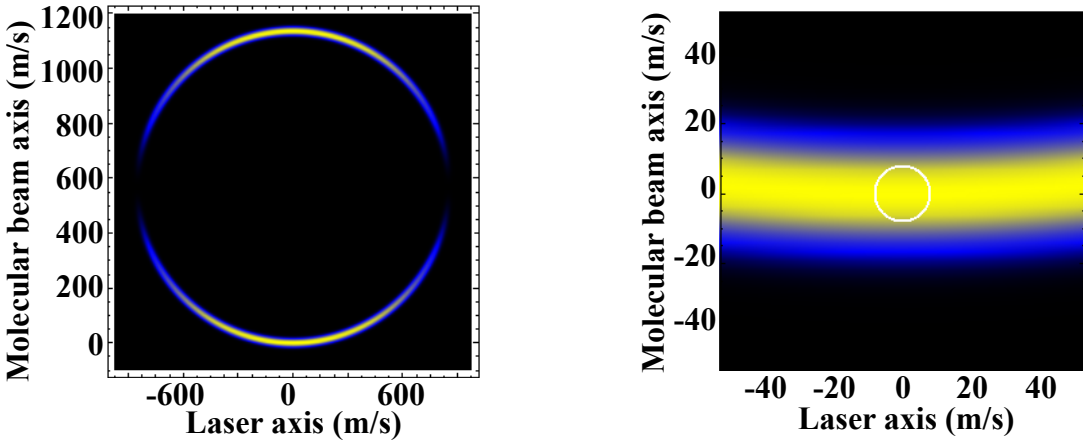

Figure 3.7: Density plot of velocity distribution of photodissociated Br atoms in the lab-frame. The two rings indicate the distribution of recoil velocities in the lab-frame, with the magnetisation axis perpendicular to the page. The velocities that represent trappable Br atoms lie within the white circle at the bottom of the right hand figure. The figure is adapted from figure 4.5, page 91, *Ultracold atom production via photodissociation of small molecules*, by W. Doherty, 2012, with permission from the author [130].

Using equations 3.12 and 3.13, the total number of Br atoms trapped per laser shot, N_{Br}, is a function of the trap volume and density of Br atoms in the laser interaction region, integrated over the volume of the trap,

$$N_{Br} = \int_{\text{trap volume}} V_F(r, z_l) \times D(r, z_l) dr dz_l. \tag{3.14}$$

A factor of 2, arising from 2 Br atoms being formed per dissociation of a Br_2 molecule, is cancelled out by the fact that 50% of the Br atoms formed in the branch indicated by equation 2.1 are in the spin-orbit ground $^2P_{3/2}$ state.

The 5 ns, pulsed, photodissociation laser is focused into the magnetic field minimum, and the minimum beam diameter at the focal point of the laser, w_0, is measured to be 750 μm. Thus, the photodissociation laser effectively illuminates a 750 μm diameter cylinder, which overlaps with the molecular beam at the centre of the trap. The peak density of atoms formed here expands to fill the trap on a microsecond time scale, reducing the density of Br atoms by a factor of 2.6. Integrating the trapped

fraction over the illumination volume of the dissociation laser, the density of the trapped ground-state atoms is estimated to be, in its upper limit, 1.1 $\times 10^8$ cm^{-3} and 2.0 $\times 10^8$ cm^{-3} in the $m_J = 1/2$ and $m_J = 3/2$ sub-states, respectively, corresponding to $N_{Br,(J=3/2,m_J=1/2)} = 4{,}320$ atoms in the $m_J = 1/2$ state and $N_{Br,(J=3/2,m_J=3/2)} = 7{,}970$ atoms in the $m_J = 3/2$ state. Under these conditions, a density of 3.5 $\times 10^7$ cm^{-3} spin-orbit excited $^2P_{1/2}$ atoms is also trapped, which corresponds to $N_{Br,(J=1/2,m_J=1/2)} = 1{,}340$ atoms.

3.4 Results of simulation

The Monte Carlo simulation of collisional losses is run with an initial set of 1370 Br atoms formed by photodissociation, the amount chosen such that the size of the arrays used to store the properties of each Br atom lie just below the maximum value before exceeding computational memory, and thus, each simulated Br atom represents 5.8 real Br atoms in the experiment. The number of collisions occurring in the trap is proportional to the duration of the molecular beam, which is set at 130 μs to mimic the experiment. The probability of collisions and the energy transfer for elastic collisions is treated as described in sections 3.1.3 and 3.2, respectively. During each period of 0.1 s, a new molecular beam pulse occurs, and thus a new set of 1370 Br atoms, are added to the trap.

Figures 3.8 and 3.9 show the distribution of velocities of Br atoms (each atom indicated by a red or blue data point) immediately after escaping the trap potential due to elastic collisions with the Ar in the molecular beam and/or background gas. The asymmetry of the velocity distribution of these lost Br atoms is directly tied to the DCS used in the elastic collisions responsible for the trap losses. In both figures, the plots using a 130 μs molecular beam pulse are indicated by the blue data points on the left. As a comparison, the plots using a shortened molecular beam pulse, with

its duration reduced by a factor of 10 to 13 μs, are indicated by the red data points on the right. For both cases, the velocity distributions appear the same. As expected, the duration of the molecular beam should not influence the angular distribution of the collisional products, and thus, it should have no effect on the velocity distribution of the Br atoms lost from the trap.

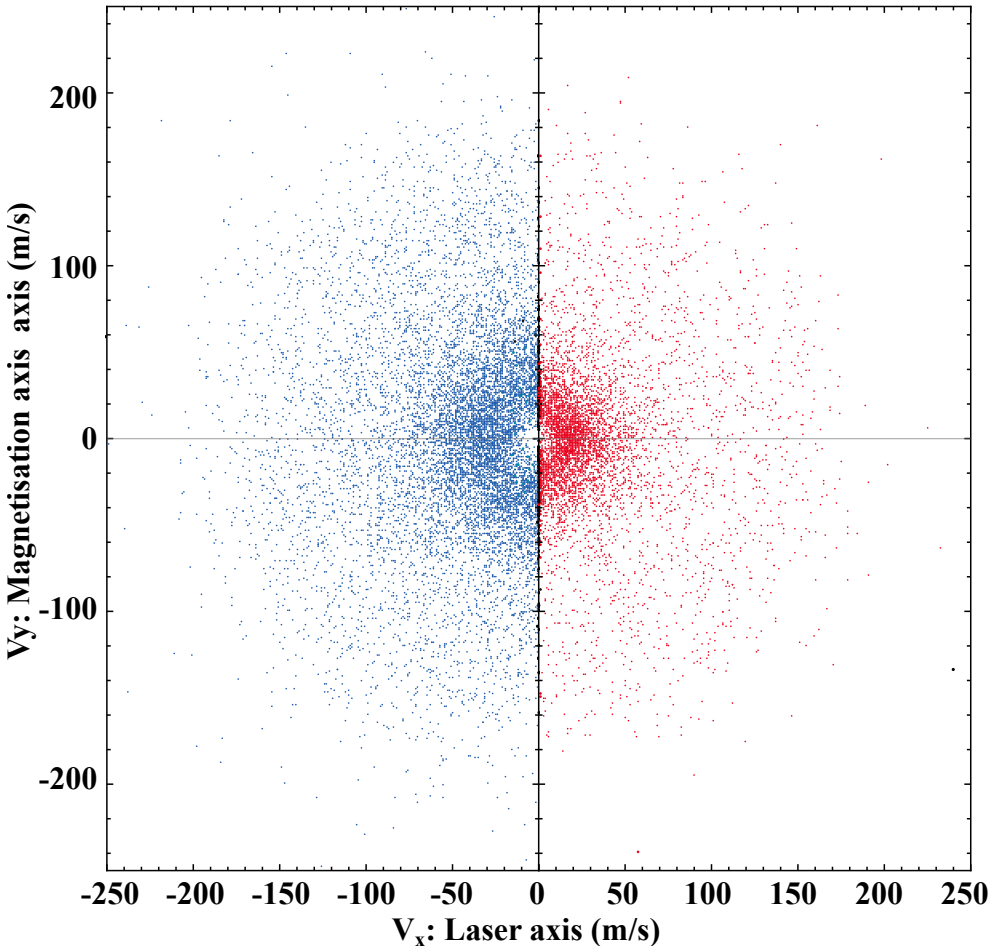

Figure 3.8: Velocity distribution of Br atoms in the lab-frame, just after undergoing trap loss collisions with the molecular beam and background gas. The molecular beam axis is perpendicular to the page. The cases in which the duration of the molecular beam is 130 μs (blue, left) and 13 μs are compared.

Figure 3.8 shows a symmetric velocity distribution along the axes perpendicular to the propagation direction of the molecular beam. Each of these values indicate the velocity of the Br atom immediately after undergoing the final collision that results in

a trap loss. Thus, some of these velocities might be a sum of several collisions. The gap in the centre of the graph, with velocities close to 0 m/s, represents the impossibility of an initially trapped Br atom to escape the trap potential without adequate kinetic energy.

In contrast, figure 3.9 shows a very different velocity distribution, which includes the direction of propagation along the molecular beam axis (z-axis).

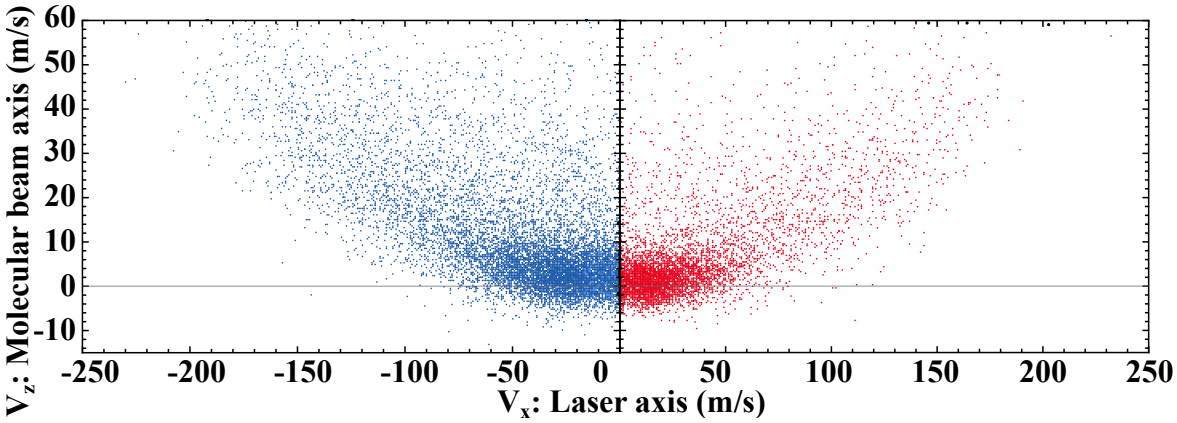

Figure 3.9: Velocity distribution of Br atoms in the lab-frame, just after undergoing trap loss collisions with the molecular beam and background gas. The magnetisation axis is perpendicular to the page. The cases in which the duration of the molecular beam is 130 μs (blue, left) and 13 μs (red, right) are compared.

The velocity distribution of the escaped Br atoms illustrates the propensity for forward–scattering to occur in Br–Ar collisions. This distribution is much smaller along the molecular beam axis and concentrated at positive values of the z-axis near 0 m/s, which is the direction of propagation away from the valve. The small values are due to the majority of collisions resulting in low scattering angles in the Br–Ar scattering frame, described by the CDF in figure 3.6. Thus, most of the momentum transferred from the Ar atom to the Br atom leading to trap escape is in a direction perpendicular to the molecular beam axis. These results illustrate the effects of a distinct forward-scattering DCS along the molecular beam axis.

3.5 A brief exploration of substituting Kr for Ar as the carrier gas atom

The prospect of using Kr as the carrier gas is also explored. A Kr atom is twice as heavy as an Ar atom, and thus, its lab-frame velocity in the molecular beam is centred around 394 m/s, and its median velocity in the thermal background gas is 249 m/s.

The DCS for a collision between a Br atom and a Kr atom in the molecular beam (blue) and thermal background (red) is shown in figure 3.10, weighted across the two PESs, $X_{1/2}$ and $I_{3/2}$, and is similar to those used to model the collisions between Br and Ar [135, 137]. The DCSs in this figure are calculated at the peak velocity of Kr in the molecular beam and at the most probable velocity of Kr in the thermal background. The similarity in the DCSs for the Br–Kr scatter in the molecular beam and thermal background are due to the similar values of their collision energies, in particular, since Kr moves slower than Ar in the molecular beam. The DCS calculated at one velocity can be a good estimate for that averaged over a distribution of velocities, as was calculated with the scattering between Br and Ar in figure 3.4.

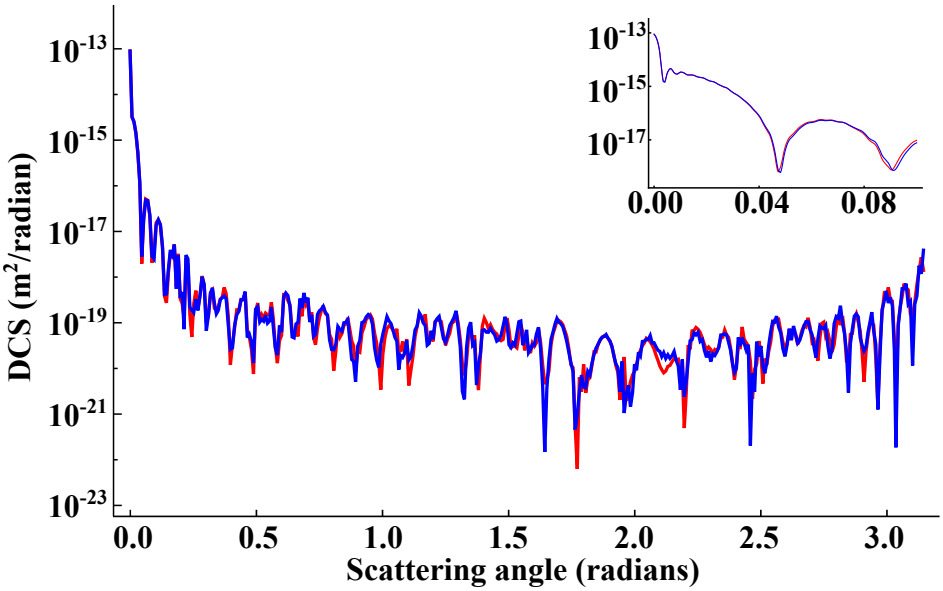

Figure 3.10: DCS for Br with Kr in the molecular beam (blue) and thermal background (red), weighted across the two PESs $X_{1/2}$ and $I_{3/2}$. The inset figure is a close-up of the region below 0.1 radians and, in comparison with figure 3.4, shows that the collision dynamics of the Kr and Ar in the molecular beam and in the thermal background are very similar.

The DCSs of the Br–Kr scattering in the molecular beam (blue) and background gas (red) are nearly overlapped. The inset graph shows that at small scattering angles, collisions between Br and Kr in this energy regime favour forward-scattering, similar to that between Br and Ar in figure 3.4.

Using the equations 3.10 and 3.11 in section 4.2, the peak Kr beam density is calculated to be $6.3 \times 10^{13}\text{cm}^{-3}$ (compared with $3.9 \times 10^{13}\text{cm}^{-3}$ for Ar). Assuming that the ratio of experimental to calculated peak density is similar to that for Ar as a carrier gas (calculated to be 77%, described in section 4.2) the measured peak density of Kr is predicted to be $4.8 \times 10^{13}\text{cm}^{-3}$. Using Kr as the carrier gas, and using the calculation methods in section 3.3, the density of the trapped ground-state, $m_J = 3/2$ sub-state, Br atoms is estimated to be 4.6 $\times 10^8$ cm^{-3} (compared with 2.0 $\times 10^8$ cm^{-3} using Ar as the carrier gas prepared in a molecular beam of Ar), corresponding to 17,450 atoms trapped per laser shot. Hence, the use of Kr as the carrier

gas enables a greater amount of Br atoms to be trapped. At this point, Kr appears to be favoured over Ar as the choice of carrier gas. However, further investigation is necessary to understand the differences between using Kr and using Ar, in relation to collisional trap loss and to accumulating trapped Br atoms over successive molecular beam cycles. These differences are explored in the next section.

3.6 Accumulating Br atoms over successive molecular beam cycles

The investigation of the formation of trapped Br atoms and of subsequent trap loss allows us to better understand the competing processes occurring, and it enables us to work towards producing a cold atom source with sufficient density for reaction studies. In order to gain sufficient density of Br atoms in the trap, the atoms must be accumulated over multiple laser shots, limited by trap loss dynamics, such as those described above. Figure 3.11 illustrates the feasibility of accumulating density in the magnetic trap over successive molecular beam cycles, at a rate of 10 Hz. Each spike corresponds to the loading of a new bunch of Br atoms, followed by the decay due to the collisional losses.

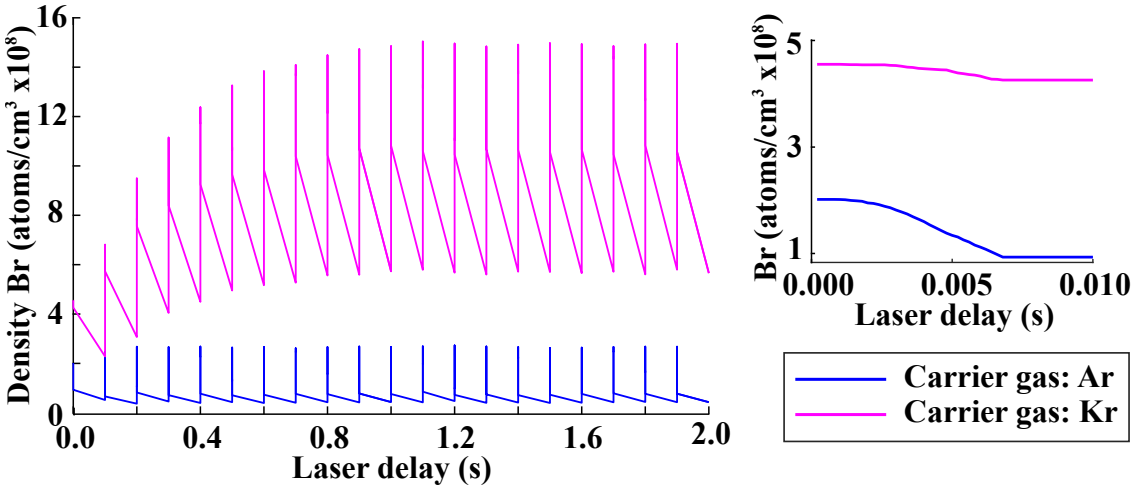

Figure 3.11: Loading curves with Br prepared from a beam of Br_2 seeded in Ar (blue) and in Kr (magenta). The simulations are run over a period of 2 s (left) and each load cycle shows a decay due to collisions with the molecular beam and with the thermal background (right).

Figure 3.11 suggests that using Ar as the carrier gas (blue) does not allow accumulation of trapped Br atoms, whereas that using Kr as the carrier gas (magenta) results in an increase in the amount of trapped Br atoms after one gas pulse, by a factor of 2.5. Taking the density of initially trapped Br atoms, prepared in Kr, to be 4.6 $\times 10^8$ cm^{-3} (calculated in section 3.5), the total density of trapped Br atoms prepared by the accumulation cycle is 5.7 $\times$ 10^8 cm^{-3} (compared with 4.3 $\times$ 10^8 cm^{-3} by using Ar as the carrier gas), reached in just over 1 s, or 10 gas pulses. As a comparison, the total Br density achieved using Ar as the carrier gas is 4.3 $\times$ 10^8 cm^{-3}).

There are several factors that help explain why the use of Kr as a carrier gas results in a greater density of Br atoms in the accumulation cycle. First, as explained in section 3.5, the peak density of Kr in the molecular beam is around 1.6 times greater than that of Ar, thus enabling a greater amount of Br atoms to be initially trapped. Second, during each simulated time step of 1 μs, the probability of a collision occurring, P (defined by equation 3.1.3), is around 16% for Kr, compared to around 20% for Ar. (In the case of Br–Ar collisions in the thermal background, P is around

0.003% and 0.002%, for Kr and Ar, respectively.) Thus, a trapped Br atom is less likely to undergo a collision with Kr than with Ar. Third, the use of Kr as the carrier gas results in fewer single collisions that directly lead to trap loss. Using equation 3.4, the minimum scattering angle for single collisional loss with Kr in the molecular beam, $\theta_{\text{min, Kr, molecular beam}}$, is equal to 2.3°, or 0.040 radians, corresponding to 23% of all collisions (compared with 0.024 radians for Ar, corresponding to 57% of all collisions). For collisions with Kr in the background gas, the minimum scattering angle, $\theta_{\text{min, Kr, thermal background}}$, is equal to 3.7°, or 0.065 radians, corresponding to 20% of all collisions (compared with 0.048 radians for Ar, corresponding to 29% of all collisions). Overall, for the case of producing a high density of trapped Br atoms, the use of Kr as the carrier gas is preferred over Ar.

The right plot in figure 3.11 illustrates the different rates of trap loss due to collisions with the molecular beam, compared with the background gas. In each molecular beam cycle, the decay of Br atoms due to collisions with the molecular beam occurs over 70 μs and at a faster rate than that with the background gas. For example, in the case of using Ar as the carrier gas (blue), at 70 μs immediately after the tail of the molecular beam passes through the magnetic trap, 54% of trapped Br atoms are lost (shown by the steeper decays in the right plot in figure 3.11, from 0.000 s to 0.007 s), comparable to that determined experimentally in figure 4.4. After 0.1 s, collisions with the thermal background gas (at a base pressure of 4×10^{-7} mbar) represent 44% of trapped Br atoms lost (shown by the shallower decays in the right plot in figure 3.11, from 0.007 s to 0.010 s), comparable to that found experimentally in section 4.1.

3.7 Exploring Majorana losses

For long trapping times, trap loss due to Majorana spin flips needs to be considered. When a Br atom moves across a region with a sufficiently small field near the centre

of the magnetic trap, it can change from a low- to a high-field seeking m_J sub-level and is expelled from the trap. Majorana transitions occur when the rate of change of the magnetic field experienced by the atom, $|dB/dt|$, exceeds the Lamor frequency, ω_L [141]. Substituting the notional rate of change of the magnetic field for its spatial gradient and the velocity of a trapped atom yields the relation:

$$\omega_L = \frac{\mu_{\mathrm{B}} B}{\hbar} << \left|\frac{dB}{dt}\right| \frac{1}{B} = \left|\frac{dB}{dr}\right| \frac{v_{\mathrm{Br}}}{B}, \tag{3.15}$$

where $B \equiv B(\mathbf{r})$ is the magnetic field experienced by the trapped Br atom, μ_{B} is the Bohr magneton, v_{Br} is the lab-frame velocity of the Br atom.

The $<<$ sign can be replaced by a scaling factor ζ on the right hand side of the equation, $\frac{\mu_{\mathrm{B}} B}{\hbar} = \zeta \left|\frac{dB}{dr}\right| \frac{v_{\mathrm{Br}}}{B}$, which compensates for the fact that this region is neither rigid nor ideal, and thus ζ allows us to place a more conservative lower limit on the number of spin flips occurring [142].

The gradient of the quadrupole-like field in this trap is linear near the centre, so the inequality in equation 3.15 depends most strongly on the local field magnitude, $B(\mathbf{r})$, and on the trapped particle velocity, v_{Br}. The inequality is most likely to be satisfied, resulting in Majorana transitions to high-field seeking states near the centre of the trap, where v_{Br} is maximum and B is minimum. The contribution of Majorana losses is estimated from classical simulations of the motion of the atoms in the trap.

In the simulation, each Br atom undergoes ballistic movement, as described in section 3.1.2. For simplicity, elastic collisions are omitted. At the end of each time step, each atom is then tested to see if its position and velocity satisfies the condition for Majorana transition to a high-field seeking state; if satisfied, such a transition results in a trap loss. This process is repeated for 1370 simulated Br atoms with random initial positions and velocities, for a total time of 5 s. Figure 3.12 plots the location of each particle as it is lost from the trap.

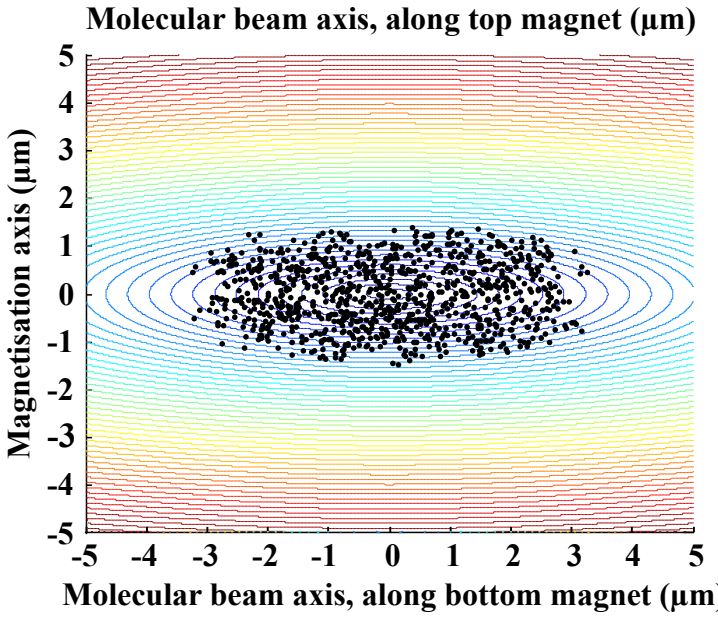

Figure 3.12: A map of the locations near the centre of the trap, at which 200 out of 1370 simulated Br atoms will undergo a Majorana transition after 5 s. The contour lines show a qualitatively description of the magnetic field lines near the centre of the magnetic trap, and the horizontal axis along the page is parallel to the direction of the lasers. The figure is drawn from Lam *et al.* [121].

In this simulation, one set of Br atoms is evolved over 5 s, using ζ scaling factors of 5, 10, and 20, with loss rates of 1.1 atoms/s, 0.5 atoms/s, 0.3 atoms/s, respectively. Setting ζ to equal 20, the positions at which the Br atoms have undergone Majorana transitions are shown by the black dots in figure 3.12, as observed along the axis parallel to the direction of the lasers. The magnets are indicated above and below the figure, and the false-colour fine contour lines show the density of magnetic field lines in this trap.

This procedure provides a very conservative loss rate estimate of 0.3 atoms/s, a rate much lower than that due to elastic collisions.

3.8 Conclusion

The three forms of trap loss which challenge the ability to generate a dense source of trapped Br atoms have been discussed on the basis of theory and simulations in this chapter. Among these, elastic collisions with Ar atoms in the molecular beam and thermal background are the most significant, because a fraction of such elastic collisions transfer sufficient energy to the Br atoms, enabling them to overcome the trapping potential and leave the trap. The energy transferred in a collision depends on the geometry of the collision as $\Delta E(\theta)$ in equation 3.4, where θ is the scattering angle between the initial and final velocity vectors. Equating the trap depth to $\Delta E(\theta)$ defines a minimum collision angle, $\theta_{\min}$, used to compute the ICS for single-collisional loss. Monte Carlo simulations show that elastic collisions with the molecular beam and background gas inhibit the ability to accumulate density of Br atoms over successive molecular beam cycles.

In Chapter 4, these theoretical calculations are compared with experimental observations on the two forms of trap loss caused by elastic collisions between the trapped Br and the Ar in the molecular beam and in the thermal background.

Majorana transitions to high-field seeking states, on the other hand, have been simulated and found to occur very infrequently, with an upper estimate of 1.1 atoms/s. Because these transitions result in a low rate of decay of Br atoms, experimental observation of such transitions requires confinement of Br atoms on the order of seconds, which is currently not feasible in this work. As such, this thesis neglects Majorana transitions and focuses only on minimising collisional losses of Br from the trap.

Chapter 4

Experimental Characterisation of Collisional Trap Loss

This chapter discusses experimental observations on two forms of trap loss caused by elastic collisions between the trapped Br, and Ar in the molecular beam and in the thermal background. The results are compared with the theoretical calculations discussed in chapter 3. Majorana transitions to high-field seeking states are not observed experimentally and are not discussed in this chapter. The content in this chapter is drawn from Lam *et al.* [121] and Rennick *et al.* [122], as published in the journals *Physical Review A* and *Physical Review Letters*, respectively.

4.1 Background gas collisions

The DCS for trap loss arising from a single collision, $\sigma(\theta_{\min}, v_{\mathrm{r}})$, averaged over a Maxwell-Boltzmann velocity distribution of the Ar atoms is given by equation 3.3. The bimolecular rate constant is $k_{\mathrm{bi}} = \langle v_{\mathrm{Ar}}\sigma(v_{\mathrm{Ar}})\rangle$ [122], where $\sigma(v_{\mathrm{Ar}})$ is the ICS for a single Br–Ar collision energy, which is dictated by the Ar atom velocity in the limit of stationary Br atoms. Throughout this chapter, $\langle v\sigma\rangle$ (defined in equation 4.1) is used

as a shorthand notation for $\langle v_{\mathrm{Ar}}\sigma(v_{\mathrm{Ar}})\rangle$:

$$\langle v\sigma\rangle = \left(\frac{m_{\mathrm{Ar}}}{2\pi k_{\mathrm{B}}T}\right)^{3/2} \times \int_0^\infty \sigma(\theta_{\mathrm{min}}, v_{\mathrm{r}}) v_{\mathrm{Ar}}^3 \exp\left\{-\frac{m_{\mathrm{Ar}} v_{\mathrm{Ar}}^2}{2k_{\mathrm{B}}T}\right\} dv_{\mathrm{Ar}}, \tag{4.1}$$

where v_{Ar} is the average velocity of the Ar atom in the laboratory frame, $\mathrm{m_{Ar}}$ is the mass of the Ar atom, k_{B} is the Boltzmann constant, and T is the average temperature.

The trap depth, calculated in chapter 3, can be determined experimentally by measuring the loss rate as a function of chamber pressure, and by modelling the loss by pseudo first-order kinetics. Delaying the REMPI laser pulse with respect to the dissociation laser pulse probes the time-dependent trapped atom density, shown in figure 4.1. The chamber pressure is controlled by a variable leak valve, which allows Ar atoms to flow into the detection chamber.

These measurements are performed under similar operating conditions as those used to produce the Br decays in figure 2.6. The measurements that produce the Br decays in figures 2.6 and 4.1 were performed on separate occasions, between which the experimental apparatus was regularly taken apart and reassembled for maintenance.

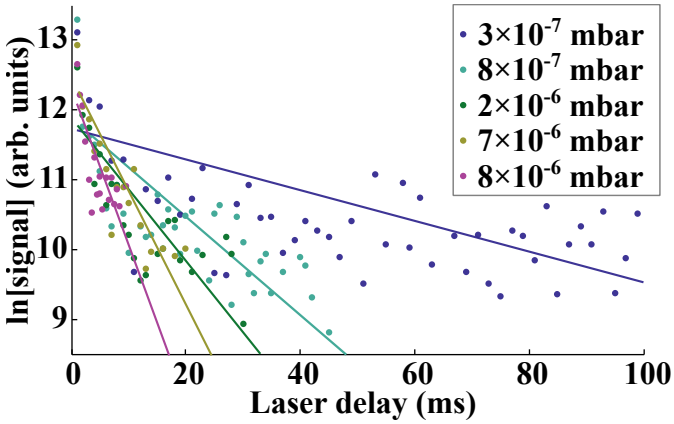

Figure 4.1: Trapped Br atom signal as a function of delay between the dissociation and REMPI lasers for a range of chamber background pressures. The solid lines are fits to a pseudo-first order kinetic model of trapped atom density. The figure is drawn from Lam *et al.* [121].

For a given chamber pressure, the background Ar density is essentially constant

with time, and the trapped Br atom loss rate is well-represented by a pseudo first-order process [121]:

$$\frac{d[\mathrm{Br}]}{dt} = -k[\mathrm{Br}], \tag{4.2}$$

where $k = \langle v\sigma \rangle [\mathrm{Ar}]$ is a pseudo first-order rate coefficient that depends on the Ar density and on the velocity-averaged cross section for trap loss collisions [121]. The integrated form of equation 4.2 fits the experimental data, shown as solid lines in figure 4.1, producing an estimate of k for each Ar background pressure. The loss of Br atoms from the trap from 5 ms to 100 ms is dominated by collisions with Ar in the thermal background (as the molecular beam pulse has ended). This decay process for a given chamber pressure is well described by a single exponential.

Figure 4.2 plots this rate constant as a function of Ar density, established from the pressure gauge and assuming ideal gas conditions, controlled by a leak valve attached to an Ar reservoir.

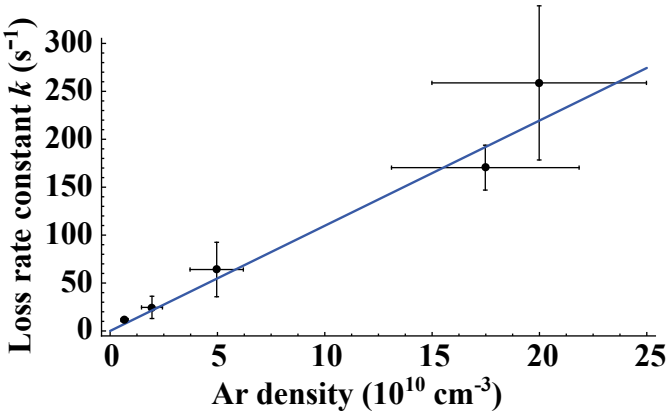

Figure 4.2: Pseudo-first order trap loss rate coefficient as a function of background Ar density. The figure is drawn from Lam *et al.* [121].

Each data point in figure 4.2 represents the gradient of the corresponding decay rate in figure 4.1, with an error bar representing the standard error on the gradient, arising from the scatter in the experimental data. The gradient of figure 4.2 gives an estimate of the velocity-averaged cross section, $\langle v\sigma \rangle = (1.12 \pm 0.09) \times 10^{-9}\,\mathrm{cm}^3\,\mathrm{s}^{-1}$ [121]. This is

the velocity-averaged cross section for collisional trap loss and depends on the Br–Ar ICS, $\sigma(\theta_{\min}, v_{\mathrm{r}})$. Multiple-collisional loss is neglected due to the lack of sensitivity in the experimental set-up to measure trap loss to a higher polynomial order. Using this value for $\langle v\sigma \rangle$ and the pseudo first-order rate in equation 4.2, the percentage of Br atoms that remain trapped after a laser delay of 100 ms (at the end of one molecular beam cycle), after undergoing purely elastic collisions with the background gas at a chamber pressure of 4 $\times 10^{-7}$ mbar, is determined to be (34 $\pm$ 3)%. As a comparison, Monte-Carlo simulations in section 3.6 show that this percentage remaining is 56%. The experimental and theoretical values are not far from one another and a good achievement, given the variety of experimental error that would lead to a greater loss of Br atoms than that predicted by simulation. A source of experimental error may be the instability in the chamber pressure particularly at high chamber pressures, as controlled by the leak valve, and an under-estimation of the Ar density from the measured chamber pressure. Another source may be the inaccuracy in calculating the theoretical cross sections used in the simulations. Future work is needed to further explore and minimise the difference between these experimental and theoretical values.

A fit of the loss rate constant and chamber pressures was performed to a first-order decay rate, given by the integrated form of equation 4.2. Including an estimated 10% error in the chamber pressure, the measured velocity-averaged cross section is $\langle v\sigma \rangle = (1.31 \pm 0.29) \times 10^{-9} \mathrm{cm}^{-3}\mathrm{s}^{-1}$ [122]. Using this value and equations 3.6 and 4.1 defines a value for $\theta_{\min}$ and hence also the trap depth $U_0/k_{\mathrm{B}} = 255$ mK with the upper and lower standard errors $[215, 325]$ mK.

These values are similar to the trap depth calculated from the Zeeman energy shift for a Br atom in the $m_J = 3/2$ sub-state, located at the edge of a magnetic trap (with a magnetic field of 0.22 T); the Zeeman energy shift at this point is calculated to be $U_0/k_{\mathrm{B}} = (322 \pm 36)$ mK [122], where the error corresponds to the error in the field strength under the manufacturer's specifications. The $m_J = 1/2$ sub-state of

the ground, $J = 3/2$, state has a Zeeman shift about 3 times smaller in magnitude, corresponding to a trap depth of (99 ± 9) mK. As discussed in section 2.4, the spin-orbit excited state possesses a Landé g factor half the magnitude of the ground state, and thus its corresponding trap depth for the $m_J = 1/2$ sub-state at this location is calculated to be (56 ± 4) mK.

4.2 Molecular beam collisions

During the earliest period of trap loading, the dominant loss mechanism for trapped Br is collisions with the molecular beam carrier gas. The beam forms on expansion of gas from a high-pressure room temperature reservoir into the vacuum chamber through a 0.5 mm nozzle. This isentropic expansion converts the random thermal motion of room-temperature gas into a high-velocity directed flow with low transverse velocity. The resulting jet has a similar average speed as the room temperature Maxwell Boltzmann distribution, but now predominantly along a single direction.

Collisions between the jet and trapped atoms lead to loss with a similar probability as collisions with the thermal background, but at a higher rate owing to the increased on-axis density. The amount of trapped Br remaining at the end of the molecular beam pulse will therefore depend on two factors: the instantaneous Br_2 density when the dissociation laser is fired (and hence the number of Br atoms produced), and losses from collisions with the cumulative Ar density in the tail of the molecular beam. Exciting at the peak density of the pulse initially produces more Br atoms, but the high loss rate during the remainder of the pulse eliminates this advantage.

Figure 4.3 plots the relative density of the molecular beam as a function of the delay between the valve trigger and the dissociation laser pulse. Although it is the Br atom density that is measured here by the REMPI laser, the ion signal is proportional to the instantaneous Br_2 density as the REMPI laser pulse is coincident with the dissociation

laser pulse. This is also representative of the temporal profile of the relative carrier gas density, assuming minimal velocity slippage with respect to the Br_2 seed molecules. An exponential double-sigmoid function fits to the rising and falling edges, with a decay rate approximately 2.5 times that of the rising edge, and a FWHM duration of 130 μs.

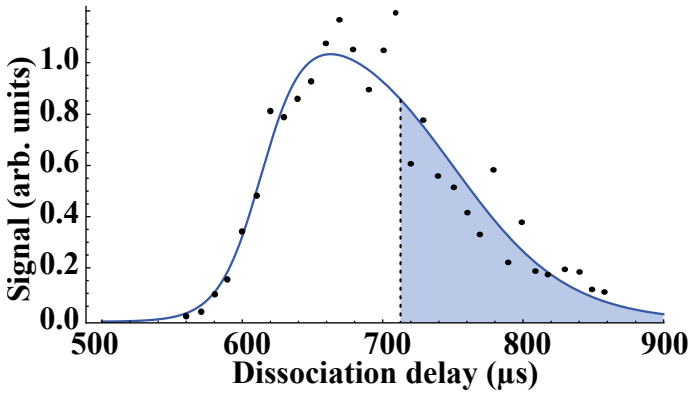

Figure 4.3: Instantaneous molecular beam density, determined from the Br fragment ionisation yield as a function of dissociation delay time, relative to the molecular beam valve trigger. The solid line is a fit to an exponential double-sigmoid function. The shaded region indicates the integration range from the dissociation time to the end of the pulse, used in equation (4.3). The figure is drawn from Lam *et al.* [121].

Measurements of the trapped atom loss rate during the molecular beam pulse are not possible, as there are additional contributions to the observed signal intensity. The high Br_2 density during the molecular beam pulse yields a significant one-colour REMPI signal, as the REMPI laser alone has sufficient energy to dissociate a molecule and ionise the fragments. Immediately after parent molecule dissociation, the atom signal time dependence is a convolution of both trapped atom loss and escape of high-velocity atoms from the probe volume.

The post-molecular beam decay can be described by an exponential decay, the rate of which is only dependent on the background pressure, as shown in section 4.1. Extrapolating each of these fits to $t = 900$ μs gives an estimate of the trapped atom density at the end of the molecular beam gas pulse; this time is defined as the point at

which the measured molecular beam intensity is indistinguishable from the background (Fig. 4.3.) This extrapolated value is then normalised by the molecular beam density at the instant of excitation to account for the Br_2 density during photodissociation. Figure 4.4 plots this relative trapped atom fraction as a function of dissociation time, and it shows that exciting later in the molecular beam permits survival of a greater fraction of the original atom density.

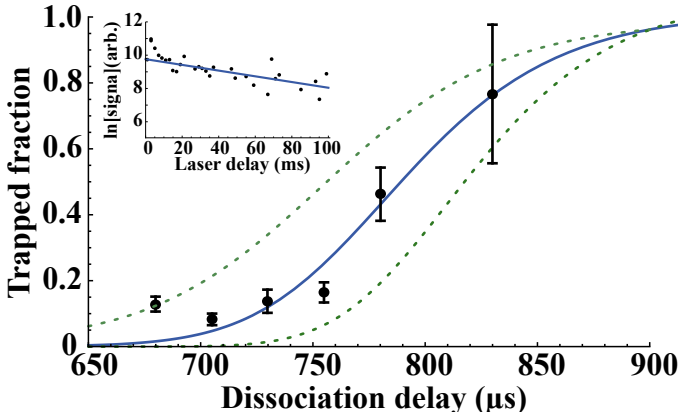

Figure 4.4: Scaled fraction of trapped atoms remaining after the molecular beam pulse, determined by extrapolation of trap loss curves. An example of the extrapolation at a dissociation delay of 780 μs is inset. The solid line is a non-linear fit to a kinetic model. The upper and lower lines show the estimated fraction for half and twice the fitted Ar density, respectively. The figure is drawn from Lam *et al.* [121].

Near the peak of the molecular beam, at a dissociation delay of 780 μs, 60% of initially trapped Br atoms are lost, comparable to that found from Monte-Carlo simulations in section 3.6.

The fractional trap loss during a molecular beam pulse is also modelled as a pseudo first-order process with a time-dependent rate coefficient arising from the time-dependent Ar density, $k(t') = \langle v\sigma \rangle [\mathrm{Ar}](t')$, where t' is a time parameter. The velocity-averaged cross section, $\langle v\sigma \rangle$, is now determined from the DCS for collisions at the 560 m/s molecular beam velocity, integrated over the scattering angle limits determined from the trap depth, as described in section 4.1.

Integrating the rate equation from the dissociation point, t_D, to the end of the

pulse, t_{final} – illustrated by the shaded region in figure 4.3 – yields the fractional trap loss [121]:

$$\frac{[\text{Br}](t_{\text{final}} = 900\,\mu\text{s})}{[\text{Br}](t_{\text{D}})} = \exp\left\{-\int_{t_{\text{D}}}^{t_{\text{final}}} [\text{Ar}](t')\,\langle v\sigma\rangle\,dt'\right\}. \tag{4.3}$$

The time-dependent Ar density is represented analytically by the amplitude-normalised double-sigmoid function, multiplied by the peak density of the molecular beam. The peak Ar density can be calculated by fitting equation 4.3 to the data by least-squares optimisation, and by a scaling factor that accounts for the fraction of Br atoms produced with velocities below the trap depth. The solid line in figure 4.4 demonstrates the fit for a peak Ar density of $(3.0 \pm 0.3) \times 10^{13}\,\text{cm}^{-3}$ [121]; the upper and lower dashed lines indicate the predicted dependence for a density a factor of 2 lower and higher, respectively.

This value is about 30% lower than that predicted from a simple gas dynamics model ($D_{\text{max}} = 3.9 \times 10^{13}\,\text{cm}^{-3}$) [130], described in section 3.2.2. The lower value for the experimental measurement may be due to variations in the operating conditions. For example, the pulsed valve is, at times, found to be slightly tilted, causing a skewed misalignment between the molecular beam axis and the skimmer separating the source and detection chambers. The horizontal position of the valve can be adjusted to maximise the REMPI signal of the Br^+ cations, but the angle between the valve and the skimmer cannot. Thus, the number of Br atoms that effectively pass through the skimmer and through the trap volume, with suitable velocities below the trap depth, will be lower. Alternatively, it may be possible that the poppet in the pulsed valve is not fully retracted, and thus, the effective nozzle diameter would be smaller.

4.3 Future work

The value of the calculated trap depth for the ground spin-orbit state $m_J = 3/2$ sub-state of the Br atom (322 mK) lies between the range of errors for the measured

trap depth ($[215, 325]$ mK). The lower value for the measured trap depth suggests that the some of the detected Br atoms may be in the $m_J = 1/2$ sub-state of the ground, $J = 3/2$, state. Br atoms in this higher sub-state have a lower trap depth ((99 ± 9) mK, as described in section 4.1), and thus, a lower minimum angle for single collisional trap-loss ($\theta_{\min}$). The pseudo first-order rate coefficient, k, described by equation 4.2, and which is dependent on $\theta_{\min}$, would be greater than that calculated for Br atoms purely in the $m_J = 3/2$ sub-state, at the same chamber pressure.

Further work is needed to increase the density of trapped Br atoms. While it would be feasible, in principle, to load the trap continuously rather than in a pulsed format (such as dissociating the parent Br_2 molecule from a continuous beam, by using a sufficiently powerful diode or a continuous-wave dye laser), the loading rate would be limited by collisions between the high-density molecular beam and trapped atoms, as shown in figure 4.4. Furthermore, the background pressure would be much higher, unless very large pumping systems were employed, as demonstrated in figures 4.1 and 4.2. In the pulsed case, the dissociation can be timed to occur near the tail of the molecular beam pulse, minimising such losses, but with fewer Br_2 molecules to photodissociate. Clearly, shortening the molecular beam pulse will enable a reduction in the collisions that contribute to trap loss and thus could facilitate a genuine accumulation of signal over multiple pulses. Such a scheme is described in chapter 5.

Chapter 5 describes a method to reduce collisions with the molecular beam. Additional changes to the design of the chamber, such as with a more effective differential pumping, and to the pumping speed could significantly reduce the base pressure, thus reducing the probability of collisions between the trapped Br atoms and the background gas. A reduction in the number of atoms in the molecular beam due to a shortened beam duration may also increase the likelihood for a lower base pressure to be achieved.

A larger trap depth, such as one created from permanent magnets with a larger

magnetisation, would allow a greater number of Br atoms to be trapped, in particular, those with higher velocities. However the overall temperature of the atoms would be higher under such conditions, and effects involving higher density of trapped atoms, such as from Br–Br collisions, may begin to contribute to trap losses.

Chapter 5

Development of a Molecular Beam Chopper

In this chapter, the design and implementation of a mechanical chopper is described. The effect of the chopper on the duration of the molecular beam, or 'beam width,' and the ability to reduce collisional loss of trapped Br atoms are quantified. The advantages of using a chopper construct in this thesis is discussed in section 5.1. The content in this chapter is drawn from Lam *et al.* [126], as published in the journal *Review of Scientific Instruments*.

5.1 Significance of developing a new method to shorten the duration of cold molecular beams

Recent advances in the production and application of cold atomic and molecular beams benefit from using the shortest gas pulse that is compatible with maintaining a high number density, a narrow velocity distribution, and a cold rotational distribution.

Very short pulsed beams produce fewer gas molecules in the vacuum chamber, thereby lowering the gas load on the pumps for the experimental apparatus, and

reducing background collisions with the beam; the low velocity spread and cold internal temperature of the molecules in the beam are thus preserved [16, 143, 144].

Short-pulse molecular beam sources are primarily pulsed valves that use modified, fast-acting, resonantly-driven valve components. For example, the Jordan Pulsed Supersonic Valve provides cold molecular beams of 55 μs duration during choked flow and 20 μs during low flow [145]. This valve operates on the magnetic beam repulsion principle, by passing opposing currents through two parallel-beam conductors, one of which is a thin metal strip that blocks the gas outlet. The currents produce a magnetic force, which moves the strip and thus opens the valve [146]. Another fast-acting pulsed valve was recently constructed by Janssen and colleagues; it uses a cantilever piezo to produce molecular beam pulses of 7 μs duration at high repetition rates of 5 kHz [147]. The Even-Lavie pulsed valve uses light, miniaturised components to enable operations at high backing pressures of up to 100 bar, resulting in a high intensity molecular beam with a duration of 8 μs and with very cold rotational temperatures for entrained molecules of around 0.5 K [148,149]. Most recently, the Nijmegen Pulsed Valve was constructed, by pulsing a current through an aluminium strip located within a magnetic field. The Lorentz force causes the strip to break its seal to the nozzle in a periodic fashion, resulting in molecular beams with durations as low as 20 μs and a rotational temperature of around 1 K [150].

These beam sources are typically constructed from many small individual components. The high surface area to volume ratio ratio of these components makes them susceptible to corrosion from redox reactions with chemically reactive seed molecules, such as halogen species [151–154]. Thus, the use of a valve that contains a few robust components, while still realising a full expansion of the molecular beam, is advantageous to experiments using reactive seed molecules.

The commercially available General Valve Series 9 valve system has a relatively simple design, and the components are robust against corrosion. The main body is

constructed with corrosion-resistant stainless steel, and a solenoid is used to drive a Teflon cylinder with a conical tip, which breaks the seal to the valve nozzle, producing a fully expanded molecular beam [155]. The Teflon cylinder can be easily replaced, and the build-up of halogen-induced oxidation on the metal components can be easily removed and sanded off without changing the shape of the valve geometry. Thus, the valve is fully compatible with halogen-seeded molecular beams, and residue from the oxidation of the halogen molecules on the valve can be easily washed off with deionised water or acetone. Our current work uses a Series 9 valve to generate a molecular beam of Br_2 seeded in Ar.

A disadvantage of using a Series 9 valve is that the beam pulse duration is typically on the order of a hundreds of microseconds to a few milliseconds, so collisions with a high density of carrier-gas (Ar) atoms in the tail of the pulsed beam (typically 10^{13} cm^{-3} at the centre of the trap) is the dominant cause of trap loss of Br atoms [121]. In order to accumulate density of Br atoms in the trap from successive pulses of the beam, it is essential to minimise trap loss in the 100 ms time interval between the successive photolysis pulses. Thus, the duration of the molecular beam pulses must be reduced, both to minimise collisions with the tail of the beam, and also to reduce the background pressure in the chamber.

A common method of reducing the duration of gas pulses from a valve that initially generates long pulses is to mechanically block the majority of the original gas pulse, and to only open the beam path in a narrow time window. Schwarz *et al.* constructed a molecular beam chopper using an electromagnet to resonantly drive a magnetic field across a contact pin. This oscillating pin blocks and unblocks the molecular beam with the varying density of the beam closely matching that of a sinusoidal function [156]. The use of a spinning chopper wheel has been a more common tool, particularly in experiments which observe the time resolved dynamics of reactions in a molecular beam. By only letting a small portion of the beam pass through the slit of a spinning

chopper wheel, a full TOF profile, and therefore velocity distribution of the source beam, can be found [155, 157–162]. The molecular beam is directed perpendicularly to a spinning disk, into which slots are cut. The rotation of the disk is synchronised to the gas pulse, so that only a portion is allowed through the slot, and the rest of the beam is blocked. Abad *et al.* measured the velocity distributions and translational temperatures of the molecular beam from a Series 9 valve using a chopper rotating at 11,280 rpm to produce molecular beam durations of around 23 μs [155].

However, two disadvantages of using a chopper wheel to shorten molecular beams have prevented this method from dominating over modified pulsed valves. First, the relatively low mechanical speed of rotation used to date limits the shortest gas pulse attainable. Second, the large portion of the molecular beam that does not pass through the chopper slit may contribute to the background pressure in the vacuum chamber. Increasing the disk radius of the chopper increases the tangential velocity, and hence, reduces the pulse width for a given slot dimension. But a larger disk also increases the mechanical and heat load on the system, and the radius is typically limited by the geometry of the vacuum chamber and the ability to balance the disk onto the motor at high revolution speeds. The gas build-up has been mitigated by placing the chopper wheel along the path of a set of skimmed differentially pumped stages [163].

5.2 Constraints for the design of the chopper construct

The construction of a mechanical chopper to shorten the duration of a molecular beam is dependent on many experimental factors, such as the velocity distribution of the Ar carrier gas in the molecular beam, the distance from the valve to the chopper wheel, and the dimensions of the source chamber. The design of the chopper construct

described in this thesis is specific to accommodate the experimental set-up described in Chapter 2.

5.2.1 Analytical model of pulse width reduction by the chopper

The terminal velocity of a molecular beam, v_∞, is given by [16]

$$v_\infty = \sqrt{\frac{\bar{\gamma}}{\bar{\gamma}-1}\frac{2k_\mathrm{B}T}{m_\mathrm{eff}}}, \tag{5.1}$$

where $\bar{\gamma}$ is the mean heat capacity ratio of the mixture (calculated to be 1.67 for a weighted average of 8% Br_2 in Ar, and to be 1.63 for 8% NO in Ar), k_B is the Boltzmann constant, T is the initial temperature of the gas in the reservoir (298 K), and m_eff is the weighted average mass of the mixture [16]. The standard deviation of velocities around v_∞ in the moving frame is related to the translational temperature of Ar in the moving frame, T_Ar [126]:

$$\sigma_\mathrm{v} = \sqrt{\frac{2k_\mathrm{B}T_\mathrm{Ar}}{m_\mathrm{Ar}}}, \tag{5.2}$$

The packet of molecules that passes through the chopper has a length ω_0 (immediately after the chopper wheel) that is inversely proportional to the rotational frequency of the wheel, given by

$$w_0 = v_\infty\frac{d_\mathrm{slit}}{2\pi rS}, \tag{5.3}$$

where d_slit is the width of the slit tangential to the edge of the chopper (equal to 1 mm), r is the radius of the chopper wheel, and S is the rotational frequency of the chopper in revolutions per second [126]. The moving-frame temperature causes longitudinal expansion of the packet during the flight from the chopper to the detection region,

with the spatial spreading given by

$$w_\sigma = \sigma_{\mathrm{v}} t = \sigma_{\mathrm{v}} \frac{d_{\mathrm{ci}}}{v_\infty}, \tag{5.4}$$

where d_{ci} is the distance between the chopper and intersection with the detection laser, and t is the mean time taken for the packet to travel that distance [126]. Using equations (5.3) and (5.4), the length of the detected packet at the laser detection volume, w_{beam}, is obtained from the convolution of the length of the initially chopped packet with that due to its longitudinal velocity distribution σ_{v}. A Gaussian packet and velocity distribution is assumed to give

$$w_{\mathrm{beam}}^2 = w_0^2 + w_\sigma^2 = (v_\infty \frac{d_{\mathrm{slit}}}{2\pi r S})^2 + (\sigma_{\mathrm{v}} \frac{d_{\mathrm{ci}}}{v_\infty})^2. \tag{5.5}$$

At low rotational frequency of the chopper, the size of the molecular beam is determined by the first term in equation 5.5, while at high frequency, by the spread of velocities around the moving frame, v_{s}, as indicated by the second term [126].

5.2.2 Physical constraints

Two primary characteristics of the chopper construct which limit the beam width are the following. First, the diameter of the chopper is constrained by the diameter of a stainless steel 'top hat,' located at the end of the source chamber, shown in figure 5.3. The experimental set-up is described in more detail in section 5.4. Second, the revolution speed of the chopper wheel is limited by the maximum motor speed appropriate to use safely, as described in more detail in section 5.3.

Figure 5.1 shows the smallest beam widths that can be achieved in an ideal situation, where the chopper slit is located right next to the detection region.

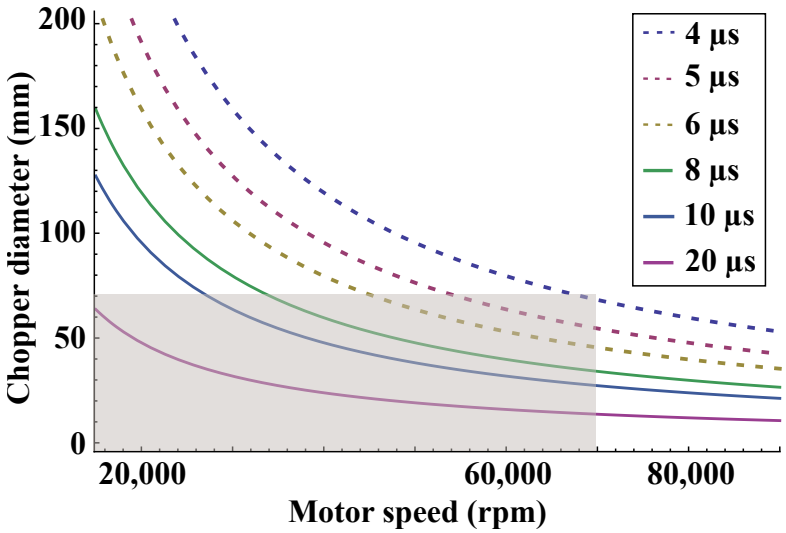

Figure 5.1: Range of beam widths achieved with the detection region located right after the molecular beam passes through the chopper slit. This range (shaded area) is bound by the diameter of the chopper and just below the maximum motor speed of the chopper.

The beam width is also a function of the diameter of the chopper wheel, shown on the y-axis in figure 5.1. As this diameter increases, the tangential velocity of the edge of the chopper wheel increases, and correspondingly, the period of time at which the molecular beam passes through the chopper slit, decreases, respectively. The shaded grey area shows the upper limit of the diameter of the chopper wheel, constrained by the dimensions of the source chamber, and by a conservative estimate of the highest motor revolution speed of 70,000 rpm, just under the maximum revolution speed. Under these conditions, and assuming that the detection region is located immediately after the chopper wheel, a beam width of 5 μs could, in principle, be achieved at a chopper speed of around 60,000 rpm.

5.3 Final design of the chopper construct

The chopper disk is a 70 mm diameter aluminium (7075 Aircraft alloy) disk with two slits cut on opposite sides. The slits are 1 mm wide and extend 3 mm into the

disk centre (described later in section 5.4 in figure 5.4). The disk is thinned at the edge to less than 1 mm. The chopper wheel is directly coupled onto the shaft of a 25 mm diameter brushless DC motor (Maxon Motor model EC25), balanced at up to 42,000 rpm in ambient conditions.

This brushless DC motor is chosen for its durability, which allows for the high speed of the chopper. First, it is compatible with a vacuum environment, due to it having fewer components than other types of motors. Second, the motor has a high torque output per power input due to the low friction around its bearings. Third, it has low electromagnetic interference. Fourth, it has an ability to operate without requiring the use of additional cooling agents such as airflow or water [164–166]. Finally, the motor uses ball bearings which are vacuum compatible and which minimises the build-up of heat around the rotor.

Two chopper slits are used to ensure that at most one slit will pass through the molecular beam over the largest range of motor speeds, while keeping the chopper wheel balanced. With just one slit, for example, the chopper wheel will be off-balance when spinning, which may decrease the precision of synchronisation with the chopper system and increase the turbulence behind the chopper wheel. The period between each slit over this range is presented in figure 5.2.

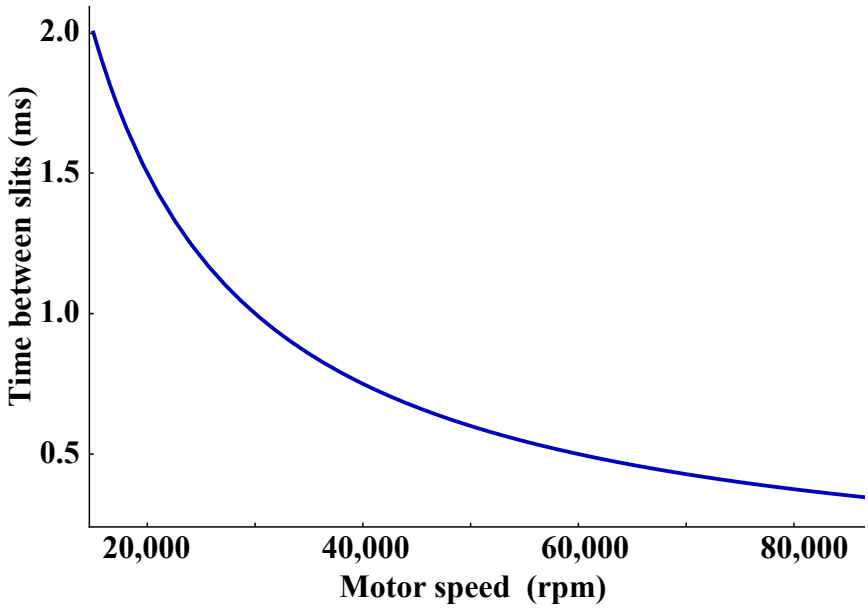

Figure 5.2: The calculated time between each slit passing through the axis of the molecular beam, as a function of motor speed.

The duration of the un-chopped molecular beam is about 350 μs, as shown in figure 4.4. If the front end of the molecular beam were to pass through the first chopper slit, then in order to block the rest of the beam, and thus, in order to prevent the tail of the beam from passing through the second slit, the chopper motor speed would need to remain below about 65,000 rpm. However, the peak of the molecular beam produces the largest amount of signal of Br, as well as trapped Br signal; synchronising the centre of the slit with the centre of the molecular beam pulse results in blockage of the remainder of the pulse. Thus, the tail of the molecular beam pulse will not overlap with the second slit, up to a maximum chopper motor speed of 80,000 rpm.

5.4 Implementing the chopper construct into the source chamber

A schematic of the chopper device located within the experimental apparatus, adapted from figure 2.3, is shown in figure 5.3. The pulsed valve generates a molecular beam,

which passes through two skimmers separated by the chopper wheel and ultimately passes into the differentially-pumped detection chamber. The chopper, its motor, and the pulsed valve are housed within the 'top hat.' The source chamber is pumped by a 700 L/s diffusion pump, while the detection chamber is pumped by a 350 L/s turbo-molecular pump. As shown in figure 5.3, the chopper wheel is placed between skimmer-A and skimmer-B, with the slitted edge aligned with the centre of the molecular beam.

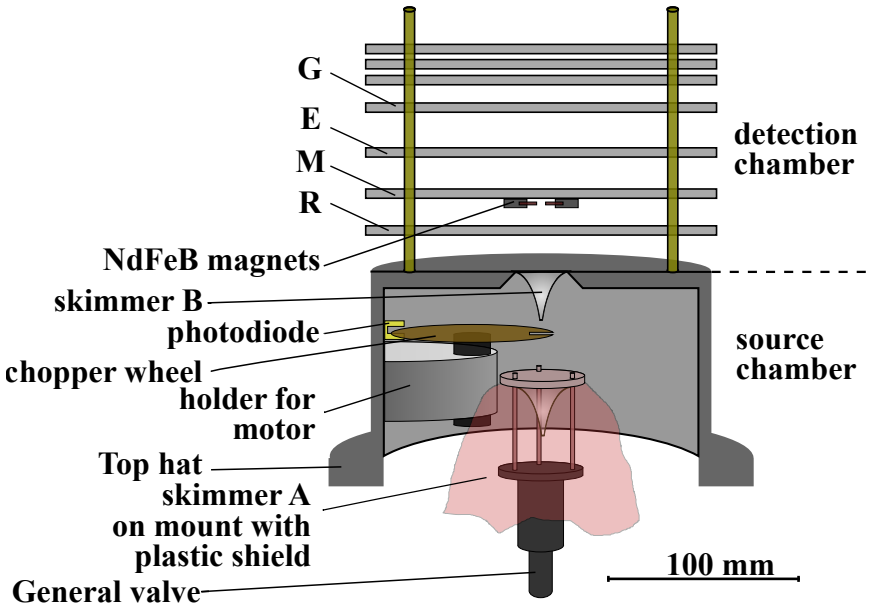

Figure 5.3: Molecular beam and ion detection section of the experimental set-up. The Br^+ ionised by REMPI passes through a series of electrostatic plates, labeled G (ground), E (extractor), M (magnet), and R (repeller), designed for TOF detection of ions. The dotted line (right) shows the separation between the source chamber (bottom) and the detection chamber (top). The figure is drawn from Lam *et al.* [126].

The chopper is driven by a home-built controller which generates the AC wave forms used to drive the brushless motor at the desired speed, tunable from 3,000 rpm to 80,000 rpm. The motor is cooled by contact with the wall of the vacuum chamber, and remains below 80 °C at speeds up to 80,000 rpm.

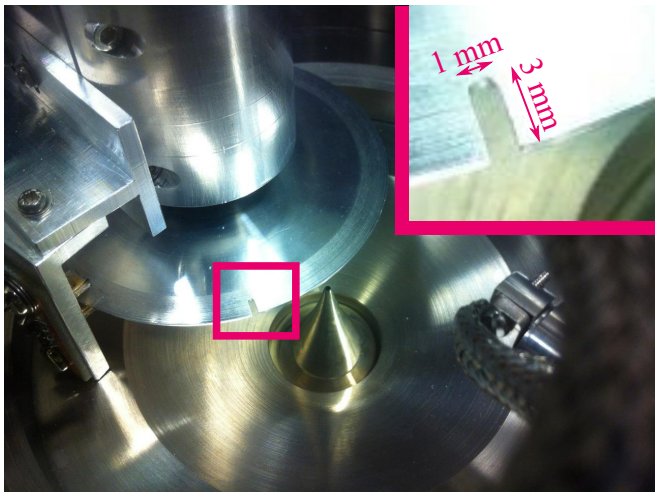

Figure 5.4: Photograph of the chopper set-up in the source chamber. The chopper slit is seen as the indent in the chopper wheel (enclose by the pink square). A close-up of this slit is shown (inset), with dimensions as indicated. The figure is drawn from Lam *et al.* [126].

Skimmer-A (orifice diameter 1 mm) is rigidly mounted to the Series 9 valve, as shown in figure 5.3. This rigid mounting mechanically aligns skimmer-A to the valve orifice, at a distance of 3 cm from the skimmer tip. The mount is surrounded by a shroud made of plastic polyethylene terephthalate (PET) foil, which forms an effective differential pumping stage. This set-up enables only the central part (1 mm diameter) of the molecular beam, passing through the first skimmer, to reach the chopper wheel. The rest of the beam, travelling off-axis, is directed by the PET foil to the diffusion pump, which has a pumping speed sufficient to allow the background gas to be pumped away before further build-up from the next gas pulse. Any gas escaping around the edge of the shroud has a long enough diffusion time that it does not interfere with the fast on-axis beam. The molecular beam pulse, shortened by the chopper wheel, subsequently passes through a 0.5 mm skimmer (B), which blocks further background gas scattered by the chopper wheel from reaching the detection chamber.

The chopper generates a trigger pulse used to trigger the pulsed valve and the REMPI laser. As the edge of one of the two chopper slits passes between the pho-

todiode (shown in figure 5.3) and a LED light, a trigger pulse is passed back to the chopper controller through a pair of vacuum feedthroughs (Allectra GmbH). This trigger pulse train is corrected to a 10 μs-wide pulse, independent of rotation frequency, and a gate allows only the first pulse in every 100 ms through to the output. This output is therefore synchronised to the chopper, nominally at the 10 Hz frequency demanded by the pulsed laser system. The actual frequency is allowed to vary between 9.5 Hz and 10.5 Hz to maintain the phase-lock, with negligible impact on the laser power. This pulse triggers the input of a delay generator (Quantum Composer 9500 Plus Series), which in turn triggers the pulsed valve after a delay (A) and the REMPI lasers after a further delay (B), as shown in figure 5.5.

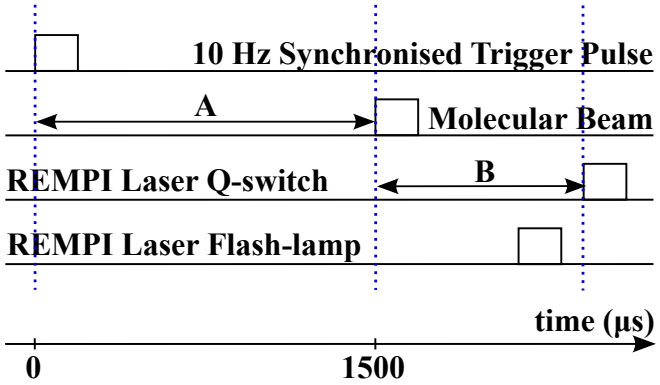

Figure 5.5: Diagram of the timing set-up in the chopper controller and delay generator. **A** is the time between the 10 Hz clock signal generated by the chopper and the trigger for the pulsed valve actuation, and **B** is the delay between the pulsed valve and the dissociation/REMPI laser Q-switch triggers. The widths of the delay generator output pulses are on the order of 1 μs. The figure is drawn from Lam *et al.* [126].

5.5 Testing with NO as the seed molecule

5.5.1 Controlling the temperature of the molecular beam

The chopper construct is tested with a molecular beam composed of 8-10% NO seeded in 3 bar of Ar. NO is chosen due to its strong, well-resolved, rotational lines in the (1+1) REMPI spectrum, facilitating easy calibration of the rotational temperature

of the molecular beam, and due to the convenient wavelength of the REMPI laser in the set-up. A photodissociation laser is not used for these experiments. The NO is detected by (1+1) REMPI via the $A^2\Sigma^+ \leftarrow X^2\Pi_{1/2,3/2}$ transition at a wavelength around 226.2 nm (corresponding to the position of the overlapping Q_{21} (0.5) R_{11}(0.5) lines) [167, 168]. The fundamental wavelength is generated from a pulsed dye laser (Sirah Continuum, Coumarin 503 dye) and doubled with a BBO crystal. The NO^+ cations, produced by REMPI close to plate M, are guided towards the MCP detector (absent from figure 5.3) by the field applied across plates R, M and E, using a Wiley-McLaren configuration (see figure 5.3) [169].

The rotational temperature of NO in the molecular beam is determined by recording the REMPI signal of NO while scanning the detection wavelength from 226.000 nm to 226.400 nm. The rotational line intensities are fitted to a Boltzmann plot, as well as a full simulation of the spectrum using the simulation program PGOPHER [170, 171].

The Boltzmann plot is an efficient tool in finding the rotational temperature of gases, by fitting peak intensities of the rotational lines of the gas logarithmically against transition energy. This method is described by equation 5.6,

$$\ln\left(\frac{I_{J'\leftarrow J''}}{S_{J'\leftarrow J''}}\right) = -\frac{1}{T} \times \frac{E_{J''}}{k_{\mathrm{B}}} + \ln(\Omega), \tag{5.6}$$

where $I_{J'\leftarrow J''}$ is the measured intensity of each isolated rotational absorption line, its value calculated by fitting the area under each intensity peak to a Gaussian function and integrating across the full line profile, $J' \leftarrow J''$ is the transition from the lower state (J'') to the higher state (J'), $S_{J'\leftarrow J''}$ is the absorption line strength (Hönl-London factor) also computed from the simulation PGOPHER, T is the rotational temperature of the NO in the molecular beam, Ω is the partition function that normalises the population distribution in each energy state, J, and $E_{J''}$ is the energy of the rotational level in the lower state.

As described in section 2.1, the gas pressure is measured indirectly and, in this case, varies from 3 $\times 10^{-5}$ mbar to 5 $\times 10^{-6}$ mbar. The chopper construct is absent to enable a greater amount of molecules to reach the detection volume. Two sets of measurements are performed, one set with skimmer-A attached to the Series 9 valve but without the chopper construct, and another set with neither skimmer-A or the chopper construct present. Figure 5.6 shows one such Boltzmann plot, with a gas pressure of 1 $\times 10^{-5}$ mbar, with skimmer-A attached to the Series 9 valve and without the chopper construct.

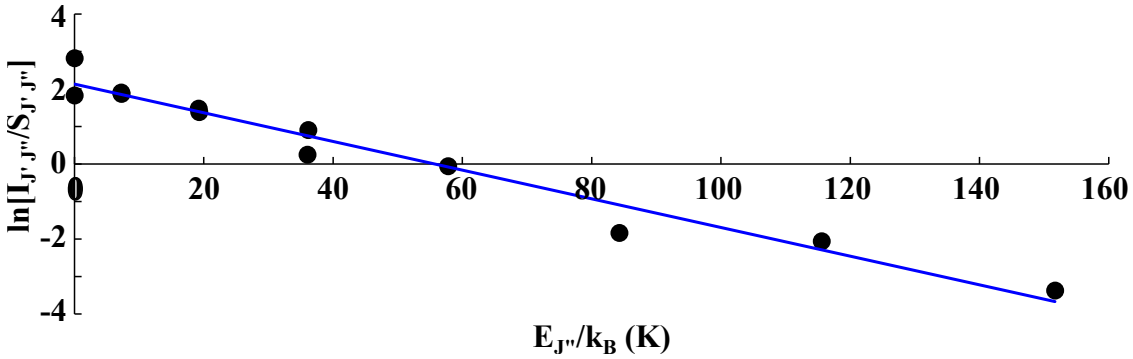

Figure 5.6: Intensities of the rotational absorption lines of NO at a gas pressure of 1 $\times 10^{-5}$ mbar (black), using the Boltzmann plot method in equation 5.6. A regression line (blue) is fitted for the rotational temperature of the NO. All transition energies (x-axis) are relative. Both skimmers A and B are used, with no chopper in place.

A least-squares fit through the data points (blue) determines the rotational temperature of the NO, equal to $-1/S_{\text{fit}}$, where S_{fit} is the slope of the regression line. In figure 5.6, the rotational temperature is calculated to be (26.2 $\pm$ 0.2) K, where the error is the standard error derived from the corresponding regression line for small sample sizes.

Rotational temperatures are shown in figure 5.7, plotted as a function of source chamber pressure, in the two cases with (blue) and without (red) skimmer-A attached to the Series 9 valve.

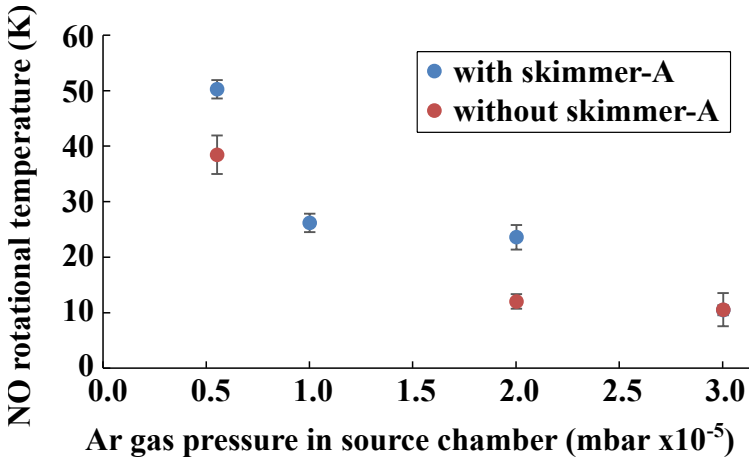

Figure 5.7: Rotational temperatures of NO as a function of gas pressure. Each data point is fitted using equation 5.6 in a Boltzmann plot.

In both cases, with and without skimmer-A, the rotational temperature of NO decreases from around 40 K to 10 K as the gas flow from the valve increases, from gas pressures of 5×10^{-6} mbar to 3×10^{-5} mbar, respectively. The calculated temperatures in figures 5.6 and 5.7 are independently verified using the spectral simulations in PGOPHER. The measured REMPI spectrum used for the Boltzmann plot in figure 5.6 (top, red) is compared with a PGOPHER simulation (bottom, black), shown in figure 5.8.

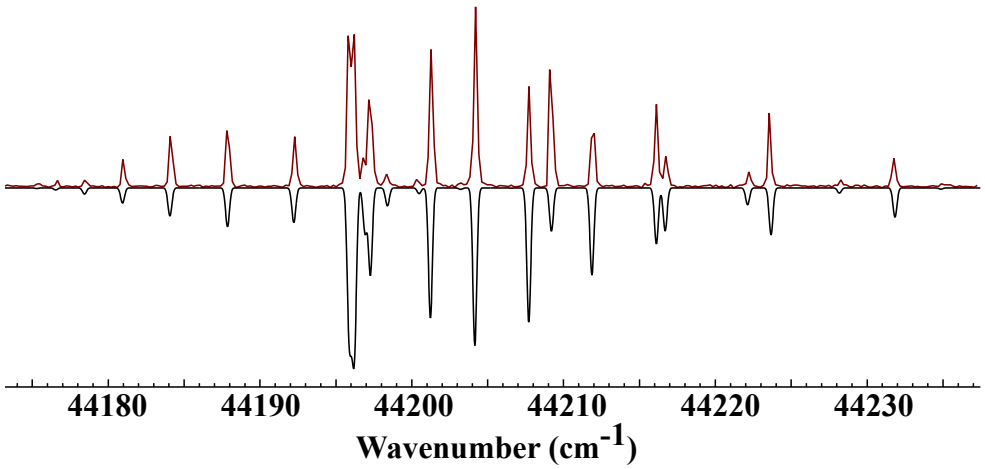

Figure 5.8: The NO (1+1) REMPI spectrum recorded experimentally (above) and simulated (below) with PGOPHER, at rotational temperatures of 26.2 K and 24 K, respectively.

The relative intensities of the absorption lines in both plots are in near-qualitative agreement. The simulated spectrum in PGOPHER (at a rotational temperature of 24 K) appears to have the best fit to the REMPI spectrum (at 26.2 K, as calculated from the Boltzmann plot in figure 5.6). The fit is limited by variations in the relative intensities between the measured and simulated spectra. The first disappearance of an absorption line (Q_{21} line ($\nu = 0, J = 7.5 \leftarrow \nu = 0, J = 7.5$) at 44235 cm^{-1}) occurs at a rotational temperature of 24.6 K, and the first appearance of an additional line (P_1 line ($\nu = 0, J = 7.5 \leftarrow \nu = 0, J = 8.5$) at 44175 cm^{-1}) occurs at 25.1 K.

The low rotational temperature of NO passing through the chopper indicates that there is little or no build-up of background gas behind the chopper wheel (which, if present, interferes with the molecular beam passing through it).

The NO result confirms the feasibility of the effective differential pumping stage using the PET foil. Figure 5.9 shows the NO signal recorded with the REMPI laser, fixed at a wavelength of 226.2 nm and taken with a chopper speed of 3,000 rpm, with and without this plastic shield. The delay between the synchronised clock signal from the chopper and the REMPI laser is scanned to record the temporal profile of the beam passing through.

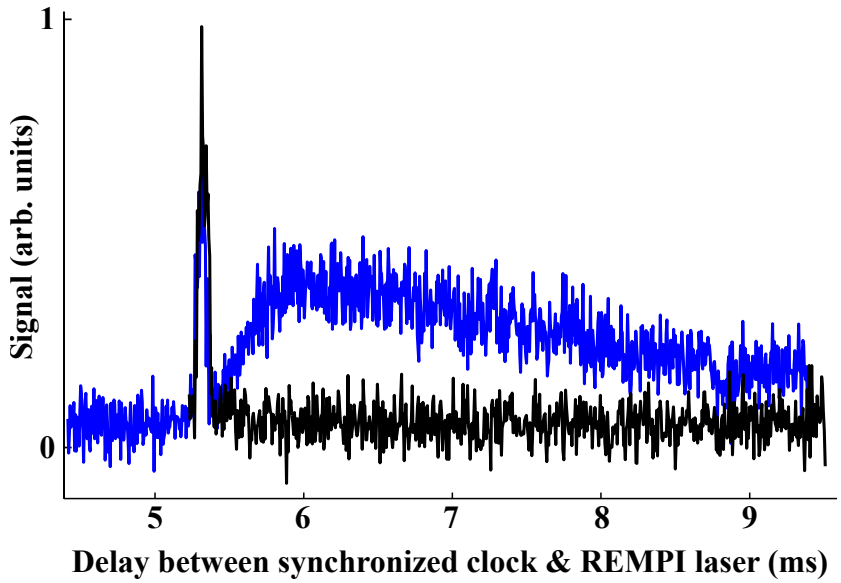

Figure 5.9: Comparison of the NO signal measured on the MCPs with a chopper running at a revolution speed of 3,000 rpm, with (black) and without (blue) the plastic shield. The figure is drawn from Lam *et al.* [126].

In both cases, a clear, sharp NO peak at a 5.3 ms delay indicates that a molecular beam pulse of the same duration passes through the chopper wheel, as shown in figure 5.9. However, in the case without using the PET foil, a broad signal of NO is observed at longer time delays. The broad signal results from gas that does not pass through the first skimmer, but rather slowly diffuses to the detection region. The broad signal is eliminated when using the PET foil; the foil acts as a differential pumping stage, and therefore allows observation of a clean, sharp peak in the TOF. This qualitative comparison is repeated at five different revolution speeds of the chopper wheel (3,000 rpm to 50,000 rpm); all chopper speeds show similar results.

5.5.2 Controlling the duration of the molecular beam

For a range of revolution speeds, the temporal profile of the NO REMPI signal is recorded with delay **A** set to a constant optimised value of 750 μs near the peak of the molecular beam. This value allows the largest gas density from the molecular

beam packet to reach the chopper slit, as shown in figure 5.10 at a chopper speed of 70,000 rpm.

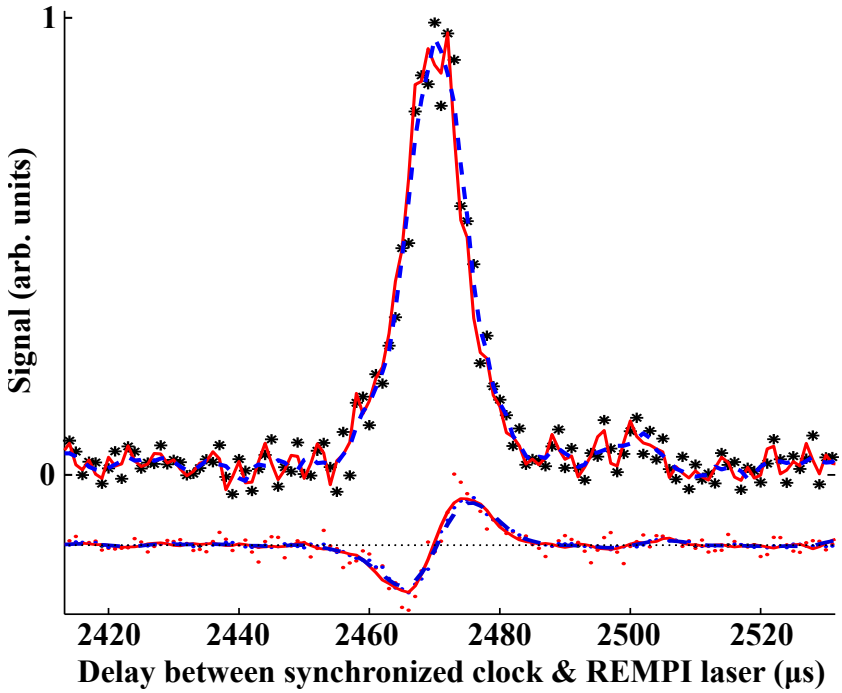

Figure 5.10: A normalised profile of the molecular beam with the chopper running at 70,000 rpm. The upper trace (black stars) shows the signal intensity, and the lower (red dots) shows the negative of its first derivative (used to define the pulse duration). The Savitzky-Golay method uses fine and rough fits (solid-red and dashed-blue lines, respectively) to determine the beam width of this profile. The figure is drawn from Lam *et al.* [126].

A Savitzky-Golay method is used to smooth the raw data (black stars) [172, 173]. This method applies a 2nd order polynomial least-square fit to the data set, as shown in figure 5.10, where the solid-red and dashed-blue lines in the fit above the $(y = 0)$-axis indicate fine and rough fits, respectively, according to the number of data points used in the smoothing algorithm (4 and 9 points, respectively). Next, the first derivative is taken from these curves, and the Savitzky-Golay method is applied again, as shown by the curves located below the zero $(y = 0)$-axis in figure 5.10. The beam width is defined as the difference between the delays on the x-axis, representing the peak and nadir of this final, smoothed, first derivative. The beam width for the profile in figure

5.10 is calculated to be 8 μs and 11 μs, from the fine and rough fits, respectively.

A series of these beam widths are determined for NO over a range of revolution speeds of the chopper wheel, from 3,000 rpm to 79,800 rpm, and the values are plotted as the orange points in figure 5.11.

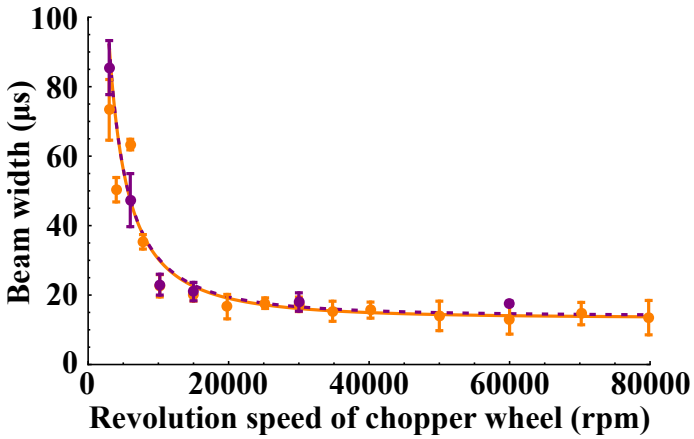

Figure 5.11: Plot of beam widths of NO (orange) and Br (purple) as a function of chopper speed. Each data point represents an average and first standard deviation of three sets of beam-width measurements. The theoretical model, w_{beam}, described by equation 5.5, is represented by the solid-orange and dashed-purple curves for NO and Br_2, respectively. The figure is drawn from Lam *et al.* [126].

Each data point in figure 5.11 represents an average of three beam-profile measurements, each fitted using a rough fit (dashed-blue line, in figure 5.10) to provide an upper limit to the calculated beam widths. The error bars show the one standard deviation variation of this fluctuation over repeated runs. Thus the average 13 μs beam width for a revolution speed of 80,000 rpm is greater than some of the individually measured beam widths, such as that shown in figure 5.10 (which is calculated to be 11 μs using a rough fit, or 8 μs using a finer fit, for a revolution speed of 70,000 rpm).

The theoretical model value of w_{beam}, defined by equation 5.5, is used to calculate the expected temporal width of the pulse and is plotted for a NO seeded beam (solid orange line) in the figure. In both the experimental measurements and theoretical model, beam widths at revolution speeds beyond 30,000 rpm converge toward a single value on the order of 10 μs, limited by the longitudinal velocity distribution, σ_{v}, of the

molecular beam. Excellent agreement is observed between theory and experiment.

5.6 Testing with Br_2 as the seed molecule

To confirm that the results from the chopper are consistent for other seed molecules, particularly with corrosive halogen species - a key objective of this work - measurements are also performed with a molecular beam of 8-10% Br_2 seeded in Ar, at a backing pressure of 3 bar. The Br_2 molecules passing through the chopper and skimmers are photodissociated, and the Br atoms are detected by (2+1) REMPI detection, as described in section 2.1.

As shown in figure 5.12, without the use of a chopper (black line), the Br_2 molecular beam has a FWHM (dashed lines) duration of 130 μs, whereas with a chopper running at 60,000 rpm (blue), just under the maximum speed of 80,000 rpm, the duration of the beam is reduced to 18 μs.

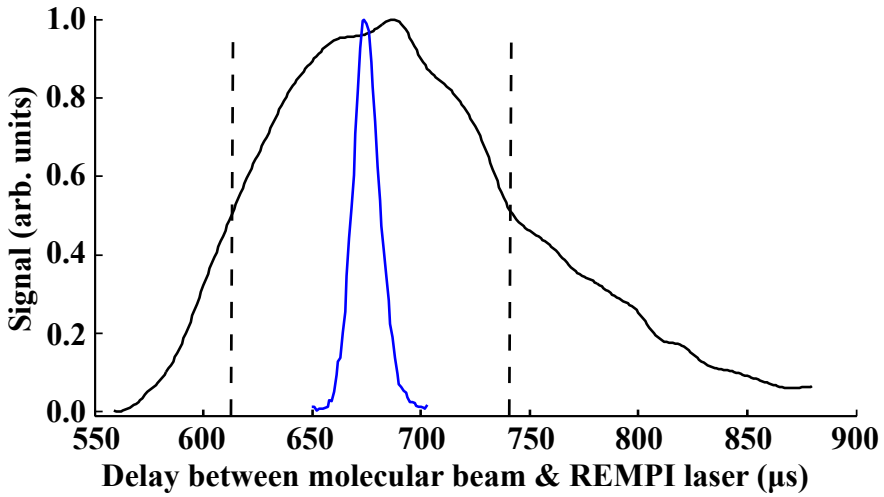

Figure 5.12: Molecular beam profile of 8-10% Br_2 seeded in 3 bar Ar without the presence of a chopper (black) and with a chopper running at 60,000 rpm (blue). The dotted lines show boundaries of the FWHM of the molecular beam profile without the chopper. The figure is drawn from Lam *et al.* [126].

In figure 5.12, the molecular beam profile has been smoothed using a Savitzky-Golay algorithm. Note that although the intensities of each signal are shown as having the

same peak value, the relative normalisation is only approximate. The removal or re-installation of the chopper requires substantial changes to the set-up. Therefore, it is difficult to ensure that there is no residual dependence of the signal intensity on the power and on the alignment of the dissociation and REMPI lasers in the two sets of measurements. In practice, such measurements are separated by days. Nevertheless, it is clear that there is substantial shortening of the molecular beam pulse with the chopper in place. In figure 5.11, the measured (dots) and calculated (dashed lines) pulse widths for the Br_2 molecular beam are plotted in purple; these are seen to fit on the same line as the data for NO, verifying the general applicability of this analytical model.

The molecular beam profile also varies with the revolution speed of the chopper. In figure 5.13, the molecular beam profile with a chopper running at 60,000 rpm (blue) is thin and narrow. This peak widens and flattens with decreasing chopper speed, as illustrated by the profile passing through a chopper running at 3,000 rpm (black). This is because with lower revolution speeds, the chopper slit passes through the molecular beam axis at a slower rate, and thus, the molecular beam will be admitted through the slit for a longer period of time.

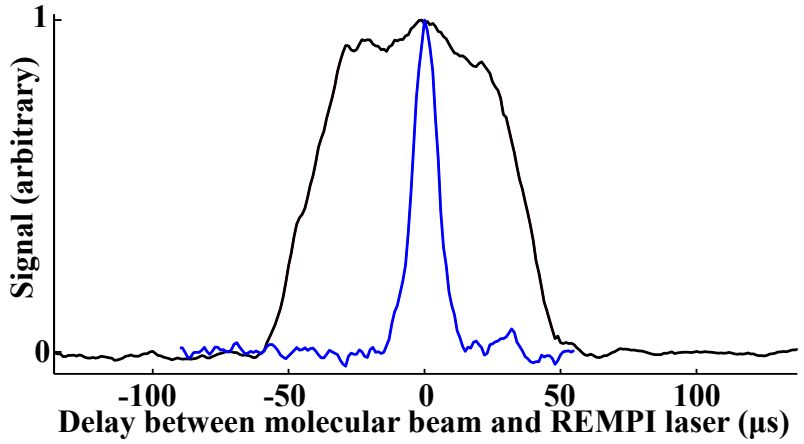

Figure 5.13: Comparison of the molecular beam profile with a chopper running at 60,000 rpm (blue) and at 3,000 rpm (black) [126]. The peak intensity of the profile with a chopper running at 60,000 rpm has been scaled to that with the chopper at 3,000 rpm for clarity.

In addition to measuring the signal of Br over one pulse, the stability of the period between each chopper slit is also tested over a range of a few milliseconds. Figure 5.14 illustrates the periodic signal of Br atoms at chopper speeds of 4,000 rpm (orange) and 6,000 rpm (blue). For each molecular beam pulse, only one section of the molecular beam passes through the chopper slit. The regions where no Br signal is present indicate the times when the molecular beam is blocked by the chopper wheel.

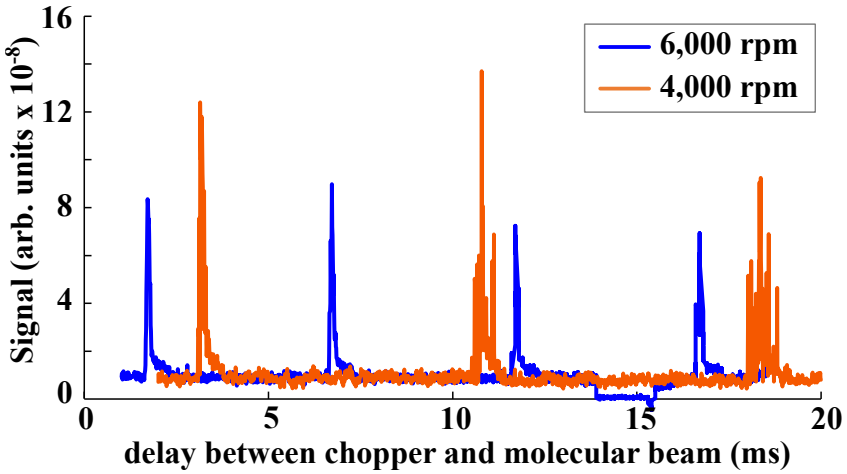

Figure 5.14: Signal of Br^+ over multiple molecular beam cycles, with a chopper running at 4,000 rpm (red) and at 6,000 rpm (blue).

The average period between each slit for a chopper running at 6,000 rpm is (5.0 ± 0.1) ms, in figure 5.14, which is within 1 standard deviation from the theoretical value of 5.0 ms in figure 5.2. The time period for a chopper running at 4,000 rpm is measured to be (7.6 ± 0.1) ms, which is 2 standard deviations from the theoretical value of 7.5 ms in figure 5.2. In the second case, the agreement between experiment and theory is less quantitative, attributed to the fewer peaks over the same time period (due to the slower rate at which the chopper slit passes through the molecular beam axis).

5.7 Controlling trap loss of Br atoms by minimising collisions with the molecular beam

5.7.1 Decay of Br atoms with a chopped molecular beam

To analyse the effects of molecular beam collisions on the initially trapped Br atoms prepared using a chopper construct, one can observe the decay of Br signal over a range of laser delays for different chopper rotational speeds (and hence different pulse lengths). Figure 5.15 shows the Br atom signal measured at laser delays from 0 ms to 6 ms, with a chopper running at 3,000 rpm and 6,000 rpm (blue and orange dots, respectively), corresponding to beam widths of 87 μs and 55 μs (shown in figure 5.11), respectively. Each data point at a chopper speed of 3,000 rpm is an average of three measurements, with an error bar representing the standard deviation of related experiments, $0.434 \times [\mathrm{Br}]_{\mathbf{err,\ avg}}/[\mathrm{Br}]_{\mathrm{avg}}$, as described in section 2.5. The data points measured at a chopper speed of 6,000 rpm each indicate just one measurement (with the error bar representing the total error in signal intensity, $[\mathrm{Br}]_{\mathbf{err}}$, described in section 2.5). The intensity of the Br signal is much lower and more difficult to measure with the chopper running at 6,000 rpm; the drop in intensity at this chopper speed is

quantified in more detail at the end of this section. Further measurements are required to improve the accuracy and precision of this data. For comparison, the Br decays from figure 2.6 are replotted here, without a chopper (red stars) and further without magnets (black stars).

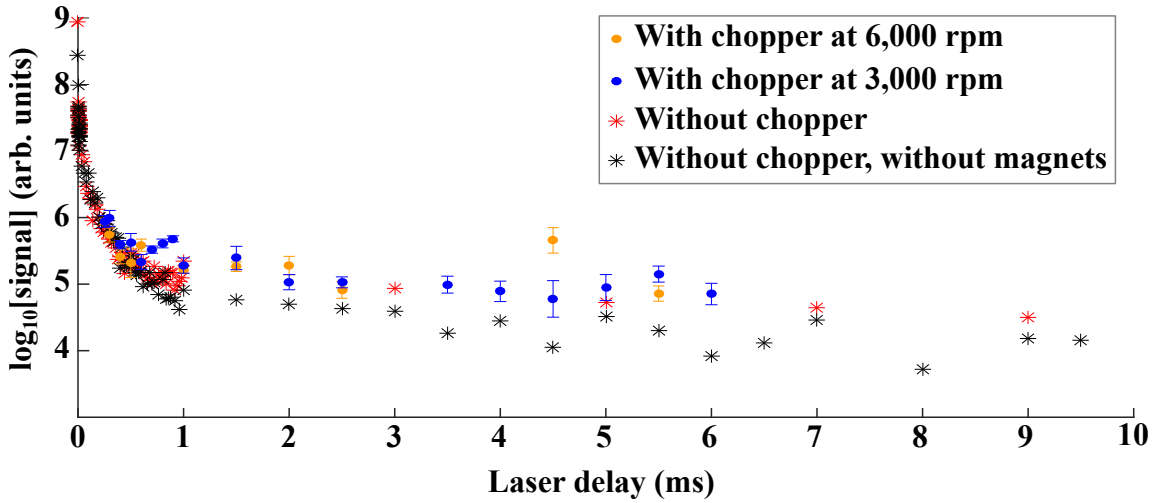

Figure 5.15: Fraction of initially trapped Br atoms remaining after collisions with the molecular beam, determined by extrapolation of the trap loss curve in equation 4.3. The amount of Br atoms with a chopper running at 3,000 and at 6,000 rpm are illustrated by the blue and orange dots, respectively). The red (with magnets) and black (with Al pieces) stars are drawn from Rennick *et al.* [122].

.

The Br decays with a chopper are normalised to the data in figure 2.6 (red and black stars in figure 5.15) at a laser delay of 250 μs. This normalisation value is chosen for the following reasons. Below 250 μs, the Br signal measured is primarily composed of fast atoms undergoing ballistic expansion out of the detection volume; the Br decays in all plots from 0 to 250 μs thus follow the same trend. Beyond this, the shapes of the decay for the cases with and without the chopper begin to differ. As illustrated in figure 2.6, the Br decays transition smoothly from being dominated by ballistic expansion, to being dominated by collisions with Ar in the molecular beam, and finally, with Ar in the thermal background. In contrast, for the Br decays with a chopper running at 3,000 and 6,000 rpm, this transition is sharp, from being

dominated by ballistic expansion, directly to being dominated by collisions with Ar in the thermal background. Collisions with the molecular beam are hidden in the Br decays with the chopper, because the duration of molecular beam collisions is smaller than that of ballistic expansion. This transition is hard to simulate and quantify, and further work is required to move beyond this qualitative analysis.

Following the normalisation procedure described in the preceding paragraph, the relative fraction of initially trapped Br atoms appears to be greater at laser delays beyond 250 μs with a chopper present, especially for the data at 3,000 rpm (blue dots). However, this observation is not fully conclusive, as both sets of trapped Br signal in the presence of a chopper lie within the error bars of the older data from figure 2.6. Furthermore, it is hard to tell the difference in relative signal intensity between the two sets of decays (with chopper speeds of 3,000 and 6,000 rpm), particularly because the Br signal is close to the detection limit and therefore very hard to extract. Repeated measurements of the Br decays with the chopper running at 3,000 and 6,000 rpm will be needed to quantify the increase in relative fraction of Br signal at long laser delays in the presence of a chopper.

The initial amount of Br atoms formed with the chopper present is lower by a factor of 40, compared to the un-chopped beam when the chopper runs at 3000 rpm, and by a factor of 160 at 6000 rpm. This is likely to be because the chopper wheel blocks a majority of the molecular beam that contains Br_2 molecules with the right velocity to produce photostopped Br atoms There is a strong correlation between the longitudinal velocity of a Br_2 molecule and its arrival time at the laser probe volume; molecules moving faster than the average speed of the molecular beam arrive earlier, and those moving slower arrive later. At the detection volume, the faster moving molecules located at the back of the molecular beam can catch up with the slower moving ones located at the front of the molecular beam. In the presence of a spinning chopper wheel, these molecules are blocked by the chopper wheel before they reach the

detection volume. Moving the pulsed valve closer to the chopper construct can reduce this loss in peak density, although the current experimental geometry is not favourable to this suggestion. Thus, ironically, while the use of a chopper construct minimises trap loss, it also substantially decreases the absolute amount of atoms initially formed. The ideal situation for producing a source of cold Br atoms is to obtain the highest absolute number of Br atoms in the trap at laser delays beyond 99 ms, long enough for the atoms to accumulate over successive molecular beam cycles. The next section illustrates the feasibility of obtaining sufficient density of Br atoms with a chopper running at 3,000 rpm.

5.7.2 Collisional loss of trapped Br atoms with a chopped molecular beam

The collision dynamics between trapped Br atoms and the molecular beam have been tested with the chopper in place. Figure 5.16 shows the percentage of initially trapped Br atoms which remain trapped after collisions with the molecular beam at different delays between the pulsed valve and the dissociation laser, passing through a chopper running at 3,000 rpm. (This method is similar to the process described in section 4.2). The measurements taken for figures 5.15 and 5.16 are performed with a source chamber pressure of 2×10^{-5} mbar, in order to be consistent with the measurements taken without the chopper construct in section 4.2.

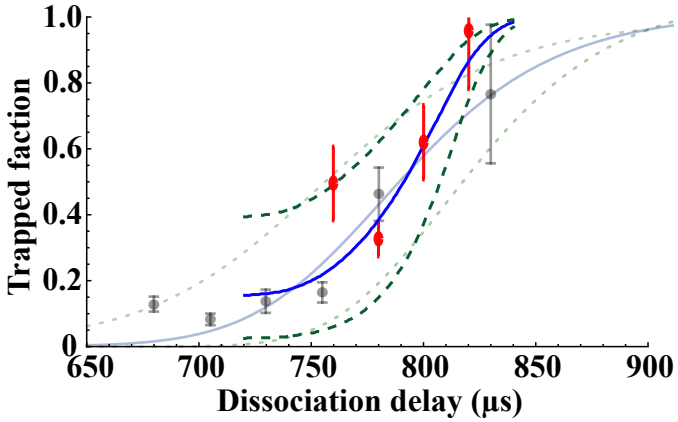

Figure 5.16: Fraction of initially trapped Br atoms remaining after collisions with the molecular beam. The case of using a chopper construct (red dots) is compared with that without the chopper (watermark), the latter being a replica of figure 4.4. The solid blue line is a non-linear fit to the kinetic model described in equation 4.3. The dashed lines indicate the case in which the peak Ar density in the molecular beam is assumed to be a factor of two lesser and greater (upper and lower curves, respectively).

The peak density of Ar, $[\mathrm{Ar}](t')$, is calculated to be $(0.8 \pm 0.2) \times 10^{13}\,\mathrm{cm}^{-3}$ from the best fit of the data to the model. The upper and lower dashed lines indicate the same trend for a molecular beam density a factor of two lower and higher, respectively. The peak density of the chopped molecular beam is about 4 times lower than that for the un-chopped molecular beam ($(3.0 \pm 0.3) \times 10^{13}\,\mathrm{cm}^{-3}$, shown in figure 4.4), potentially due to a lower number of Ar atoms in the molecular beam passing through the chopper.

This value is much lower than the amount of reduction in density of initially trapped Br atoms with the chopper running at 3,000 rpm (measured in section 5.7.1 to be a factor of 40). Both values should, in fact, be the same. As the fraction of Br_2 molecules seeded in the molecular beam is expected to be independent of whether or not a chopper construct is used, the percentage of decrease of carrier gas density in the presence of the chopper construct should be the same as that of initially trapped Br atoms. A combination of different factors may lead to a significant drop in the Br signal between figures 5.15 and 5.16. For example, a decrease in the detection efficiency of the MCPs may occur due to exposure to the halogen atoms over time.

Fluctuations in the intensity or misalignment of the dissociation and REMPI lasers may also lead to a drop in signal. Furthermore, the fit for the peak density of Ar in figure 5.16 clearly shows a larger uncertainty than that with an un-chopped beam (figure 4.4), particularly due to the inability for the model to fit well to the data (red dots) at the lowest and highest dissociation delays. Nonetheless, the uncertainties in these measurements and the model should not lead to such a large discrepancy between the two values found for the amount of reduction in density of initially trapped Br atoms in the presence of the chopper construct. The reason for this discrepancy is not know at the present time, and further experiments should be performed to obtain a more accurate value for the amount of reduction.

At early molecular beam delays, a greater amount of initially trapped Br atoms produced with a chopped molecular beam is maintained, as expected with a shortened beam width. The dissociation delay on the x-axis of figure 5.16 spans a smaller range than that in figure 4.4, due to the shortened duration of the molecular beam passing through the chopper slit. As a result, fewer Ar atoms will be in a chopped molecular beam, and fewer collisions with the initially trapped Br atoms will occur. Therefore, the fraction of initially trapped Br atoms formed at the front of the molecular beam (at the earliest delays in figure 5.16) should be higher than that in the absence of the chopper construct. The model (blue line) shows that of the Br atoms formed at the front of the molecular beam, 15% will still remain trapped, even after undergoing collisions with nearly the entire molecular beam. It is interesting to compare this with forming Br atoms in front of an un-chopped molecular beam in figure 4.4, where almost none of the initially trapped Br atoms will remain after undergoing molecular beam collisions. As the revolution speed of the chopper increases, the duration of the molecular beam will shorten further, and therefore this percentage is expected to increase. The trend is similar in both figures; close to the tail at long delays, the percentage of initially trapped Br atoms remaining in the trap is close to 100%.

However, near the centres of both curves, which are overlapped at a dissociation delay of 780 μs, this trend is reversed, and the fraction of initially trapped Br atoms is marginally lower after collisions with an un-chopped beam. It is hard to confirm this dip in trapped fraction of Br atoms near the peak of a chopped molecular beam, given the signal to noise ratio. Most of the data points with a chopped beam fall above those with an un-chopped beam. Furthermore, near the peak of the molecular beam (at a delay of 780 μs), the error bars on the data points for both cases overlap. As in the conclusion for figure 5.15, further measurements with improved signal to noise are required to determine whether the fraction of initially trapped Br atoms at the peak of the molecular beam is lower with a chopped beam than without.

5.7.3 Accumulation of trapped Br atoms with a chopper

In simulating collisions with a molecular beam with a chopper running at 3,000 rpm, a square-pulse with a duration of 40 μs can be used (calculated using the same method outlined in section 3.1.3), and the peak densities of the molecular beam using Ar and Kr are reduced by a factor of 40, as determined in the drop in signal intensity in figure 5.15. In addition, a reduction in collisions with Ar in the thermal background is included by assuming that a second turbo-molecular pump in the detection chamber reduces the base pressure down by an order of magnitude to 4 $\times 10^{-8}$ mbar. This pressure may vary accordingly with many factors, such as the size of the chamber pressure used, choice of o-ring, location of the turbo-pump, and diameter of the skimmer separating the source and detection chambers.

An improvement with reduced molecular beam duration can be seen in the predictions of figure 5.17.

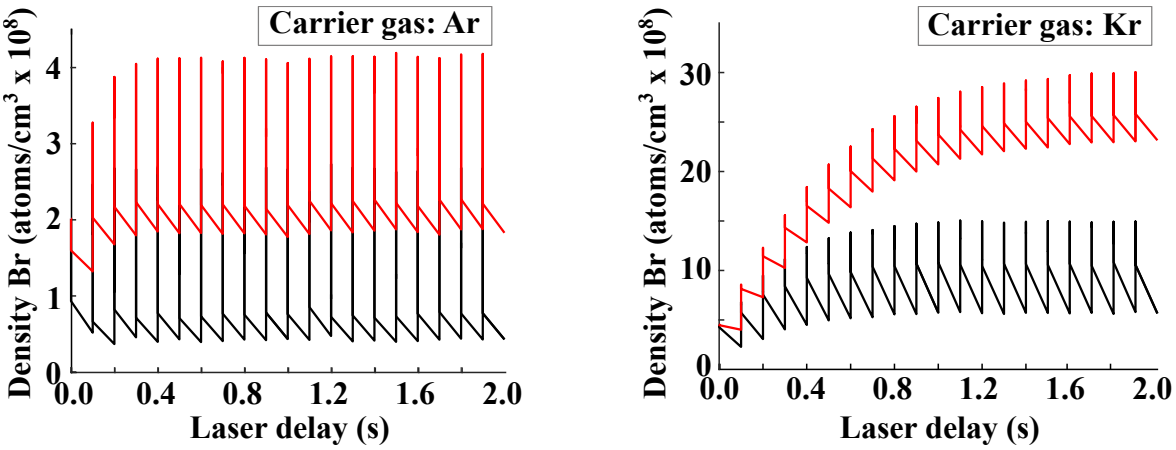

Figure 5.17: Loading curves with Br prepared from a beam of Br_2 seeded in Ar (left) and in Kr (right). In each plot, the case with a chopper running at 3,000 rpm and a reduced base chamber pressure at 4 $\times 10^{-8}$ mbar (red) is compared with the original trap loading curves in figure 3.11.

Simulations of trap loading for trapped Br atoms prepared using Ar (left) and Kr (right) as the carrier gas, with reductions in collisions with Ar in the molecular beam and in the thermal background (red) are compared with the original plots in figure 3.11 (black). To isolate the effects the role of the chopper construct in reducing collisional trap loss in the accumulation cycle, the initial amount of trapped Br atoms is assumed to be the same as in the case without the chopper. Thus, the reduction in initially trapped Br atoms due to the presence of a chopper (shown in section 5.7.1) is ignored in the simulation.

The density of trapped Br atoms after one gas pulse, prepared in Ar, and with a chopper running at 3,000 rpm and a reduced base chamber pressure (red, left), is increased by a factor of 1.4 by the accumulation cycle. Taking the density of initially trapped Br atoms prepared in Ar to be 2.0 $\times$ 10^8 cm^{-3} (calculated in section 3.3), the total density of trapped Br atoms achieved by the accumulation cycle is 1.8 $\times$ 10^8 cm^{-3}, reached in just under 0.5 s, or 5 gas pulses. Similarly, in the case of using Kr as the carrier gas, and with a chopper running at 3,000 rpm and a reduced base chamber pressure (red, right), the total density of trapped Br atoms achieved

by the accumulation cycle is 23.2 $\times 10^8$ cm^{-3}, an increase by a factor of 5.8 from that remaining after one gas pulse. This density is reached in 2 s, or 20 gas pulses, and is 9 times greater than that achieved by the accumulation cycle without the presence of a chopper construct (black, right).

The case of using Ar as the carrier gas clearly appears to be less favourable than that using Kr. Although the number density of atoms in the molecular beam is lower using Ar than using Kr, and although the DCSs in both instances of scattering in the molecular beam and background gas collisions exhibit similar propensities toward forward-scattering, as calculated in section 3.5, the lower relative velocity between the Br and Kr atoms, the smaller ICS in the molecular beam collisions, and the increased number of initially trapped Br atoms, are main contributors to the overall decrease in collisional trap loss effects. Thus, substituting Kr for Ar as the choice of carrier gas, in addition to implementing a chopper construct, a second turbo-molecular pump, and a mechanism to maintain density of initially trapped Br atoms, are highly suggestive of the potential to maintain and accumulate density of trapped Br atoms over successive molecular beam cycles. However, the greatest challenge to be solved is maintaining the initial density of trapped Br atoms in the presence of the chopper construct.

5.8 Summary and suggestions for future improvements

In summary, a novel custom-built chopper construct has been implemented to shorten the duration of a molecular beam by a factor of 10 to 13 μs. With just a few robust components, this method is particular useful for experiments using corrosive species, such as halogens, as the seed molecules in molecular beams. The use of a brushless DC motor enables the chopper to run at a range of speeds from 3,000 rpm to 80,000 rpm,

limited only by the cooling of the motor. This range of speeds produces a range of molecular beam widths ranging from 80 μs to 13 μs. The beam widths are reproducible and independent of the molecular species. Measurements of the beam widths as a function of chopper wheel revolution speed closely match the theoretical model, w_{beam}, plotted in figure 5.11.

It is interesting to note that, despite the dependence of the rotational temperature of the molecular beam on gas pressure, the resulting beam widths measured at revolution speeds of 3,000 rpm at the laser detection volume are observed to be within the error bars of the data plotted in figure 5.11, which are all taken at a constant gas pressure of 2×10^{-5} mbar. This observation indicates that the flight time of the molecular beam from the chopper slit to the laser detection volume is short enough for the variations of source chamber pressure to have no significant effect on the duration of the transmitted molecular beam pulse.

Modification of the experimental set-up is necessary to decrease the pulse duration below 13 μs. First, implementing additional cooling to the motor rotor can increase the revolution speed at which it operates, while still maintaining its temperature below 80 °C. Furthermore, decreasing the overall temperature of the motor as it operates will increase its durability. The small size of the source chamber limits the ability to more efficiently cool the motor, for example, causing the motor to heat up from 25°C to 80°C within the span of 10 min for the case of the chopper wheel spinning at 70,000 rpm. Continued operation under these conditions will cause the motor bearings to erode or crack, and the motor will eventually break down. Expanding the size of our source chamber could accommodate a cooling water system or a larger metal holder for the motor that would allow better heat exchange.

The Series 9 valve could also be cooled, in order to decrease the spread of velocities around the moving frame of the carrier gas, thereby increasing the number of Br_2 seed molecules that are velocity-selected when passing through the two skimmers. The

width of the molecular beam can be decreased further by relocating the chopper wheel closer to the detection region, as shown in figure 5.1, thereby lowering the threshold at which the beam width is limited by the longitudinal velocity distribution, as shown in figure 5.11.

In conclusion, a chopper will serve to limit collisional losses arising from the molecular beam, but at a cost of decreasing the absolute number of Br atoms initially formed. Further work must be done to vary the experimental parameters, such as the type of carrier gas, chopper speed, and distance from the chopper slit to the detection region, in order to maximise the density of trapped atoms at laser delays at least to 100 ms.

The ability to use such a simple, yet durable system, offers an opportunity to expand the breadth of chemical systems for which short-pulse molecular beams can be used.

Chapter 6

Conclusions and Future Outlook

6.1 Summary

In summary, the feasibility of producing a dense, cold sample of halogen atoms has been illustrated, for the first time.

The combination of the Photostop method and a magnetic trap was shown to produce cold Br atoms in a detection volume. Br atoms were formed via photolysis of molecular Br_2 seeded in Ar. The spin-orbit ground $^2P_{3/2}$ states were detected by (2+1) REMPI, and a Monte Carlo Markov chain (MCMC) fitting method using (maximum likelihood estimation) MLE (described in Appendix 1) was implemented to detect the trapped Br atoms at intensities on the order of the background noise.

A magnetic trap with a depth of 0.22 T was used to confine the slowest Br atoms. The trap depth for ground-state Br atoms was measured to be $U_0/k_B = 255$ mK with the upper and lower standard error $[215, 325]$ mK, equivalent to having velocities below 7.9 m/s. At a measured peak Ar density of $3.0\times10^{13}\,cm^{-3}$, the density of initially trapped Br atoms was calculated to be 2.0×10^8 cm^{-3}, corresponding to around 8000 atoms. The trapped Br atoms were detected at laser delays up to 99 ms, suggesting the potential for Br atoms to be accumulated over successive laser pulses at a rate

of 10 Hz. However, a high fraction of Br atoms was found to be lost from the trap; the decay was found to be initially dominated by ballistic expansion of the fastest atoms and by collisions with the molecular beam, and, beyond 5 ms, by collisions with the thermal background.

The three primary causes of trap loss, elastic collisions with the molecular beam and with the thermal background and quantum-state transitions to high-field seeking states near the trap minimum, were investigated theoretically and experimentally. A Monte-Carlo simulation was developed to model the trap loss dynamics and accumulation cycle of the trapped Br atoms. DCSs were calculated for the Br–Ar and Br–Kr scattering systems, which were found to have a propensity for forward-scattering. These were used to generate a cumulative distribution function (CDF) to calculate the post-collisional trajectories of the simulated atoms. The total integrated cross section (ICS) was used to calculate the probability of a collision occurring at a given simulated time step. Over the duration of one molecular beam cycle (0.1 s), simulations show that 54% of initially trapped Br atoms were lost due to molecular beam collisions, and 44% due to collisions with the background gas. Experimental measurements showed similar values of 60% and 66%, respectively. Simulations show that the use of Kr as a carrier gas, as opposed to Ar in the experiment, would enable a higher initial density of Br atoms to be formed at each molecular beam pulse and allow accumulation to occur.

The major cause of trap loss, found to be elastic collisions with the molecular beam, was minimised by shortening the gas pulse through the design and implementation of a novel mechanical chopper construct. However, the initial density of trapped Br atoms was compromised, thus reducing the total amount of detected Br atoms by factors of 40 and 160 for chopper revolution speeds of 3,000 rpm and 6,000 rpm, respectively. An experiment that fitted the decay behaviour of the Br_2 in the molecular beam pulse to a model suggested that the initial density of Ar in the molecular beam was only

reduced by a factor of 4. The reasons for this lower factor compared to the apparent Br reduction were not clear.

The chopper construct was demonstrated to work with corrosive seed molecules and resulted in beam widths consistent with different seed molecules (in this case, NO and Br_2). Over a range of chopper speeds, from 3,000 rpm to 80,000 rpm, the beam width, measured at the centre of the magnetic trap, ranged from 80 μs to 13 μs. The lowest beam width achieved was a factor of 10 smaller than the FWHM of the un-chopped molecular beam. Simulations suggested that the use of a chopper could enhance the density build-up in an accumulation cycle, provided that there was not a substantial reduction in the initial Br density. In the cases using either Ar or Kr as a carrier gas, the densities of trapped atoms after one gas pulse were calculated to increase by factors of 1.4 and 5.8, respectively. Reaching a high enough density of cold Br atoms can enable experimental investigation of cold chemical reactions, described in section **??**.

6.2 Improving the number density and temperature of cold Br atoms

At low temperatures, reactive collision between the trapped, cold Br and a second cold co-reactant can be observed in "barrierless" processes, as described in section 1.1. The ability to observe chemical reaction requires the rate of loss of Br atoms from the trap as a result of reaction to be greater than that due to the sum of all loss mechanisms described in chapters 3 and 4. The two primary forms of trap loss, collisions with Ar in the molecular beam and background gasses, measured in chapter 4 to be 60% and 34 $\pm$ 3% at the end of one molecular beam cycle, respectively, contribute to a total loss of around 94% of the initial gas pulse, thus creating significant difficulty

in observing trap loss due to chemical reactions. Thus, accumulation of trapped Br atoms over successive molecular beam cycles is required to provide sufficient density of trapped Br for chemical reactions to be observed.

The accumulation cycle will also enable one to increase the time that chemical reactions can be observed. The reactive cross section can be conservatively estimated to be 10 $\mathring{A}^2$ [3]; and assuming that the co-reactant has a similar maximum velocity as the trapped Br atoms (such as using a Stark or Zeeman decelerator), the relative velocity can be estimated to be on the order of 10 m/s. Then, the rate coefficient of the reactants is on the order of 10^{-12} cm^3/s. As a comparison, the rate coefficients for radical–neutral reactions are on the order of 10^{-11} cm^3/s for reactions at temperatures of on the order of 10 K, such as that between $S(^1D_2)$ and $H_2(X^1\Sigma_g^+, \nu = 0, J = 0, 1)$ to form $SH(X^2\Sigma, \nu', J')$ and $H(^2S_{1/2})$ at 5.8 K (5.6×10^{-11} cm^3/s) [174], between $N(^4S)$ and $OH(^2\Pi)$ to form $NO(^2\Pi)$ and $H(^2S)$ at 10 K (2.5×10^{-11} cm^3/s) [175,176], between $N(^4S)$ and $NO(^2\Pi)$ to form $N_2(^1\Sigma_g^+)$ and $O(^3P)$ at 10 K (0.7×10^{-11} cm^3/s) [176], and between OH and HBr to form H_2O and Br at 23 K (10.7×10^{-11} cm^3/s) [177].

Assuming that the density of the co-reactant is in excess, and thus, the density of the trapped Br atoms is the limiting reactant, and assuming that the total density of Br (seeded in Ar) reached by the accumulation cycle to be on the order of 10^8 cm^{-3} (calculated in section 3.6), then, the trapped Br atoms would initially decrease at a rate of 10^4 cm^{-3}/s, or 0.01%/s. To observe a fractional reactant depletion of around 10% to at least 1 s, the density of trapped Br atoms would need to be increased by a factor of 10^3, to around 10^{11} cm^{-3}. For observations on the order of 1 ms, the density of trapped Br atoms would need to be increased by an additional factor of 10^3 to around 10^{14} cm^{-3}. This is a very high density of trapped Br atoms and very hard to achieve. Even in the case of using a spinning chopper wheel while maintaining density of initially trapped Br atoms, as well as Kr as the carrier gas, the maximum density of trapped Br atoms achieved by the accumulation cycle is on the order of 10^9 cm^{-3}

(described in section 5.7.3). Thus, the chances of observing chemical reactions with trapped Br atoms at cold temperatures will be greatly improved by the ability to increase density of Br atoms beyond those reported in this thesis, or by choosing a reaction with a larger collisional cross section.

Additional methods can be added to the current experimental set-up to increase the number density of trapped Br atoms. One example discussed in chapter 3 is to reduce the velocity of the Br_2 parent molecules in the molecular beam. The velocity spread of a gas is inversely proportional to its mass, so seeding Br_2 in a heavier gas will result in Br fragments with a lower distribution of recoil velocities, and thus a greater number of Br fragments with velocities below the trap minimum.

As described in section 5.8, the chopper construct can be improved in a number of ways to reduce collisions with the molecular beam and to increase the number density of Br atoms at the detection volume. For example, a shorter molecular beam can be achieved by increasing the maximum revolution speed of the chopper wheel beyond 80,000 rpm, via the addition of a robust cooling system to maintain the motor below the maximum operating temperature. Furthermore, the distance between the chopper wheel and detection volume can be minimised, which in turn minimises the spatial spreading of the molecular beam, shown in section 5.2.1. Finally, moving the pulsed valve closer to the chopper wheel can increase the number of Br_2 molecules with the potential to be photostopped to pass through the chopper slit, described in section 5.7.1.

At time scales on the order of seconds, collisions with Ar atoms in the thermal background can be reduced by lowering the overall base pressure in the detection chamber via additional pumping mechanisms, such as by adding in a second turbo-molecular pump in the detection chamber, or by developing a new chamber with ultra-high vacuum capabilities. In addition, trap loss due to Majorana transitions to high-field seeking states could be observable at long time scales. Trap loss due to

Majorana transitions can be eliminated by adding a positive bias field to the zero field minimum at the centre of the magnetic trap, such as through the use of additional permanent magnets.

To reduce the temperature of the trapped atoms, evaporative cooling can be performed, for example, by clamping each end of the magnet to a piezo-electric actuator and slowly widening the distance between the two magnets. For evaporative cooling to work, the rate of elastic collisions must be much higher than the rate of inelastic collisions, in order to maintain the quantum state of the trapped atoms. However, to obtain a sufficient collision rate between the trapped atoms, densities greater than 10^{10} cm^{-3} would be required [62].

It may be useful to detect trapped Br atoms in states other than the probed spin-orbit ground ^{2}P$_{3/2}$ state, thus increasing the total density of Br atoms detected in the trap. Detection of the spin-orbit excited ^{2}P$_{1/2}$ state could be achieved using a (2+1) REMPI scheme (5p $^2S_{1/2} \leftarrow$ 4p $^2P_{1/2}$) at a wavelength of 243.021 nm [178]. This wavelength region is outside the region accessible with the laser dye used to probe the ground-state Br atoms. In this case, Coumarin 153 can be used, which peaks at a wavelength of 535 nm, or, once doubled, 267.5 nm. Mixing both dyes could enable the ionisation and detection of both the spin-orbit ground and excited states.

6.3 Other atoms and molecules suitable for the Photostop method

In principle, this experiment can be extended to trapping other halogen atoms and free radicals. As described in chapter 2, the primary conditions which determine the feasibility of using the Photostop method to prepare nearly stationary atoms include the following. First, the parent molecule undergoing photodissociation must absorb

at a wavelength with sufficient energy to provide the fragment with a finite velocity. Second, the dissociation channel must have anisotropy parameters close to $\beta = 2$ or -1, i.e. strongly aligned parallel or perpendicular, respectively, to the laser polarisation. It is important to note that at β = -1, the distribution of fragments would be evenly distributed in a symmetric ring around the polarisation axis of the laser (and molecular beam in this geometric set-up); thus a lower fraction of atoms in this configuration will have a velocity within the limits required for the Photostop method. The following examples describe how these conditions could be met by preparing other photostopped free radical species beyond Br. Subsequently, the potential for these species to be confined in a trap is explored.

6.3.1 Preparing photostopped halogen atoms

Cl atoms can be produced by photodissociation of BrCl or Cl_2. In the former case, excited $Cl^*(^2P_{1/2})$ and ground state $Cl(^2P_{3/2})$ atoms can be produced by photodissociation of the parent molecule by light over a range of 442.6 nm to 554.8 nm [179], close to that used in the dissociation of Br_2 in this thesis. Several reaction channels within this range produce Cl atoms with anisotropy parameters (close to $\beta = -1$ and 2, for $Cl^*(^2P_{1/2})$ and $Cl(^2P_{3/2})$, respectively) favourable for the Photostop method.

Similarly, dissociation of Cl_2 to form photostopped Cl atoms can also be achieved close to the photolysis energy used in this thesis, at 480 nm. At this wavelength, the recoil velocity of Cl is 560 m/s which closely matches that of the terminal speed of a molecular beam of Ar [180]. Dissociation of Cl_2 produces spin-orbit ground and excited Cl atoms in two separate branches, recoiling at angular distributions orthogonal to one another. At a dissociation wavelength of 480 nm, the branch formed by a parallel transition dominates, with an anisotropy parameter that approaches 1.9 (compared with 1.8 for Bromine) favourable to the Photostop method. The products formed in

this branch are ground and excited state Cl atoms.

Photostopped F atoms can be achieved by photodissociating ClF, which is the most stable interhalogen molecule containing F [181]. Dissociation of ClF produces ground state $F(^2P_{3/2})$ atoms at a dissociation energy of $D_0 = 20{,}633$ cm^{-1}, and excited state $F^*(^2P_{1/2})$ at $D_0 = 21{,}110$ cm^{-1} (equal to dissociation wavelengths of 473.9 nm and 484.7 nm, respectively) [182]. Its dissociation energy lies in the middle of the B-X absorption band and accessible by tunable visible regime lasers. The $F^*(^2P_{1/2})$ atoms are also formed with a favourable anisotropy parameter ($\beta = 2$).

Isotopes of ^{35}Cl and ^{37}Cl may affect the velocity distribution of the recoiled F and Cl fragments. For example, $F^*(^2P_{1/2})$ products can also be formed by predissociation of ClF, with a different threshold for each parent isotopologue ($D_0 = 21{,}126$ cm^{-1} and 21,136 cm^{-1}, for ^{35}ClF and ^{37}ClF, respectively) [181]. Assuming that the anisotropy parameter for this predissociation channel is $\beta = 2$, and that the photolysis wavelength is set at 464.9 nm (equal to 21,510 cm^{-1}), then the velocities of the recoiled F* atoms would be centred on 560 m/s and on 565 m/s, for the ^{35}ClF and ^{37}ClF parent molecules, respectively. (For the purpose of comparing to differences in recoil velocities between the parent isotopologues of Br in section 2.3, and assuming that Ar is chosen to be the carrier gas, the photolysis wavelength is chosen to be 464.9 nm.) The 5 m/s difference in velocities is smaller than that between the parent isotopologues of Br prepared from Br_2 (calculated in section 2.3 to be 7 m/s), which is minimal. Furthermore, the natural abundance of ^{35}Cl is 76% (and thus, of ^{37}Cl, 24%), making the strongest signal of detected Cl atoms appear from just one isotope (^{35}Cl). Thus, variations in the atomic mass of Cl can be neglected. (In the case that BrCl is chosen as the parent molecule, the velocity distribution of the recoiled Br or Cl fragments would depend on mass variations between the two Cl isomers, as well as between ^{79}Br and ^{81}Br. These mass variations would result in a maximum velocity spread of 12 m/s, which is on the same order as that of Br prepared from Br_2, and thus, minimal.)

6.3.2 Preparing photostopped non-halogen species

The O(^{3}P) radical is another potential atom of interest, particularly due to its significant role in atmospheric chemical dynamics [77]. O(^{3}P) can be formed using the Photostop method from a variety of parent molecules. For example, NO can be dissociated via a 2-colour 2-photon scheme (at wavelengths of 226 nm and 339 nm, both which could be formed from 678 nm, doubled and tripled, respectively, from a tunable dye laser) to form O($^3_2$). The recoil anisotropy parameter (β = -0.67) for a perpendicular transition is close to -1 [183]. Production of O(^{3}P) can also be achieved via a 1-photon dissociation of CO to produce O(^{3}P) fragments, along with C(^{1}D) side products [184]. The anisotropy parameter in this dissociation process is favourable to the Photostop method ($\beta = 2$), but the dissociation threshold is far into the UV region (D_0 = 12.35 eV) and would require a tunable UV laser operable at wavelengths of around 112 nm, which currently does not exist other than those created by frequency tripling or sum frequency mixing methods [185].

It is also possible to photostop molecules, as demonstrated by Wrede et al., who prepared photostopped NO from NO_2 [120]. For example, the NH_2 radical is a prospective molecule to be photostopped. NH_2 fragments can be produced by dissociating NH_3 (D_0 = 37,115 cm^{-1}) via two product branches with orthogonal recoil anisotropy parameters, corresponding to ground state (β = -1) and highly rotationally excited ($\beta = 2$) NH_2 products, respectively [186]. Tuning the polarisation of the laser can enable us to select which type of NH_2 fragment to investigate. However, this method may be complicated by the fact the photodissociation cross section to form NH_2 and H products is very weak near the dissociation threshold and is only significant at shorter wavelengths [187]. The photo-fragments in this dissociation scheme have been observed to have a range of high kinetic energies and high-level rotational energies [186, 188], many of which may be untrappable.

6.3.3 Trapping photostopped atoms and molecules

The ability for such atoms and molecules to be magnetically trapped is dependent on their magnetic moments along the direction of an external weak magnetic field. The magnetic moment of an atom is proportional to its m_J sub-state and the Landé g factor. As these values for the ground and excited states of F and Cl are the same for the ground (g = 4/3) and excited (g = 2/3) states of Br, magnetic trapping mechanisms similar to that used for this thesis can also be used to trap F and Cl. The maximum velocities of F and Cl which lie below the trap limit, would be greater, due to the lighter mass of both atoms. The Landé g factors for $O(^3P_1)$ and for $O(^3P_2)$ are both equal to 1.5 [189], which renders $O(^3P_1)$ and $O(^3P_2)$ to be suitable for magnetic confinement.

Both NH_2 and SO have a triplet ground state and thus could be well suited for magnetic trapping (SO can also be electrostatically trapped), although complications will arise from population of high-level internal states of the molecular fragments with similar recoil angular distributions [186, 190, 191].

The formation of cold Br atoms is a stepping stone to increasing the types of cold and ultracold chemical species that can be generated and trapped, and increasing the possibility for novel studies of chemical reactions in the quantum regime.

Appendix 1

Monte Carlo Markov chain using Maximum Likelihood Estimation

The content in this Appendix is fully drawn from Lam *et al.*, as published in the journal *Physical Review A* [121].

Conventional χ^2 fitting assumes that the error in a signal is normally distributed. This is not the case for small counting-based signals, and background subtraction and fitting can fail at extracting small signals from large backgrounds. The technique used here is derived from Bayesian inference, and seeks the most probable set of fit parameters, given a set of observations [131–133]. The procedure is to define the distribution function for observation errors, derive a likelihood estimator function, then maximise the likelihood value using a Markov Chain Monte Carlo (MCMC) approach to sample the parameter space.

The recorded ion signal is proportional to the number of ions. The probability of observing c counts, given the average expected intensity, μ, follows Poissonian statistics and can be expressed as

$$p(c \mid \mu) = \frac{\mu^c}{c!} \exp\{-\mu\}. \tag{1.1}$$

The likelihood estimator is defined in terms of the probability distribution function (PDF) as:

$$\mathcal{L} = \prod_i p(c_\mathrm{i} \mid \mu_\mathrm{i}(\bar{a})), \tag{1.2}$$

where the expected intensity in a given time bin, $\mu_\mathrm{i}(\bar{a})$ (i.e. the amplitude of a single point in the oscilloscope trace), now depends on a set of model parameters, $\bar{a}$. The product is over all observations, for the case outlined in section 2.5, the entire oscilloscope trace. It is these parameters which are optimised, and for those which fit to the traces shown in figure 2.2, are the set of Gaussian function parameters describing the amplitude, arrival time, and width of the Br signal: $\bar{a}_\mathrm{bg} = [\alpha_1, \beta_1, \gamma_1, \alpha_2, \beta_2, \gamma_2]$ for the 1-colour background, and $\bar{a}_\mathrm{sig} = [\alpha_\mathrm{s}, \beta_\mathrm{s}, \gamma_\mathrm{s}]$ for the 2-colour signal.

The likelihood, $\mathcal{L}$, is also known as the sampling distribution, $p(c \mid \bar{a}, \mathcal{I})$, which is the probability of observing c counts, given parameters $\bar{a}$ and any prior information $\mathcal{I}$. For this thesis, the prior information is the parameter constraints. Bayes' theorem expresses this conditional probability in terms of the posterior probability to be sought, $p(\bar{a} \mid c, \mathcal{I})$, defined as the probability of obtaining parameters $\bar{a}$, given a set of observations c and prior knowledge $\mathcal{I}$ [173, 192]:

$$p(\bar{a} \mid c, \mathcal{I}) = \frac{p(c \mid \bar{a}, \mathcal{I}) p(\bar{a} \mid \mathcal{I})}{p(c \mid \mathcal{I})}, \tag{1.3}$$

where $p(\bar{a} \mid \mathcal{I})$ is the prior distribution, which represents known information about parameters $\bar{a}$ prior to observing c, and $p(c \mid \mathcal{I})$ is a normalising constant that represents the unconditional distribution of c.

A Markov chain samples the posterior distribution, $p(\bar{a} \mid c, \mathcal{I})$, over a series of iterations that converge toward a maximised value of the likelihood estimate, $\mathcal{L}$, in equation 1.2 [193, 194]. At each iteration, the value of $\mathcal{L}_\mathrm{current}$ is calculated from the current set of parameters. A new set of proposed parameters are selected at random from a PDF centred around the value of the current set of parameters. The specific

form of this selection PDF does not affect the converged parameters but is chosen to thoroughly sample the parameter space. In section 2.5, a Gaussian PDF was chosen to sample each parameter with a standard deviation of 10^{-3} of the parameter value, as standard libraries exist for generating random numbers following this distribution. The likelihood value for this new set of parameters, $\mathcal{L}_{\text{proposed}}$, is calculated and compared to the current likelihood, $\mathcal{L}_{\text{current}}$:

$$\alpha \leq \frac{\mathcal{L}_{\text{proposed}}}{\mathcal{L}_{\text{current}}}, \tag{1.4}$$

where α is a random number generated from a uniform distribution from 0 to 1 exclusive. If this inequality is satisfied, then the current set of parameters is replaced with the new set, otherwise the current parameters are kept, and a new set of proposed parameters is generated.

In practise, the logarithm of $\mathcal{L}$ is typically used, rather than the direct value, as it aids numerical convergence:

$$\log \mathcal{L} = \log \left(\prod_{\text{i}} p(c_{\text{i}}; \mu_{\text{i}}(\bar{a})) \right) \tag{1.5}$$

$$= \sum_{i}^{n} \left(-\mu_{\text{i}}(\bar{a}) + c_{\text{i}} \log \mu_{\text{i}}(\bar{a}) \right). \tag{1.6}$$

As $\mathcal{L}$ and $\log \mathcal{L}$ are monotonically related, maximising $\log \mathcal{L}$ produces the same optimised parameters [195].

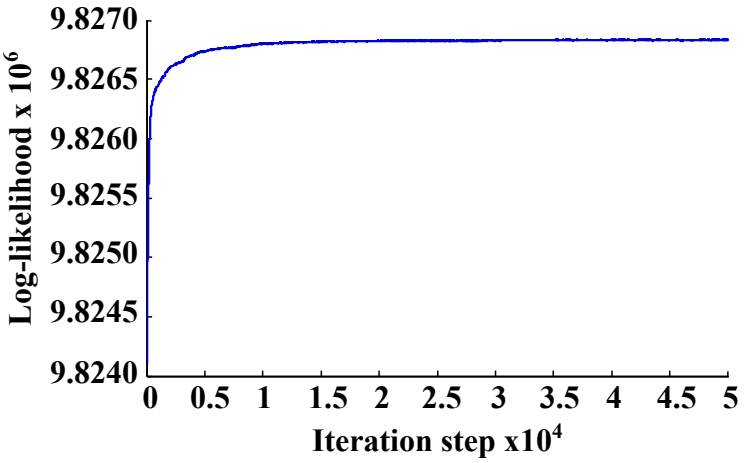

Figure 1.1: Log-likelihood of the parameters used to fit to the 1-colour background as a function of the MCMC iteration. The figure is drawn from Lam et al. [121].

Once the chain has converged, the accepted parameters $\bar{a}$ sample the posterior distribution, $\mathrm{p}(\bar{a} \mid c, \mathcal{I})$, and the mean and standard error of each parameter can be extracted from a sufficient number of iterations.

Appendix 2

Collision cross section for trapped atoms

The content in this Appendix is fully drawn from Lam *et al.*, as published in the journal *Physical Review A* [121].

The relative motion of the colliding atoms along each potential is described by the time-independent Schrödinger equation of the form

$$\Psi_l''(r) = W_l(r)\Psi_l(r), \tag{2.1}$$

where $\Psi_l(r)$ is the radial wavefunction expanded in terms of partial waves, and $W_l(R)$ is a coupling term that depends on the centrosymmetric interaction potential $V(r)$, including a centrifugal contribution:

$$W_l(r) = \frac{2\mu}{\hbar^2}V(r) + \frac{l(l+1)}{r^2} - k^2. \tag{2.2}$$

The collision wave vector depends on the collision energy E: $k^2 = 2\mu E/\hbar^2$. A number of techniques have been developed to solve equations in the form of equation 2.1; in this simple, single-channel case, the log derivative propagator is used with a constant

reference potential. The wavefunction is expanded as the sum of partial waves representing the incoming plane wave, and a spherical outgoing wave, in terms of the Legendre polynomials.

The Log-derivative of the wavefunction is defined as $Y_l(r) = \Psi_l'(r)\Psi_l(r)^{-1}$. Differentiating and substituting the second derivative using (2.1) yields the Ricatti equation, $Y_l'(r) = W_l(r) - Y_l(r)^2$. This equation can not be integrated directly as the log derivative is singular when the wavefunction vanishes, but it can be solved across an interval $(a,\, b)$ by the propagator,

$$Y_l(b) = \mathcal{Y}_4(a,\, b) - \mathcal{Y}_3(a,\, b)\,[Y(a) + \mathcal{Y}_1(a,\, b)]^{-1}\,\mathcal{Y}_2(a,\, b), \tag{2.3}$$

where the propagator elements are

$$\mathcal{Y}_1(a,\, b) = \mathcal{Y}_4(a,\, b) = \begin{cases} |w|\coth|w|h & w^2 \geq 0 \\ |w|\cot|w|h & w^2 < 0 \end{cases} \tag{2.4}$$

$$\mathcal{Y}_2(a,\, b) = \mathcal{Y}_3(a,\, b) = \begin{cases} |w|\mathrm{cosech}|w|h & w^2 \geq 0 \\ |w|\mathrm{cosec}|w|h & w^2 < 0 \end{cases} \tag{2.5}$$

In the case of this single-channel model, w^2 is equal to the coupling matrix, $W_l(r)$, evaluated at $r = a$ and at $h = b - a$. Starting from an initial value $Y_l(r_0)$, with r_0 well within the classical inner turning point, the integration proceeds by propagating out to $Y_l(b)$ in small steps, using the mean interaction potential over the interval.

At the limit of large r the usual asymptotic boundary condition for scattering problems is that the wavefunction can be written as the difference between incoming, $I(r)$, and outgoing, $O(r)$, waves with the collision energy dependent scattering matrix element for a particular partial wave. $S_l(E)$:

$$\Psi_l(r \to \infty) \simeq I_l(r) - O_l(r)S_l(E). \tag{2.6}$$

The values of $I_l(r)$ and $O_l(r)$ are determined by setting the potential to zero, then:

$$I_l(r) = k^{-1/2}\hat{h}_l^-(kr) \tag{2.7}$$

$$O_l(r) = k^{-1/2}\hat{h}_l^+(kr), \tag{2.8}$$

where $\hat{h}_l^-(kr)$ and $\hat{h}_l^+(kr)$ are the incoming and outgoing Riccati-Hankel functions respectively. Substitution of the definition of the log derivative wavefunction into equation 2.6 yields a solution for the scattering matrix element:

$$S_l(E) = \frac{Y_l(r_a)I_l(r_a) - I_l'(r_a)}{Y_l(r_a)O_l(r_a) - O_l'(r_a)}, \tag{2.9}$$

where r_a is some final value of the propagation radius in the asymptotic region of the potential.

References

[1] M. Schnell and G. Meijer. *Angew. Chem. Int. Ed.*, **48**, 6010–6031, 2009.

[2] S. Y. T. van de Meerakker, H. L. Bethlem, and G. Meijer. *Nature Phys.*, **4**, 595–602, 2008.

[3] M. T. Bell and T. P. Softley. *Mol. Phys.*, **107**, 99–132, 2009.

[4] D. G. Truhlar, B. C. Garrett, and S. J. Klippenstein. *J. Phys. Chem.*, **100**, 12771—12800, 1996.

[5] I. W. M. Smith. *Chem. Soc. Rev.*, **37**, 812–826, 2008.

[6] M. T. Cvitaš, P. Soldán, J. M. Hutson, P. Honvault, and J.-M. Launay. *Phys. Rev. Lett.*, **94**, 033201, 2005.

[7] J. van Veldhoven, J. Kpper, H. Bethlem, B. Sartakov, A. van Roij, and G. Meijer. *Eur. Phys. J. D*, **31**, 337–349, 2004.

[8] E. R. Hudson, H. J. Lewandowski, B. C. Sawyer, and J. Ye. *Phys. Rev. Lett.*, **96**, 143004, 2006.

[9] M. R. Tarbutt, J. J. Hudson, B. E. Sauer, and E. A. Hinds. *Faraday Discuss.*, **142**, 37–56, 2009.

[10] R. V. Krems. *Phys. Chem. Chem. Phys.*, **10**, 4079–4092, 2008.

[11] R. Sahai and L. Nyman. *Astrophys. J. Lett.*, **487**, L155–L160, 1997.

[12] E. Herbst. *Chem. Soc. Rev.*, **30**, 168–176, 2001.

[13] D. van Delft. *Freezing Physics: Heike Kamerlingh Onnes and the Quest for Cold*. Edita, 2007.

[14] K. Onnes. Research notebooks, kamerlingh onnes archive, accessed December 20, 2015. `http://www.museumboerhaave.nl`.

[15] J. M. Hayes and G. J. Small. *Anal. Chem.*, **55**, 565A–574A, 1983.

[16] G. Scoles. *Atomic and Molecular Beam Methods*, volume 1-2. Oxford University Press, 1988.

[17] M. D. Morse. In F. Dunning and R. G. Hulet, editors, *Atomic, Molecular, and Optical Physics: Atoms and Molecules*, volume 29, Part B of *Experimental Methods in the Physical Sciences*, chapter 2, 21 – 47. Academic Press, 1996.

[18] A. Osterwalder. *EPJ Tech. Instrum.*, **2**, 1–28, 2015.

[19] D. Gerlich. *J. Chem. Soc. Farad. Trans.*, **89**, 2199–2208, 1993.

[20] M. S. Elioff, J. J. Valentini, and D. W. Chandler. *Science*, **302**, 1940–1943, 2003.

[21] W. Christen and K. Rademann. *Phys. Rev. A*, **77**, 012702, 2008.

[22] S. E. Maxwell, N. Brahms, R. deCarvalho, D. R. Glenn, J. S. Helton, S. V. Nguyen, D. Patterson, J. Petricka, D. DeMille, and J. M. Doyle. *Phys. Rev. Lett.*, **95**, 173201, 2005.

[23] D. Patterson and J. M. Doyle. *J. Chem. Phys.*, **126**, 154307, 2007.

[24] D. Egorov, T. Lahaye, W. Schöllkopf, B. Friedrich, and J. M. Doyle. *Phys. Rev. A*, **66**, 043401, 2002.

[25] V. Ghazarian, J. Eloranta, and V. A. Apkarian. *Rev. Sci. Instrum.*, **73**, 3606–3613, 2002.

[26] R. Dörner, V. Mergel, R. Ali, U. Buck, C. L. Cocke, K. Froschauer, O. Jagutzki, S. Lencinas, W. E. Meyerhof, S. Nüttgens, R. E. Olson, H. Schmidt-Böcking, L. Spielberger, K. Tökesi, J. Ullrich, M. Unverzagt, and W. Wu. *Phys. Rev. Lett.*, **72**, 3166–3169, 1994.

[27] M. Strebel, F. Stienkemeier, and M. Mudrich. *Phys. Rev. A*, **81**, 033409, 2010.

[28] M. Gupta and D. Herschbach. *J. Phys. Chem. A*, **103**, 10670–10673, 1999.

[29] L. Sheffield, M. S. Hickey, V. Krasovitskiy, K. D. D. Rathnayaka, I. F. Lyuksyutov, and D. R. Herschbach. *Rev. Sci. Instrum.*, **83**, 064102, 2012.

[30] M. Hillenkamp, S. Keinan, and U. Even. *J. Chem. Phys.*, **118**, 8699–8705, 2003.

[31] S. Chu, L. Hollberg, J. E. Bjorkholm, A. Cable, and A. Ashkin. *Phys. Rev. Lett.*, **55**, 48–51, 1985.

[32] C. Adams and E. Riis. *Prog. Quant. Electron.*, **21**, 1 – 79, 1997.

[33] W. D. Phillips. *Rev. Mod. Phys.*, **70**, 721–741, 1998.

[34] T. W. Hänsch and A. L. Schawlow. *Opt. Commun.*, **13**, 68 – 69, 1975.

[35] D. Wineland and H. Dehmelt. *Bull. Am. Phys. Soc.*, **20**, 637–637, 1975.

[36] W. Ketterle, K. B. Davis, M. A. Joffe, A. Martin, and D. E. Pritchard. *Phys. Rev. Lett.*, **70**, 2253–2256, 1993.

[37] C. Gabbanini, A. Fioretti, A. Lucchesini, S. Gozzini, and M. Mazzoni. *Phys. Rev. Lett.*, **84**, 2814–2817, 2000.

[38] Z. T. Lu, K. L. Corwin, M. J. Renn, M. H. Anderson, E. A. Cornell, and C. E. Wieman. *Phys. Rev. Lett.*, **77**, 3331–3334, 1996.

[39] K. Dieckmann, R. J. C. Spreeuw, M. Weidemüller, and J. T. M. Walraven. *Phys. Rev. A*, **58**, 3891–3895, 1998.

[40] C. J. Myatt, N. R. Newbury, R. W. Ghrist, S. Loutzenhiser, and C. E. Wieman. *Opt. Lett.*, **21**, 290–292, 1996.

[41] N. R. Hutzler, H.-I. Lu, and J. M. Doyle. *Chem. Rev.*, **112**, 4803–4827, 2012.

[42] S. E. Maxwell, N. Brahms, R. deCarvalho, D. R. Glenn, J. S. Helton, S. V. Nguyen, D. Patterson, J. Petricka, D. DeMille, and J. M. Doyle. *Phys. Rev. Lett.*, **95**, 173201, 2005.

[43] K. S. Twyman. D.Phil thesis, University of Oxford, 2013.

[44] S. Y. T. van de Meerakker, H. L. Bethlem, N. Vanhaecke, and G. Meijer. *Chem. Rev.*, **112**, 4828–4878, 2012.

[45] M. Lemeshko, R. V. Krems, J. M. Doyle, and S. Kais. *Mol. Phys.*, **111**, 1648–1682, 2013.

[46] S. D. Hogan, M. Motsch, and F. Merkt. *Phys. Chem. Chem. Phys.*, **13**, 18705–18723, 2011.

[47] E. Narevicius and M. G. Raizen. *Chem. Rev.*, **112**, 4879–4889, 2012.

[48] R. Fulton, A. I. Bishop, M. N. Shneider, and P. F. Barker. *Nature Phys.*, **2**, 465–468, 2006.

[49] N. Vanhaecke, U. Meier, M. Andrist, B. H. Meier, and F. Merkt. *Phys. Rev. A*, **75**, 031402, 2007.

[50] E. Narevicius, A. Libson, C. G. Parthey, I. Chavez, J. Narevicius, U. Even, and M. G. Raizen. *Phys. Rev. Lett.*, **100**, 093003, 2008.

[51] C. Sommer, M. Motsch, S. Chervenkov, L. D. van Buuren, M. Zeppenfeld, P. W. H. Pinkse, and G. Rempe. *Phys. Rev. A*, **82**, 013410, 2010.

[52] L. S. Brown and G. Gabrielse. *Rev. Mod. Phys.*, **58**, 233–311, 1986.

[53] W. Paul. *Rev. Mod. Phys.*, **62**, 531–540, 1990.

[54] S. Willitsch, M. T. Bell, A. D. Gingell, and T. P. Softley. *Phys. Chem. Chem. Phys.*, **10**, 7200–7210, 2008.

[55] A. K. Hansen, O. O. Versolato, L. Klosowski, S. B. Kristensen, A. Gingell, M. Schwarz, A. Windberger, J. Ullrich, Lopez-Urrutia, J. R. Crespo, and M. Drewsen. *Nature*, **508**, 76 – 79, 2014.

[56] S. Mavadia, J. F. Goodwin, G. Stutter, S. Bharadia, D. R. Crick, D. M. Segal, and R. C. Thompson. *Nat. Commun.*, **4**, 1–7, 2013.

[57] M. H. Anderson, J. R. Ensher, M. R. Matthews, C. E. Wieman, and E. A. Cornell. *Science*, **269**, 198–201, 1995.

[58] J. R. Anglin and W. Ketterle. *Nature*, **416**, 211–218, 2002.

[59] E. Arimondo, W. D. Phillips, and F. Strumia. *Laser Manipulation of Atoms and Ions*. Elsevier, 1992.

[60] H. J. Metcalf and P. v. d. Straten. *Laser Cooling and Trapping*. Springer-Verlag New York, Inc., 1999.

[61] J. J. Tollett, C. C. Bradley, C. A. Sackett, and R. G. Hulet. *Phys. Rev. A*, **51**, R22–R25, 1995.

[62] N. Masuhara, J. M. Doyle, J. C. Sandberg, D. Kleppner, T. J. Greytak, H. F. Hess, and G. P. Kochanski. *Phys. Rev. Lett.*, **61**, 935–938, 1988.

[63] L. D. Carr, D. DeMille, R. V. Krems, and J. Ye. *New J. Phys.*, **11**, 055049, 2009.

[64] J. F. Barry, D. J. McCarron, E. B. Norrgard, M. H. Steinecker, and D. DeMille. *Nature*, **512**, 286–289, 2014.

[65] S. Inouye, M. R. Andrews, J. Stenger, H.-J. Miesner, D. M. Stamper-Kurn, and W. Ketterle. *Nature*, **392**, 151–154, 1998.

[66] K. M. Jones, E. Tiesinga, P. D. Lett, and P. S. Julienne. *Rev. Mod. Phys.*, **78**, 483–535, 2006.

[67] J. M. Sage, S. Sainis, T. Bergeman, and D. DeMille. *Phys. Rev. Lett.*, **94**, 203001, 2005.

[68] V. S. Bagnato, G. P. Lafyatis, A. G. Martin, E. L. Raab, R. N. Ahmad-Bitar, and D. E. Pritchard. *Phys. Rev. Lett.*, **58**, 2194–2197, 1987.

[69] J. Kim, B. Friedrich, D. P. Katz, D. Patterson, J. D. Weinstein, R. DeCarvalho, and J. M. Doyle. *Phys. Rev. Lett.*, **78**, 3665–3668, 1997.

[70] J. M. Doyle, B. Friedrich, J. Kim, and D. Patterson. *Phys. Rev. A*, **52**, R2515–R2518, 1995.

[71] J. D. Weinstein, R. deCarvalho, T. Guillet, B. Friedrich, and J. M. Doyle. *Nature*, **395**, 148–150, 1998.

[72] W. C. Campbell, G. C. Groenenboom, H.-I. Lu, E. Tsikata, and J. M. Doyle. *Phys. Rev. Lett.*, **100**, 083003, 2008.

[73] M. Stoll, J. M. Bakker, T. C. Steimle, G. Meijer, and A. Peters. *Phys. Rev. A*, **78**, 032707, 2008.

[74] J. Riedel, S. Hoekstra, W. Jger, J. Gilijamse, S. van de Meerakker, and G. Meijer. *Eur. Phys. J. D*, **65**, 161–166, 2011.

[75] B. C. Sawyer, B. K. Stuhl, D. Wang, M. Yeo, and J. Ye. *Phys. Rev. Lett.*, **101**, 203203, 2008.

[76] J. Lelieveld, F. J. Dentener, W. Peters, and M. C. Krol. *Atmos. Chem. Phys.*, **4**, 2337–2344, 2004.

[77] L. A. Barrie, J. W. Bottenheim, R. C. Schnell, P. J. Crutzen, and R. A. Rasmussen. *Nature*, **334**, 138 – 141, 1988.

[78] I. Fridovich. *Science*, **201**, 875–880, 1978.

[79] M. Valko, C. Rhodes, J. Moncol, M. Izakovic, and M. Mazur. *Chem.-Biol. Interact.*, **160**, 1 – 40, 2006.

[80] T. Finkel and N. J. Holbrook. *Nature*, **408**, 239–247, 2000.

[81] M. H. Alexander, D. E. Manolopoulos, and H.-J. Werner. *J. Chem. Phys.*, **113**, 11084–11100, 2000.

[82] D. E. Manolopoulos. *J. Chem. Soc. Farad. Trans.*, **93**, 673–683, 1997.

[83] M. H. Alexander, G. Capecchi, and H.-J. Werner. *Science*, **296**, 715–718, 2002.

[84] B. Jiang, C. Xie, and D. Xie. *J. Chem. Phys.*, **135**, 164311, 2011.

[85] J. Klos, M. M. Szczesniak, and G. Chalasinski. *Int. Rev. Phys. Chem.*, **23**, 541–571, 2004.

[86] H. A. Michelsen and W. R. Simpson. *J. Phys. Chem. A*, **105**, 1476–1488, 2001.

[87] S. M. Senkan, J. M. Robinson, and A. K. Gupta. *Combust. Flame*, **49**, 305–314, 1983.

[88] E. S. Campbell and R. M. Fristrom. *Chem. Rev.*, **58**, 173–234, 1958.

[89] I. W. M. Smith and P. W. Barnes. *Annu. Rep. Prog. Chem., Sect. C: Phys. Chem.*, **109**, 140–166, 2013.

[90] I. R. Sims, I. W. M. Smith, D. C. Clary, P. Bocherel, and B. R. Rowe. *J. Chem. Phys.*, **101**, 1748–1751, 1994.

[91] R. Krems and A. Dalgarno. *J. Chem. Phys.*, **117**, 118–123, 2002.

[92] P. F. Weck and N. Balakrishnan. *Int. Rev. Phys. Chem.*, **25**, 283–311, 2006.

[93] P. F. Weck and N. Balakrishnan. *J. Phys. B: At. Mol. Opt. Phys.*, **39**, S1215–S1227, 2006.

[94] N. Balakrishnan and A. Dalgarno. *Chem. Phys. Lett.*, **341**, 652 – 656, 2001.

[95] N. Balakrishnan. *J. Chem. Phys.*, **121**, 5563–5566, 2004.

[96] P. C. Samartzis, T. N. Kitsopoulos, and M. N. R. Ashfold. *Phys. Chem. Chem. Phys.*, **2**, 453–459, 2000.

[97] T. G. Lindeman and J. R. Wiesenfelda. *J. Chem. Phys.*, **70**, 2882–2888, 1979.

[98] H. J. Wörner, J. B. Bertrand, P. B. Corkum, and D. M. Villeneuve. *Phys. Rev. Lett.*, **105**, 103002, 2010.

[99] K. Mohanakumar. *Stratosphere Troposphere Interactions: An Introduction.* Springer Netherlands, 2008.

[100] M. J. Kurylo. *Short-lived ozone-related compounds*, chapter 2, 2.1–2.56. World Meteorol. Org., 1998.

[101] W. T. Sturges, H. P. McIntyre, S. A. Penkett, J. Chappellaz, J. Barnola, R. Mulvaney, E. Atlas, and V. Stroud. *J. Geophys. Res.*, **106**, 1595–1606, 2001.

[102] S. A. Yvon-Lewis, J. H. Butler, E. S. Saltzman, P. A. Matrai, D. B. King, R. Tokarczyk, R. M. Moore, and J.-Z. Zhang. *Glob. Biogeochem. Cy.*, **16**, 88, 2002.

[103] L. M. Anthony and J. M. Roscoe. *J. Phys. Chem. A*, **108**, 7535–7547, 2004.

[104] P. L. Laine, Y. S. Sohn, J. M. Nicovich, M. L. McKee, and P. H. Wine. *J. Phys. Chem. A*, **116**, 6341–6357, 2012.

[105] A. Bierbach, I. Barnes, and K. H. Becker. *Int. J. Chem. Kinet.*, **28**, 565–577, 1996.

[106] T. J. Wallington, L. M. Skewes, W. O. Siegl, and S. M. Japar. *Int. J. Chem. Kinet.*, **21**, 1069–1076, 1989.

[107] I. Barnes, V. Bastian, K. H. Becker, R. Overath, and Z. Tong. *Int. J. Chem. Kinet.*, **21**, 499–517, 1989.

[108] V. Hanninen, M. Horn, and L. Halonen. *J. Chem. Phys.*, **111**, 3018–3026, 1999.

[109] R. H. Hunt, W. N. Shelton, F. A. Flaherty, and W. B. Cook. *J. Mol. Spectrosc.*, **192**, 277–293, 1998.

[110] K. Takahashi, E. Iwasaki, and Y. Matsumi. *Chemical Physics Letters*, **463**, 50 – 53, 2008.

[111] H. B. Stewart and H. H. Nielsen. *Phys. Rev.*, **75**, 640–650, 1949.

[112] G. M. Barrow. *Physical chemistry.* 2nd edition, 1966.

[113] D. Kolbe, M. Scheid, and J. Walz. *Phys. Rev. Lett.*, **109**, 063901, 2012.

[114] A. Kramida, Yu. Ralchenko, J. Reader, and and NIST ASD Team. Nist atomic spectra database, accessed November 11, 2015. `http://physics.nist.gov/asd`.

[115] K. Dulitz. D.Phil thesis, University of Oxford, 2014.

[116] W. G. Doherty, M. T. Bell, T. P. Softley, A. Rowland, E. Wrede, and D. Carty. *Phys. Chem. Chem. Phys.*, **13**, 8441–8447, 2011.

[117] S. J. Matthews, S. Willitsch, and T. P. Softley. *Phys. Chem. Chem. Phys.*, **9**, 5656–5663, 2007.

[118] T. P. Rakitzis and R. N. Zare. *J. Chem. Phys.*, **110**, 3341–3350, 1999.

[119] B. S. Zhao, S. E. Shin, S. T. Park, X. Sun, and D. S. Chung. *J. Phys. Soc. Jpn.*, **78**, 094302, 2009.

[120] A. Trottier, D. Carty, and E. Wrede. *Mol. Phys.*, **109**, 725–733, 2011.

[121] J. Lam, C. J. Rennick, and T. P. Softley. *Phys. Rev. A*, **90**, 063419, 2014.

[122] C. J. Rennick, J. Lam, W. G. Doherty, and T. P. Softley. *Phys. Rev. Lett.*, **112**, 023002, 2014.

[123] W. G. Doherty, M. T. Bell, T. P. Softley, A. Rowland, E. Wrede, and D. Carty. *Phys. Chem. Chem. Phys.*, **13**, 8441–8447, 2011.

[124] M. J. Cooper, E. Wrede, A. J. Orr-Ewing, and M. N. R. Ashfold. *J. Chem. Soc. Farad. Trans.*, **94**, 2901–2907, 1998.

[125] R. Engel-Herbert and T. Hesjedal. *Appl. Phys.*, **97**, 074504, 2005.

[126] J. Lam, C. J. Rennick, and T. P. Softley. *Rev. Sci. Instrum.*, **86**, 053108, 2015.

[127] R. O. Johnson, G. P. Perram, and W. B. Roh. *J. Chem. Phys.*, **104**, 7052–7058, 1996.

[128] R. Barrow, D. Broyd, L. Pederson, and K. Yee. *Chem. Phys. Lett.*, **18**, 357 – 358, 1973.

[129] M. Beckert, S. Greaves, and M. Ashfold. *Phys. Chem. Chem. Phys.*, **5**, 308 – 314, 2003. Publisher: Royal Society of Chemistry.

[130] W. G. Doherty. D.Phil thesis, University of Oxford, 2012.

[131] P. J. Green. *Biometrika*, **82**, 711–732, 1995.

[132] W. K. Hastings. *Biometrika*, **57**, 97–109, 1970.

[133] D. A. van Dyk, A. Connors, V. L. Kashyap, and A. Siemiginowska. *Astrophys. J.*, **548**, 224–243, 2001.

[134] D. Baird. *Experimentation: An Introduction to Measurement Theory and Experiment Design.* Introduction to Measurement Theory and Experimental Design. Prentice-Hall, 1995.

[135] P. Cassavecchia, G. He, R. K. Sparks, and Y. T. Lee. *J. Chem. Phys.*, **75**, 710–721, 1981.

[136] L. Verlet. *Phys. Rev.*, **159**, 98–103, 1967.

[137] A. A. Buchachenko, T. A. Grinev, T. G. Wright, and L. A. Viehland. *J. Chem. Phys.*, **128**, 064317, 2008.

[138] M. Zubek, B. Mielewska, and G. C. King. *J. Phys. B: At. Mol. Opt. Phys.*, **33**, L527–L532, 2000.

[139] J. Van Dongen, C. Zhu, D. Clement, G. Dufour, J. L. Booth, and K. W. Madison. *Phys. Rev. A*, **84**, 022708, 2011.

[140] W. Demtröder. *Laser spectroscopy: Basic concepts and instrumentation.* Springer Verlag., 2nd edition, 1996.

[141] V. Gomer, O. Harms, D. Haubrich, H. Schadwinkel, F. Strauch, B. Ueberholz, S. aus der Wiesche, and D. Meschede. *Hyperfine Interactions*, **109**, 281–292, 1997.

[142] Ketterle and van Druten. *Adv. At. Mol. Opt. Phys.*, **37**, 181, 1996.

[143] W. R. Gentry and C. F. Giese. *Rev. Sci. Instrum.*, **49**, 595–600, 1978.

[144] J. B. Cross and J. J. Valentini. *Rev. Sci. Instrum.*, **53**, 38–42, 1982.

[145] Jordan TOF Components Inc. Manual, accessed June 4, 2014. `http://www.rmjordan.com`.

[146] G. I. Dimov. *Pribory i tekhnika eksperimenta (Nuclear Physics Institute, Academy of Sciences of the USSR)*, **5**, 168–171, 1968.

[147] D. Irimia, D. Dobrikov, R. Kortekaas, H. Voet, D. A. van den Ende, W. A. Groen, and M. H. M. Janssen. *Rev. Sci. Instrum.*, **80**, 113303, 2009.

[148] U. Even, M. Hillenkamp, and S. Keinan. *J. Chem. Phys.*, **118**, 8699–8705, 2003.

[149] U. Even, J. Jortner, D. Noy, N. Lavie, and C. Cossart-Magos. *J. Chem. Phys.*, **112**, 8068–8071, 2000.

[150] B. Yan, P. Claus, B. van Oorschot, L. Gerritsen, A. Eppink, S. van de Meerakker, and D. Parker. *Rev. Sci. Instrum.*, **84**, 023102, 2013.

[151] C. Vargel. *Corrosion of Aluminium.* Referex Engineering. Elsevier, 2004.

[152] B. D. Craig and D. S. Anderson. *Handbook of Corrosion Data.* ASM International, 2nd edition, 1995.

[153] J. R. Davis. *Corrosion of Weldments*. ASM International, 2006.

[154] H. H. Uhlig and R. W. Revie. *Corrosion and Corrosion Control: An Introduction to Corrosion Science and Engineering*. John Wiley and Sons, Inc., 4th edition, 2008.

[155] L. Abad, D. Bermejo, V. J. Herrero, J. Santos, and I. Tanarro. *Rev. Sci. Instrum.*, **66**, 3826–3832, 1995.

[156] J. A. Schwarz and R. J. Madix. *Rev. Sci. Instrum.*, **39**, 1366–1368, 1968.

[157] C. V. Nowikow and R. Grice. *J. Phys. E: Sci. Instrum.*, **12**, 515–521, 1979.

[158] R. D. G. Comsa and B. J. Schumacher. *Rev. Sci. Instrum.*, **52**, 789–796, 1981.

[159] K. Kuhnke, K. Kern, R. David, B. Lindenau, and G. Comsa. *Rev. Sci. Instrum.*, **65**, 653–656, 1994.

[160] W. L. Whittemore. *Rev. Sci. Instrum.*, **37**, 742–745, 1966.

[161] L. Pasternack and P. J. Dagdigian. *Rev. Sci. Instrum.*, **48**, 226–228, 1977.

[162] D. E. Voss and S. A. Cohen. *J. Vac. Sci. Technol.*, **17**, 303–305, 1980.

[163] J. Benedikt, D. Ellerweg, and A. von Keudell. *Rev. Sci. Instrum.*, **80**, 055107, 2009.

[164] P. Madaan. Brushless DC Motors – part i: Construction and Operating Principles, 17 July 2014. `http://www.edn.com`.

[165] W. Brown. Brushless DC Motor Control Made Easy, accessed July 17, 2014. `http://www.electromate.com`.

[166] M. Motors. DC and BLDC Motors with Permanent Magnets, accessed July 17, 2014. `http://www.microchip.com`.

[167] R. G. Bray, R. M. Hochstrasser, and J. E. Wessel. *Chem. Phys. Lett.*, **27**, 167–171, 1974.

[168] D. C. Jacobs, R. J. Madix, and R. N. Zare. *J. Chem. Phys.*, **85**, 5469–5479, 1986.

[169] W. C. Wiley and I. H. McLaren. *Rev. Sci. Instrum.*, **26**, 1150–1157, 1955.

[170] H. R. Griem. *Plasma Spectroscopy*. McGraw-Hill, 1964.

[171] C. M. Western. PGOPHER, a program for simulating rotational structure, accessed June 1, 2014. `http://pgopher.chm.bris.ac.uk`.

[172] A. Savitzky and M. J. E. Golay. *Anal. Chem.*, **26**, 1627–1639, 1964.

[173] W. H. Press, S. A. Teukolsky, W. T. Vetterling, and B. P. Flannery. *Numerical Recipes 3rd Edition: The Art of Scientific Computing*. Cambridge University Press, 1989.

[174] C. Berteloite, M. Lara, A. Bergeat, S. D. Le Picard, F. Dayou, K. M. Hickson, A. Canosa, C. Naulin, J.-M. Launay, I. R. Sims, and M. Costes. *Phys. Rev. Lett.*, **105**, 203201, 2010.

[175] K. M. Hickson and A. Bergeat. *Phys. Chem. Chem. Phys.*, **14**, 12057–12069, 2012.

[176] J. Daranlot, M. Jorfi, C. Xie, A. Bergeat, M. Costes, P. Caubet, D. Xie, H. Guo, P. Honvault, and K. M. Hickson. *Science*, **334**, 1538–1541, 2011.

[177] I. R. Sims, I. W. M. Smith, D. C. Clary, P. Bocherel, and B. R. Rowe. *J. Chem. Phys.*, **101**, 1994.

[178] B. J. Ratliff, C. C. Womack, X. N. Tang, W. M. Landau, L. J. Butler, and D. E. Szpunar. *J. Phys. Chem. A*, **114**, 4934–4945, 2010.

[179] M. Beckert, E. R. Wouters, M. N. R. Ashfold, and E. Wrede. *J. Chem. Phys.*, **119**, 9576 – 9589, 2003.

[180] P. C. Samartzis, B. L. G. Bakker, T. P. Rakitzis, D. H. Parker, and T. N. Kitsopoulos. *J. Chem. Phys.*, **110**, 5201–5207, 1999.

[181] I. S. McDermid. *J. Chem. Soc. Farad. Trans. 2*, **77**, 519–530, 1981.

[182] V. A. Alekseev and D. W. Setser. *J. Chem. Phys.*, **107**, 4771–4782, 1997.

[183] B. L. Bakker, A. T. Eppink, D. H. Parker, M. L. Costen, G. Hancock, and G. A. Ritchie. *Chem. Phys. Lett.*, **283**, 319 – 325, 1998.

[184] B. L. G. Bakker and D. H. Parker. *Chem. Phys. Lett.*, **330**, 293–299, 2000.

[185] R. Hilbig and R. Wallenstein. *Appl. Opt.*, **21**, 913–917, 1982.

[186] D. H. Mordaunt, M. N. R. Ashfold, and R. N. Dixon. *J. Chem. Phys.*, **104**, 6460–6471, 1996.

[187] H. Okabe and M. Lenzi. *J. Chem. Phys.*, **47**, 5241–5246, 1967.

[188] J. Biesner, L. Schnieder, J. Schmeer, G. Ahlers, X. Xie, K. H. Welge, M. N. R. Ashfold, and R. N. Dixon. *J. Chem. Phys.*, **88**, 3607–3616, 1988.

[189] K. Kambe and J. H. van Vleck. *Phys. Rev.*, **96**, 66–71, 1954.

[190] S. Jung, E. Tiemann, and C. Lisdat. *Phys. Rev. A*, **74**, 040701, 2006.

[191] A. C. Knipe and W. E. Watts. *Organic Reaction Mechanisms*. John Wiley and Sons, 1998.

[192] A. Papoulis. *Probability, Random Variables and Stochastic Processes*. McGraw-Hill Inc., 4th edition, 2002.

[193] M. Aitkin, R. Boys, and T. Chadwick. *Stat. Comput.*, **15**, 217–230, 2005.

[194] M. D. Hannam and W. J. Thompson. *Nucl. Instrum. Meth. A*, **431**, 239–251, 1999.

[195] I. J. Myung. *J. Math. Psychol.*, **47**, 90–100, 2003.